POLITECNICO DI TORINO

Master’s degree programme in Mechatronics Engineering

Master’s thesis

Analysis of mechanical properties of Li-Ion battery cells under breathing and swelling mechanisms for various boundary conditions

Supervisor
Prof. Alessandro Rizzo
Co-supervisor
Dipl.-Ing. Dipl.-Ing. Patrick Höschele

Author
Emanuele Michelini di San Martino

A.A. 2020/2021

AFFIDATIV

I declare that I have authored this thesis independently, that I have not used other than the declared sources/resources, and that I have explicitly marked all material which has been quoted either literally or by content from the used sources.

Emanuele Michelini

Graz, 29.03.2021

Signature

ABSTRACT

The propulsion of an electric vehicle (EV) is powered by an electric-vehicle battery. The most common batteries used in the automotive industry are lithium-ion batteries. The vehicle battery is organised in several modules, each of which contains several cells. Lithium-ion battery cells experience a continuous change in volume during use. The main causes are breathing, which is reversible and caused by the intercalation of ions during charging and discharging, and swelling which is an irreversible process caused by the ageing of the cell. Cells are commonly housed in modules and therefore their expansion is limited, resulting in the development of internal mechanical stresses. Large and inhomogeneous pressures acting on the cells can accelerate their ageing and contribute to the generation of dendrites in the anode which can lead to an internal short circuit.

The study of this phenomenon was carried out by measuring the thickness along the entire surface during charging and discharging of fresh and aged non-pretensioned cells utilizing capacitive sensors. While, in the case of pretensioned cells, instead of thickness the surface pressure was measured by means of a pressure mapping sensor. The obtained data was finally used for the development of an empirical model.

The results obtained showed that the increase in thickness from 0 to 100% SOC (state of charge) occurs mainly in the geometrical centre for the fresh cells (max. 3.06%, avg. 2.92%) and in the centre and along the edges for the aged cells (max. 2.82%, avg. 2.39%). Similarly, with pretensioned cells, higher pressure values were found in the centre of the cell. The global force development from 0 to 100% SOC was higher in percentage terms but lower in absolute terms with lower pretension values: with 300 N on average the percentage growth observed was 1866% and in absolute terms 1121 MPa, with 4000 N 107% and 2622 MPa, respectively. Generally, an increase in pretension causes an increase in the homogeneity of pressure distribution.

From the results obtained, it has been observed that the increase in volume is linked to several important parameters including SOC, position on the cell, pretension and ageing condition. The parameters involved were used for the development of the empirical model that allowed the formulation of equations that could be used in the development of a simulation model capable of predicting the behaviour of the cell and consequently help in the design of a module capable of homogenising the internal pressures and limiting the negative effects.

TABLE OF CONTENTS

LIST OF FIGURES

LIST OF TABLES

1 INTRODUCTION

1.1 Motivation

The car market is constantly evolving, and in particular, there is a remarkable growth in interest in electric vehicles (EVs). EVs includes both plug-in hybrid electric vehicles (PHEVs) and battery electric vehicles (BEVs). The expansion of electric vehicles is shown in Figure 1-1, in 2010 just 17'000 electric vehicles, mainly in China, Japan, Norway, the UK and the US, populated the world's roads. In 2019, there were 7.2 million electric cars worldwide. Over the last decade, the increase in the global stock of electric passenger cars has been at least 40% higher year on year. (IEA 2020)

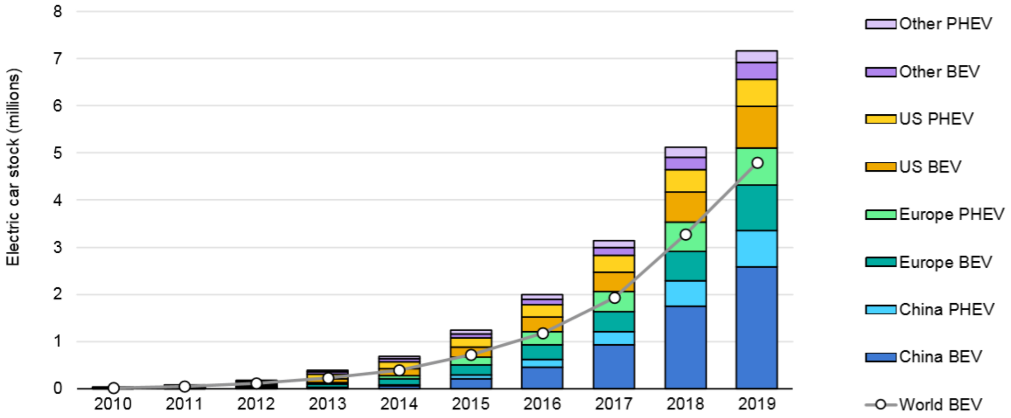

Figure 1-1 Worldwide distribution increase of electric cars considering PHEV and BEV (IEA 2020).

Electrification of mobility is a technological strategy that can bring several benefits: it is more efficient than internal combustion engines (ICE) and has zero tailpipe emissions; it contributes to reducing air pollution in densely populated cities and it is suited to the targets set by many countries to reduce greenhouse gas (GHG) emissions and expand energy diversification. (IEA 2020)

On-board technologies in electric vehicles have improved significantly in recent years, yet there is still room to further improve EVs in terms of performance, cost, and most importantly, safety. One of the key elements of the vehicle that is expected to improve dramatically is the battery pack which accounts for 35-50% of the cost of the entire vehicle and determines many of the vehicle's characteristics of interest to the buyer, including acceleration, range, price and safety (Kochhan et al. 2014). In the field of automotive batteries, much progress has been made in the last decade, energy density has increased up to 100%, production costs have fallen by 85% and fast charging technology has significantly reduced charging time. Despite this, it is considered that batteries have the potential to improve even further, which is why many studies are aiming to improve battery performance and to reduce their size, weight and cost. (IEA 2020)

1.1.1 Range Fading

Life cycle refers to the number of cycles from 0% to 100% state of charge that the battery is able to complete before reaching a capacity of below 80% and is one of the main parameters in evaluating the health of the battery. For the batteries installed in electric vehicles of particular importance is not only to have a large capacity, which results in high vehicle range but above all to preserve and maintain this capacity over the cycles. Preserving the capacity is essential not only to ensure a constant range of the vehicle over time but also because a battery mounted on an electric vehicle is no longer used when the retention capacity is less than 80% (Heymans et al. 2014; Neubauer and Pesaran 2011). The forces applied to batteries can significantly affect their life cycle, it is therefore particularly important to understand the stress and strain to which the cell is subjected, in order to optimize the behaviour, prolonging the life cycle and minimizing degradation. (Oh et al. 2014)

1.1.2 Internal Short-circuit risk

There are also some safety aspects to be taken into consideration, in particular, one scenario to be avoided is that of an internal short circuit, which is caused by the failure of the separator and the direct contact between anode and cathode. The internal short circuit leads to local heating through exothermic reactions and short circuit current. When a critical temperature is reached a self-sustainable exothermic reaction causes further separator meltdown increasing the active short circuit area leading to accelerated reaction kinetics. Furthermore, the heat propagates also to the cells adjacent to the one affected by the internal short circuit generating a chain effect throughout the module. Such a scenario, in addition to compromising the proper functioning of the battery, can have more serious repercussions for both the vehicle and the passengers, in particular, it can cause a thermal runaway and consequently the emission of smoke and toxic gasses or even fire or explosion, as shown in Figure 1-2. Separator failure can be caused by several reasons: mechanical (deformation or penetration of the cell), thermal (excessively high temperatures) or electrical (dendrite growth). Dendrites, as shown in Figure 1-3, are lithium crystals growing on the anode that are very thin and able to penetrate the separator. (Zhao et al. 2015)

Figure 1-2 Fire of a Lifan 650 EV triggered by an internal short circuit within the battery pack installed in the vehicle chassis (Sun et al. 2020).

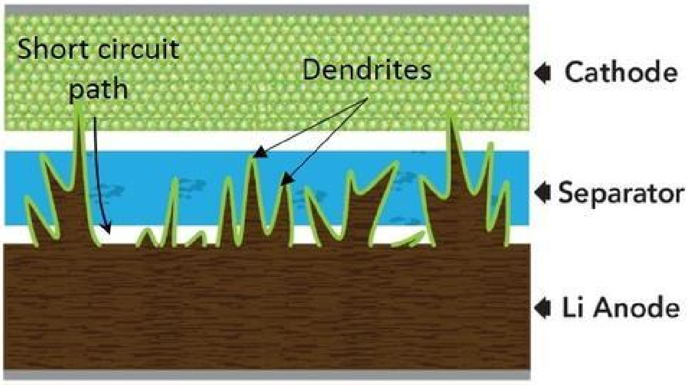

Figure 1-3 Tapered structures of lithium, known as dendrites, grow into the anode during battery operation, eventually short-circuiting the battery and posing a serious safety risk (SLAC National Laboratory, Stanford University 2015).

Ageing, which is closely linked to lithium plating and dendrite growth, is favoured by conditions of heterogeneous surface pressure distribution (Sauerteig et al. 2017). Therefore, being able to foresee and study how the surface pressure of cells constrained within a module varies during charge and discharge cycles, makes it possible to predict and minimise inhomogeneities, slowing down cell ageing and reducing the risk of internal short circuits.

1.2 Aim of the work

During battery use, the cells are subjected to mechanisms known as "breathing" and "swelling" which cause a change in battery volume. These phenomena, if the battery is placed inside the module, induce stress and strain as the constrained battery is unable to expand. The presence of these internal stresses can have a significant impact on both the life cycle and the occurrence of short circuits that can put the safety of the vehicle and passengers at risk. To properly address this problem some research questions were formulated:

- How can changes in the mechanical behaviour of Li-ion battery cells under breathing and swelling (B&S) be detected?
- Which factors influence the mechanical behaviour of Li-ion battery cells under B&S?
- Can the mechanical behaviour of Li-ion battery cells be influenced by design elements in the battery module?
- Can the changes in the mechanical properties of a Li-ion battery cell under B&S be mapped using numerical methods?

A methodological approach, schematized in Figure 1-4, was structured to answer these questions. The work started from the analysis of the scientific literature on lithium-ion batteries and in particular breathing and swelling mechanisms. After that, experiments to evaluate the breathing behaviour of non-pretensioned cells were designed and planned, and the technique for acquiring the thickness change was defined. The collected data was processed and analysed. A similar process was used to obtain results for pretensioned cells, where instead of measuring the thickness change, the surface pressure distribution was measured. Experimental evaluations were carried out with both fresh and aged cells. Finally, with the data collected, an empirical model was developed.

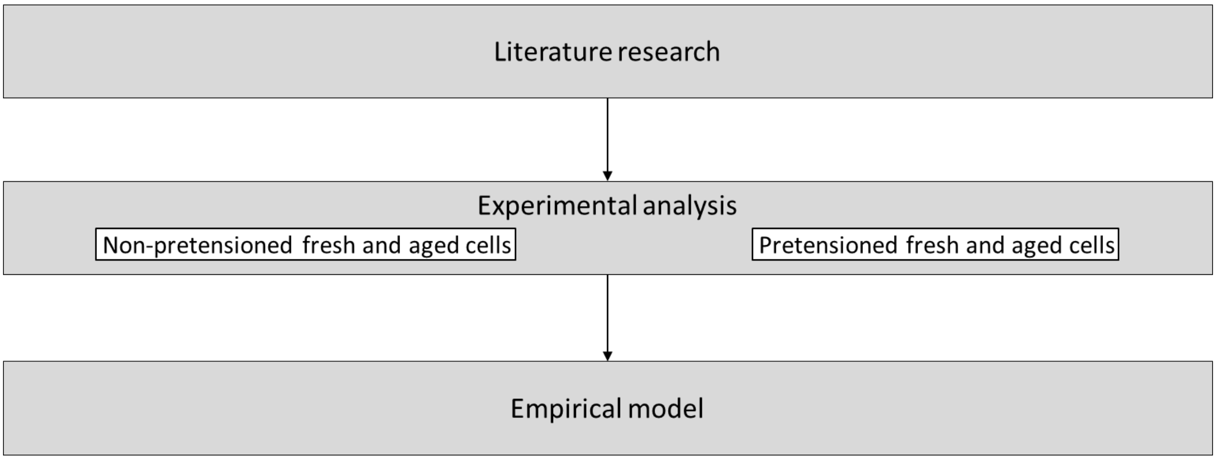

Figure 1-4 Methodological approach.

1.2.1 Benefit for the state of the art

The analysis permits to study the local effects of breathing and swelling, extending the current scientific literature, which is mainly directed towards a global analysis of breathing and swelling. Another aspect new to the literature is also studied, namely the effect of ageing on breathing. The benefits to the state of the art are listed in Table 1-1.

Table 1-1 State of the art extension.

Current state of the art	**Extension to the state of the art**
Thickness increase analysis in the centre	Surface thickness increase analysis
Global force measurement of pretensioned cells	Local pressure distribution of pretensioned cells
Ageing effects on breathing not considered	Ageing influence on local displacements

2 STATE OF THE ART

2.1 Batteries in electric vehicles

There are many types of batteries, but on electric vehicles it is common to find batteries from either the nickel-metal-hydride (NiMH) or lithium-ion (Li-ion) families. EVs batteries require both high power density and high energy density, as the battery plays a central role in the mobility of the car (Sarlioglu et al. 2017). NiMH batteries have a lower rated voltage (approx. 1.2V), low internal impedance and good tolerance to over-charge or over-discharge. Li-ion batteries have a higher rated voltage (approx. 3.3V), higher energy density, higher power density, but as drawbacks, higher manufacturing costs and are subject to ageing (Mars et al. 2017).

2.1.1 Li-Ion Batteries

Lithium-ion batteries are very popular because they not only contain a high level of energy and power in a limited volume and weight (energy density > 250 Wh/kg and > 750 Wh/l, power density from 1000 W/kg up to 20000 W/Kg (Cano et al. 2018)), as shown in Figure 2-1, but are also able to deliver 3 times more energy than other common batteries such as Ni-Cd or Ni-MH. Besides, they are not subject to the "memory effect" that is very common with other battery types (Xiong and Shen 2018).

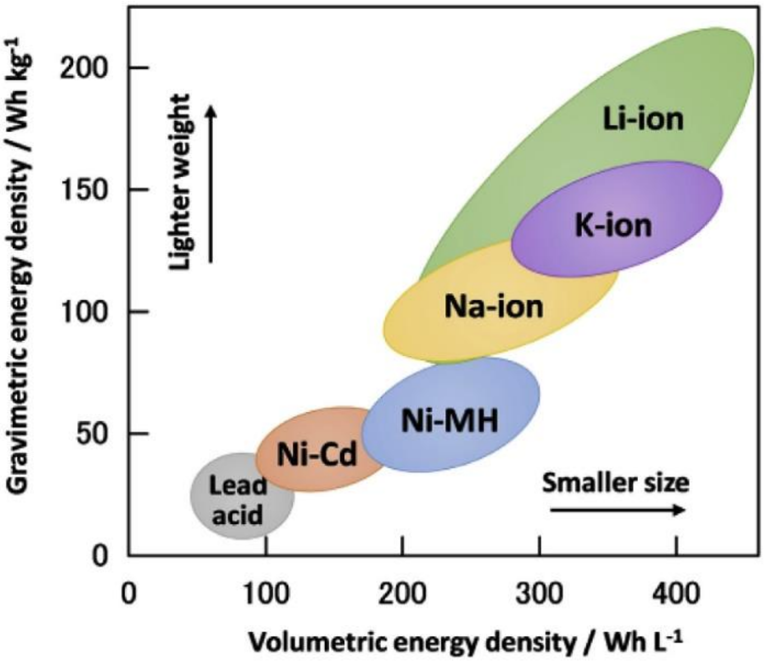

Figure 2-1 Gravimetric energy density over volumetric energy density for different types of state-of-the-art battery chemistry (El Kharbachi et al. 2020).

2.1.1.1 Components in a cell

Batteries with liquid electrolyte, as shown in Figure 2-2, are made up of four basic elements:

- Anode: negative electrode of the battery, commonly made of graphite, coated on a copper current collector.
- Cathode: positive battery electrode, commonly made of a lithium metal oxide, coated on an aluminium current collector.
- Separator: an insulating membrane that separates the anode and the cathode to avoid short-circuit, but its structure allows the passage of lithium-ions.
- Electrolyte: a compound in liquid form consisting of lithium salts in an organic solvent with high ionic conductivity in which the electrodes and separator are immersed. It enables the movement of the lithium-ions from the cathode to the anode and vice-versa.

The operating principle is based on the migration of lithium-ions from one electrode to another and their intercalation (or deintercalation) in the active material. (Korthauer and Wuest 2018)

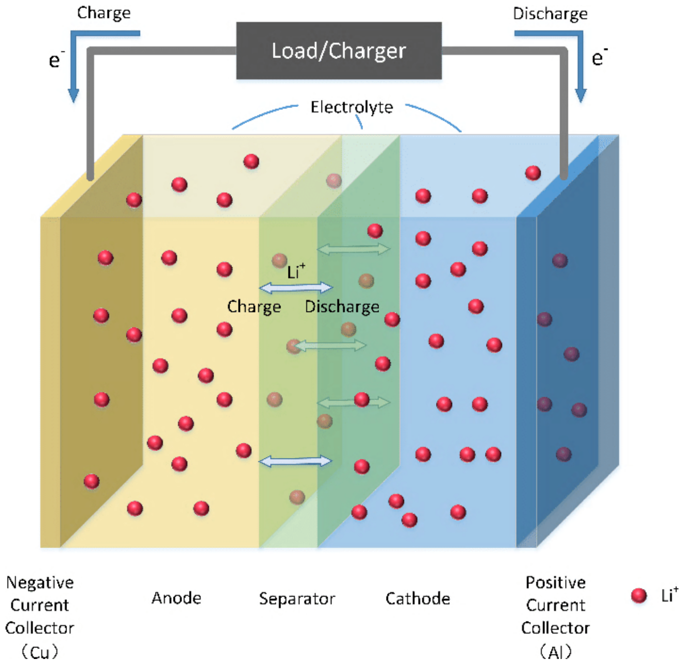

Figure 2-2 Schematic image of a lithium-ion battery and its main elements: anode, cathode, separator and electrolyte (Zhang et al. 2018).

2.1.1.2 Intercalation

Lithium-ion batteries consist of a metal oxide cathode and a graphite anode. Cells operate through a reversible topotactic reaction, shown in Figure 2-3, during which lithium-ions (guests) are inserted or removed within a matrix (host) without significantly changing its structure. During charging electrons migrate from the negative electrode to the positive one. To maintain electrical neutrality the lithium-ions are intercalated through the separator between the graphite layers forming the graphite intercalation compounds (GICs) which are lithium hexacarbide (LiC6) when the battery is fully charged. Similarly, during discharge, lithium-ions are deintercalated from the anode and travel, through the separator, to the cathode forming, in the case of a Nickel/Manganese/Cobalt (NMC) cathode, LiNiMnCoO2.There are other types of positive electrodes with different chemistry (see Chapter 2.1.1.3) which will form different compounds. (Wu 2015)

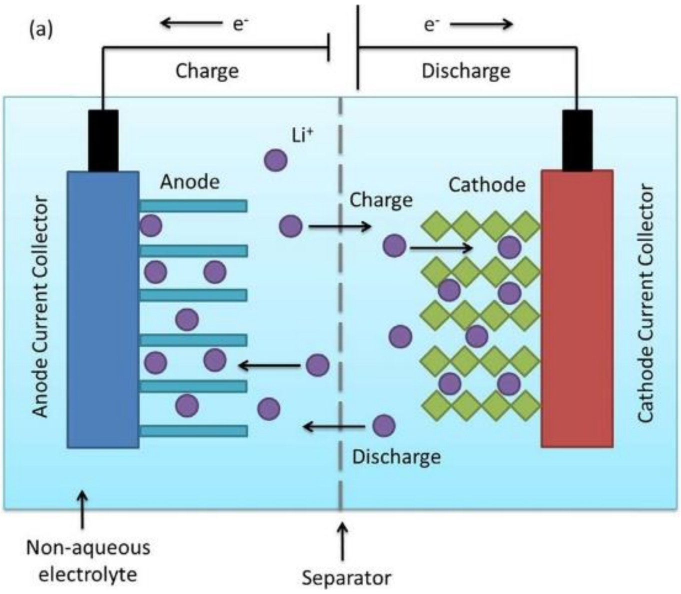

Figure 2-3 Schematic on intercalation and deintercalation processes in lithium-ion batteries (Few et al. 2018).

2.1.1.3 Positive electrodes

Lithium-ion batteries include a wide variety of cells with different chemistry, shape and size. One of the main classification methods is based on the material used for the positive electrode (cathode). In particular, 5 major families can be defined (Lighting Global 2019):

1. Lithium cobalt oxide (LCO): This type is very present in a wide variety of different applications due to its high energy and power density. However, this type of battery has a short lifecycle, which makes it unsuitable for off-grid applications; it has low thermal stability, which translates into low safety performance; and the raw materials needed for production are expensive.
2. Lithium manganese oxide (LMO): these batteries have good thermal stability, and compared to LCOs are cheaper and safer but with a shorter life cycle. Nowadays they are almost totally replaced by NMC batteries.
3. Nickel cobalt aluminium (NCA): these batteries have the highest energy density, however, they have low thermal stability, high manufacturing costs and a short life cycle. Again they are unsuitable for off-grid products.
4. Lithium Iron Phosphate (LFP, LiFePO4): these cells offer the best thermal stability, excellent safety, high power and long life cycles with limited costs. These characteristics make these

batteries well suited for off-grid applications. Conversely, they have low energy density and low output voltages.

5. Lithium nickel manganese cobalt oxide (NMC, NCM): this type of battery is safer, less expensive, with higher energy density and longer life cycles than LCO batteries. Different ratios of nickel, manganese and cobalt allow emphasizing specific qualities to optimize the battery for a particular application. The ratios within the cathode in NMC cells determine the commercial nomenclature of the battery, for example when the distribution of nickel, cobalt and manganese is the same they are identified as NMC111 (or NMC333), NMC622 if it is composed of 6 parts Ni, 2 parts Mn and 2 parts Co, this type, along with NMC532, is a typical low-cobalt structure used in the automotive industry (Wentker et al. 2019). This type of cell is the subject of much research and appears to be a very promising technology.

The chemistry of the cell, as shown in Table 2-1, has an important effect on breathing as different molecules form different compounds thus also varying their occupied space. However, the volumetric change of the cathode due to breathing in the case of NMC chemistry is particularly low compared to the cathodes of different composition. Moreover, compared to the volumetric change of the graphite anode (about 6-10%), it is an order of magnitude lower, making its contribution to breathing negligible. (Dambrowski 2013; Oh et al. 2014)

Table 2-1 Values of volumetric changes for breathing due to intercalation for different cathode chemistries (Dambrowski 2013; Oh et al. 2014).

Positive electrode chemistry family	**LCO**	**LMO**	**NCA**	**LFP**	**NMC**
Relative volume increase (0-100%)	2-3%	6.5-14%	1-2%	6.8%	1-2%

2.1.1.4 Cell construction

Batteries can also be classified according to their shape. There are mainly three different types, illustrated in Figure 2-4 (Lighting Global 2019):

1. Cylindrical: are made by rolling up the three layers: cathode foil, separator and anode foil. After that, they are hermetically sealed in a rigid steel or aluminium structure.
2. Prismatic: the assembly method is similar to cylindrical batteries, but the casing is a rectangular parallelepiped so that the thickness of the battery is reduced. This type of battery is widely used in consumer electronics, especially in applications where periodic battery replacement is required.
3. Pouch: consists of stacks of several layers of alternating electrodes with separators. The shape of these batteries is similar to prismatic batteries, except that the rigid housing is replaced by

a thin flexible laminated polymer/aluminium pouch. Removing the rigid casing reduces the cost, weight and thickness of the cell and when stacked allows to obtain a better packaging efficiency than other cell types. The low mechanical stability not only makes the cells easily and efficiently stackable but also makes them more prone to swelling and, if the change of the volume of the cells stacked inside the module is not properly considered, pressure peaks can be generated resulting in capacity loss, life cycle shortening and safety issues.

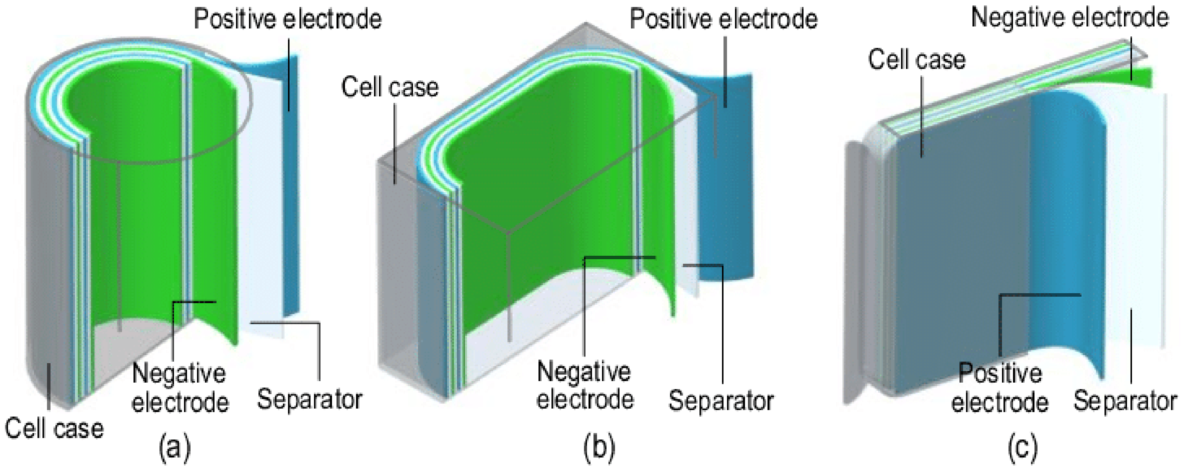

Figure 2-4 Different commercial battery types according to their shape: cylindrical, prismatic and pouch (Bilgin et al. 2015).

2.1.2 Battery Modules

The cell is the single unit of a battery, many cells can be assembled to form a module, as shown in Figure 2-5, multiple modules connected together with sensors, a controller and a housing form a battery pack. The battery pack in EVs is connected to the power train. The module is normally composed of (Greenwood 2018):

- Casing: the housing is typically made of metal and provides mechanical support. It also allows adequate compression to be applied to the cells to improve their performance.
- Temperature sensors: the sensors monitor the temperature of the module. This information is transmitted to the battery management system (BMS), which controls the cooling system and the power delivery to remain within safe limits.
- Cells: each module within a package always contains the same number of cells. The number of cells depends on the space available, the voltage and the power required.
- Terminals: each cell has a negative and a positive tab, which are welded properly to the module terminals. In addition, the module terminals are properly connected via the bus bars inside the pack.
- Cooling channels: to control the temperature and avoid thermal runaway events, there are special channels inside the module that allow the passage of cooling liquid or air.

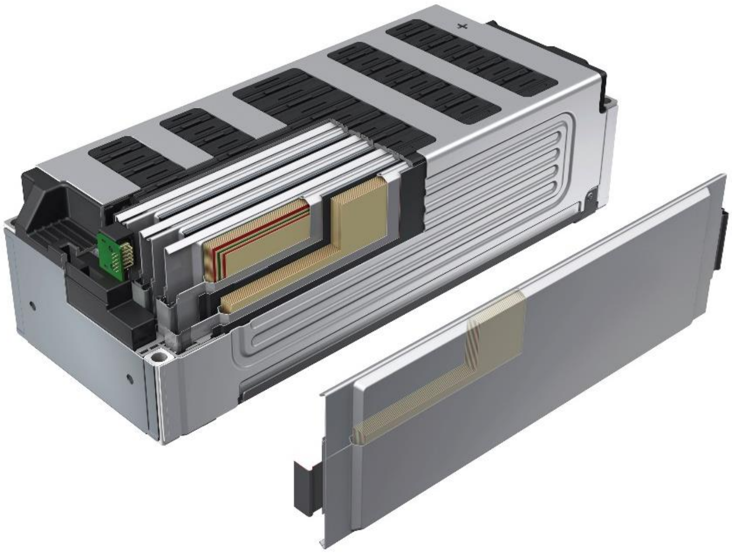

Figure 2-5 Exemplary of a battery module in aluminium containing 12 pouch Li-ion cells, this module is mounted on the Audi e-tron (AUDI AG 2015).

2.2 Breathing

The reversible flow of lithium-ions during charge and discharge cycles causes continuous expansion or contraction of the cell. The increase in volume during charging is due to the lithiation process that results in the formation of graphite-Li intercalation compounds (G-LICs), the magnitude of volume increase is closely related to the structure and stoichiometry of the electrode. A graphite anode generally exhibits a reversible 6-10% increase in thickness due to breathing. Similarly to the anode also the cathode is subjected to expansion/contraction, nevertheless, the influence in terms of volumetric variations of the NMC cathode during ion intercalation is less than 2%, hence, considerably lower compared to graphite (Oh et al. 2014; Dambrowski 2013).

During charge and discharge cycles the volumetric change of the cell is not only caused by the intercalation but also by the thermal effects acting on the cell. Temperature growth is more pronounced when the cell is subjected to higher C-rates, consequently cells subjected to higher charge or discharge currents will be more affected by the thermal displacement effect. Nevertheless, it is possible to distinguish the contribution given by the thermal expansion with respect to the volumetric change by intercalation through the relaxation period. In fact, as shown in Figure 2-6, the relaxation allows the thermal effect on the volume to be exhausted while it affects marginally the intercalation displacement. (Rieger et al. 2016)

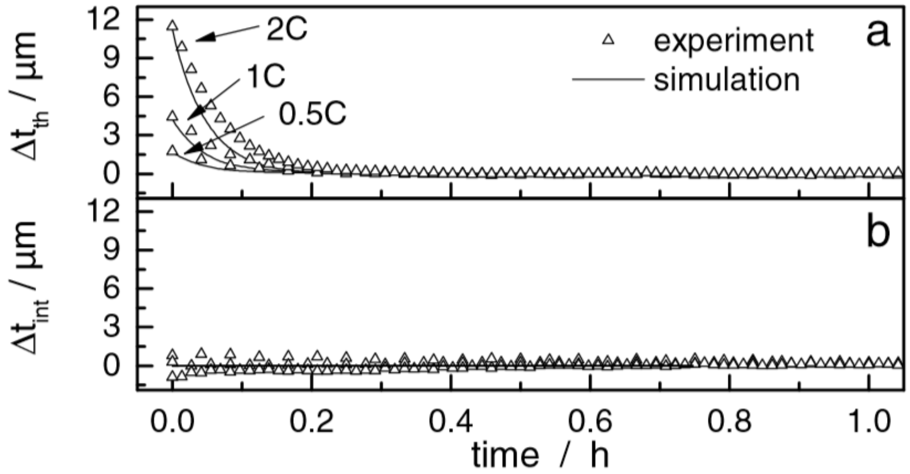

Figure 2-6 The effect of relaxation on thermal displacement Δt_{th} (a) and intercalation displacement Δt_{int} (b) are displayed. The thermal effects fade with time, while there is a negligible influence of time on the volumetric change by intercalation (Rieger et al. 2016).

During charging there is another mechanism known as "overshoot" which consists of an increase in thickness, that occurs during the end of the charging phase of the cell, and during which absolute thickness values are higher than those occurring with a fully charged battery. The overshoot occurs at the end of the constant current (CC) phase, peaking at around 90% state of charge (SOC) and subsequently tends to decrease during the constant voltage (CV) phase. Overshoot is closely related to the C-rate: for low C-rates, there is no overshoot, but after a certain threshold the overshoot increases with the increase of the C-rate. This mechanism is related to the lower intercalation uniformity when lithium-ion migration happens faster (Lee et al. 2003). This phenomenon is caused by inhomogeneity of ion distribution on the negative electrode caused by rapid intercalation (high C-rates) and slow diffusion of ions within the anode, this phenomenon is graphically represented in Figure 2-7. A subsequent relaxation period allows lithium-ion to redistribute in the graphite particles resulting in the compensation of most of the inhomogeneities. (Sommer et al. 2015)

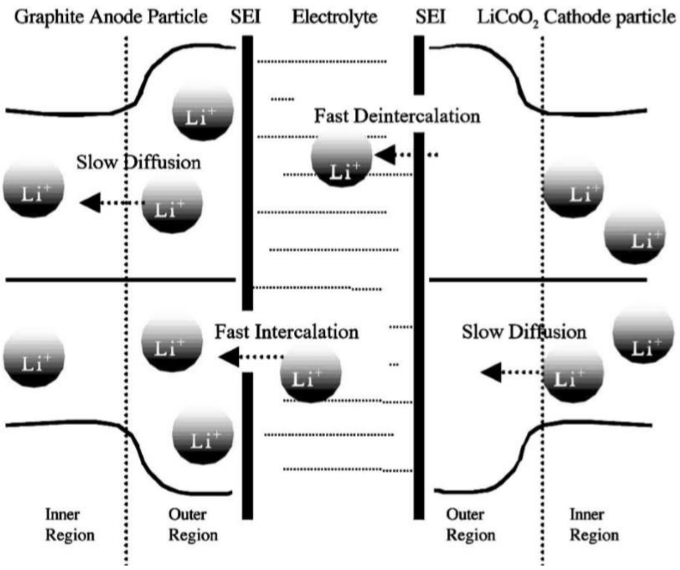

Figure 2-7 Intercalation during charging of a lithium-ion cell, the cell is subjected to fast Li-ion intercalation and slow diffusion in the graphite particle (Wang et al. 2004).

The cells are typically constrained in a device or assembled within a battery module housing thus they cannot expand and are subjected to high stress formation (Sauerteig et al. 2017). Figure 2-8 shows that the stress applied to the battery fluctuates as a function of the state of charge independently of the pretension applied, however with higher pretensions the magnitude of fluctuations is greater. This behaviour is related to the fact that the pouch cell has a non-linear elastic mechanical behaviour, when the stress levels are higher the stiffness increases, which translates that with the same level of expansion, the stress fluctuations will be greater for higher stresses (Cannarella and Arnold 2014).

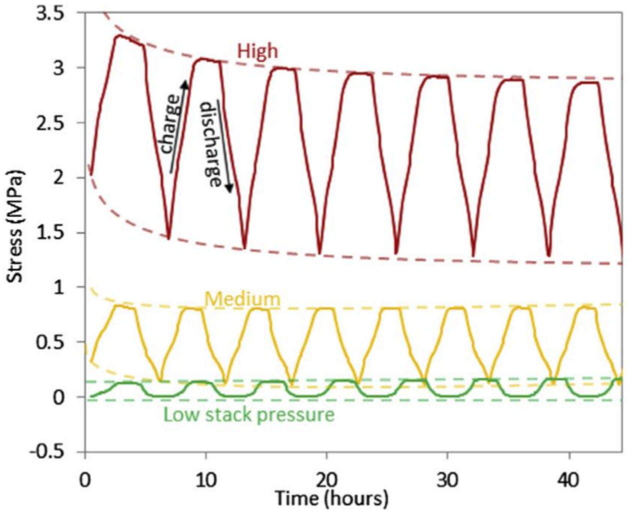

Figure 2-8 Evolution of stress fluctuations for different types of pretensions (Cannarella and Arnold 2014).

2.3 Swelling

During use, lithium-ions react with the anode and form Li-containing products; the cells undergo gradual consumption of lithium-ions and the formation of passivation films (Sauerteig et al. 2017). Lithium plating, in addition to causing irreversible expansion of the cell and a reduction in capacity due to the decrease of lithium-ions, is also a problem for safety since it can grow in the form of dendrites that may penetrate the separator causing an internal short circuit in the cell.

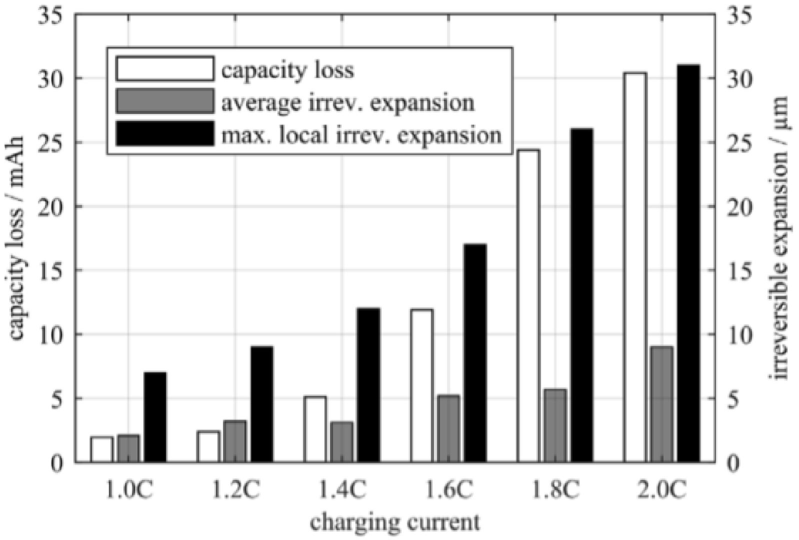

Figure 2-9 Relation between irreversible swelling, capacity loss and charging rate (Spingler et al. 2018).

Higher C rates, as shown in Figure 2-9, and lower temperatures cause more irreversible swelling and accelerate the ageing mechanism. Irreversible swelling due to ageing focuses mainly on the edges of the graphite anode as shown in Figure 2-10.

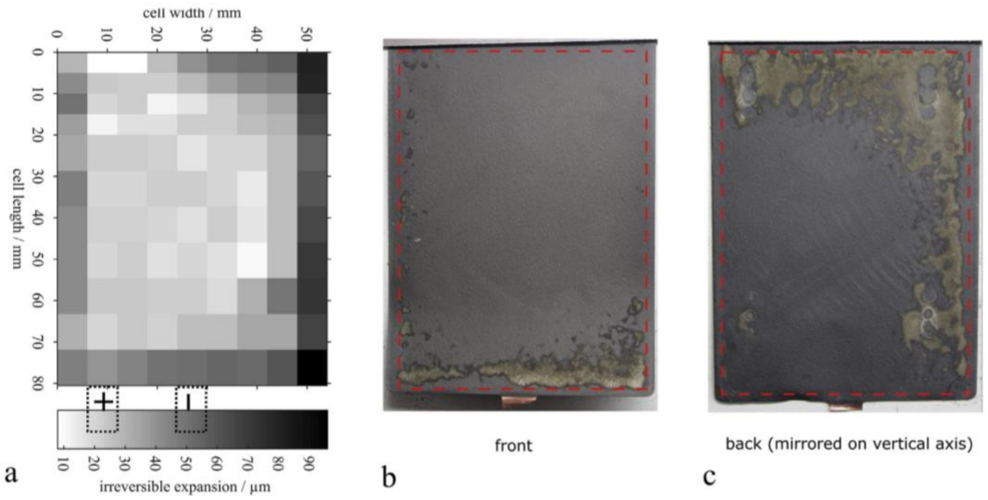

Figure 2-10 (a) Shows the irreversible cell expansion (b-c) Picture of an aged graphite anode with lithium deposition. The post-mortem analysis shows the distribution of the plating which occurs mainly along the edges (Spingler et al. 2018).

Another role related to irreversible swelling is given by the overshoot seen in 2.2. Overshoot, as shown in the graph in Figure 2-11, is a phenomenon that occurs during the transition from constant current charge to constant voltage at high C-rates and is not related to thermal phenomena. Of particular interest is the fact that for high C-rates part of the given overshoot expansion is irreversible, indicating that lithium plating occurs and the cell capacity is reduced. (Spingler et al. 2018)

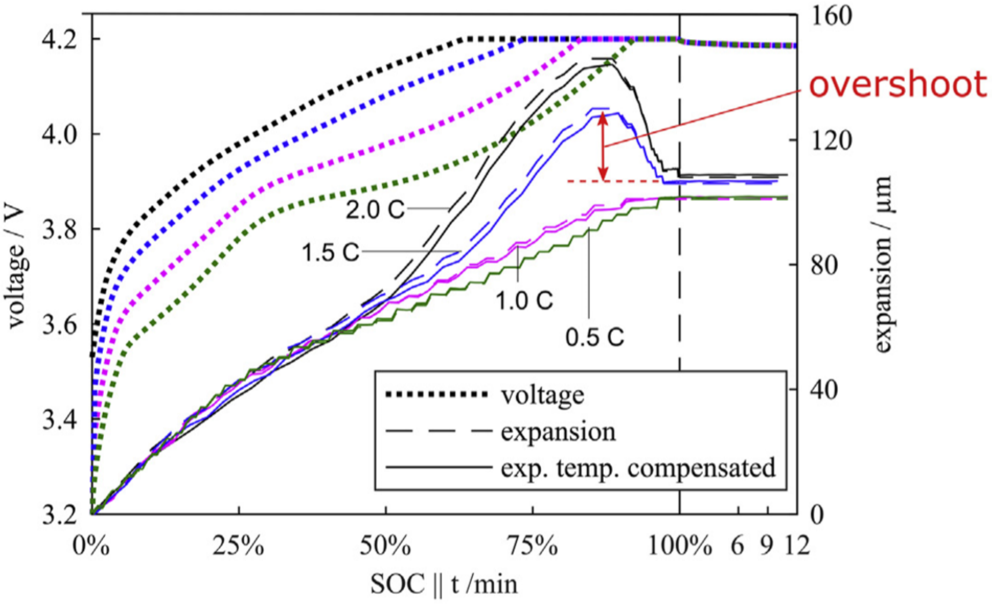

Figure 2-11 Measured voltage and cell expansion (with and without thermal effects) from 0% SOC to 100% SOC for different C-rates. The overshoot starts in the DC-CV transition and peaks around 90% SOC, then going towards full charge it decreases (Spingler et al. 2018).

Ageing is affected by the pretension applied to the cell. Cells are commonly placed inside a module and consequently subjected to a compressive stack pressure. This parameter is of particular importance because besides having a remarkable impact on battery performance, it is easily controllable by the manufacturer. A cell subjected to high pretension has a shorter life cycle, however, lower pretensions have shown an increase in capacity retention compared to non-pretensioned cells. The decrease in capacity as a function of applied pretension is summarized in the graph in Figure 2-12. As the applied stack pressure increases, the possibility of lithium plating increases and therefore the amount of cyclable lithium decreases. Nonetheless, a slight stack pressure is necessary to keep the cell layers in contact, preventing delamination due to electrode rippling and deformation of the cell during cycling. (Cannarella and Arnold 2014)

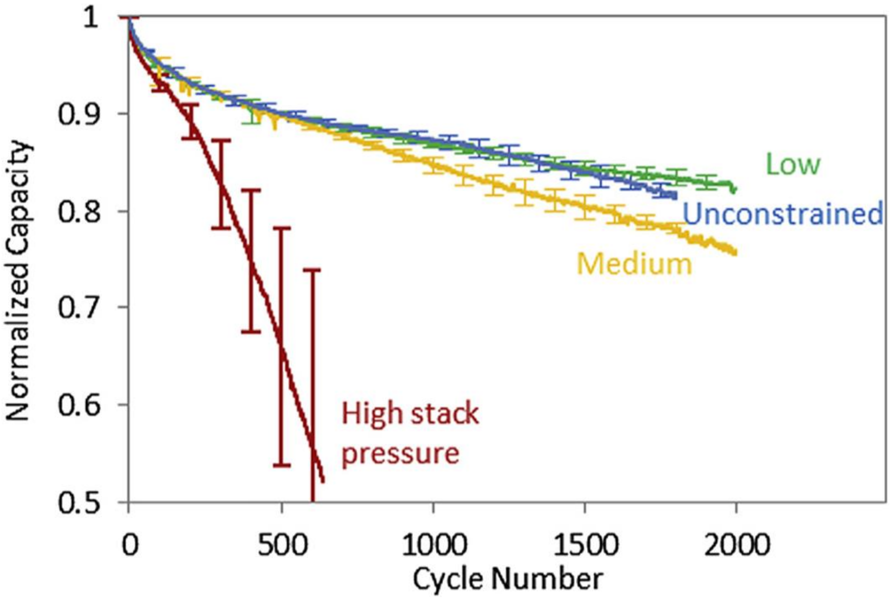

Figure 2-12 The behaviour in terms of capacity loss with different stack pressures: high (5MPa), medium (0.5MPa), low (0.05MPa) and unconstrained (Cannarella and Arnold 2014).

Non-uniform pressure distribution causes heterogeneous deposition of lithium; this phenomenon occurs because compression directly affects the tortuosity and porosity of the separator and thus influences the diffusion of ions through it. The difference in compression causes inhomogeneity in the ageing process of the cell, which favours the degradation of cell capacity. Homogeneous compressions not only delay the capacity fading process but also allow reproducible cycles to be obtained, which benefits the determinism of the battery behaviour. (Müller et al. 2019; Bach et al. 2016)

2.4 Capacity retention

The ageing and in particular the plating of lithium metal on the graphite anode causes a reduction in the total number of lithium-ions and consequently a reduction in the specific capacity of the cell. As shown in Figure 2-13, a cell subjected to many cycles will experience a greater reduction in specific capacity, this process is known as capacity fading. Similarly, capacity retention is the preservation of specific capacity and is measured in terms of attainable state of charge.

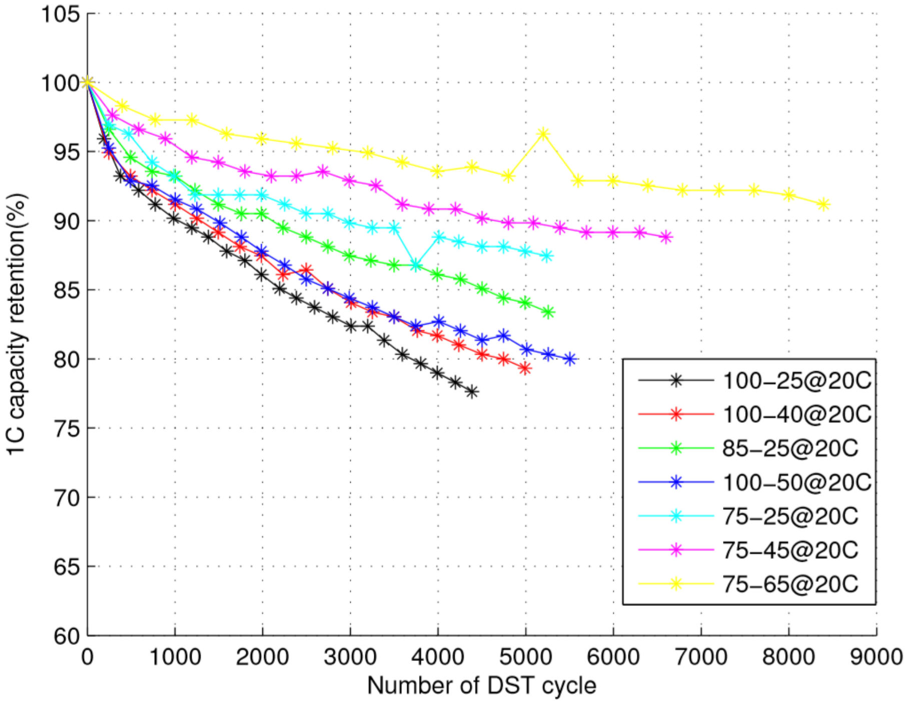

Figure 2-13 Capacity retention is measured as a function of cycles. DST (dynamic stress test) are mixed cycles utilized to measure battery performance. 1C capacity retention refers to the fact that the cell is charged with 1 C after each discharging cycle in order to evaluate the capacity retention. The legend refers to the cycling SOC range (numbers before the @) and to the room temperature (number after the @). The capacity retention decreases with the number of cycles the cell is subjected to. (Xu et al. 2018).

3 CELL

3.1 Specifications

The analysed cells are pouch type with nickel-manganese-cobalt oxide (NMC622) cathode and graphite anode with a nominal capacity of 60 Ah. More information can be found in Table 3-1.

Figure 3-1 Top view and front view of the cell.

Table 3-1 Cell specifications.

Manufacturer	LG Chemical
Cell model	E63B
Cell type	Pouch
Chemistry	Graphite / NMC622
Body dimensions	260 x 90 x 14.5 mm
Pouch dimensions (without tabs)	300 x 110 mm
Tabs dimensions	10 x 45 mm
Weight	890 g
Capacity	60 Ah
Nominal voltage	3.63 V
Maximum Voltage	4.2 V
Minimum Voltage	2.5 V
Internal resistance (1C ; 10 s; 25°C)	1.5 mΩ
Volumetric energy density (C/3 ; 25°C)	504 Wh/l
Gravimetric energy density (C/3; 25°C)	251 Wh/kg

3.2 Cell internal structure

The internal structure of the cell, shown schematically in Figure 3-2, is characterized by alternating cathodes and anodes divided by a separator layer wrapped through the layers or by individual separator sheets. Details of the cathode, anode and separator layers are shown in Table 3-2.

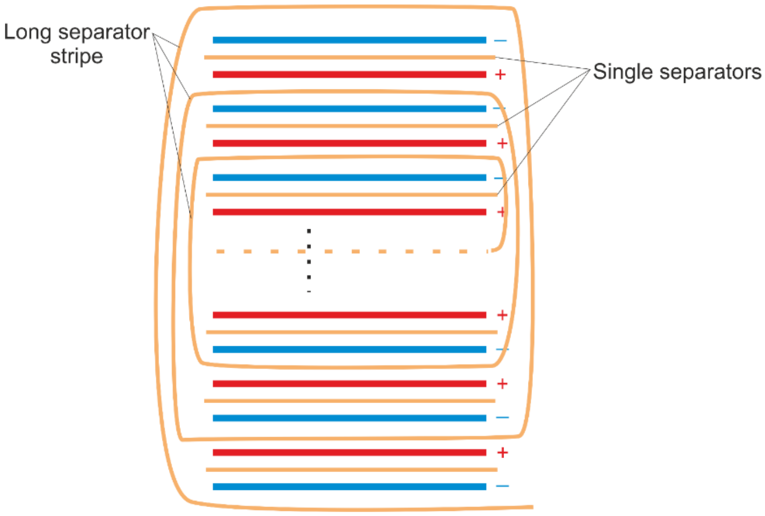

Figure 3-2 Schematic view of the distribution of the anode, cathode and separator layers of the cell (Source: ICTM/TU Graz).

Table 3-2 Geometric details of the anode, cathode and separator layers (Source: ICTM/TU Graz).

	Anode	**Cathode**	**Separator**
Number of layers	32	31	65 (42 + 23 wrapped)
Length	26 cm	26 cm	26.3 cm
Width	9 cm	9 cm	9.2 cm
Thickness overall	208 µm	172 µm	15 µm
Thickness current collector	8 µm	12 µm	

This technique causes the accumulation of separator at the edges of the cell and the subsequent generation of bumps. An example of a bump can be seen in Figure 3-3 on the anode.

Figure 3-3 Example of the presence of bumps on the right edge (anode).

3.3 Charging and discharging strategy

The cell is charged using a constant current-constant voltage (CC-CV) cycle. This means that the cell is charged at a constant voltage until the upper threshold is reached, after which, keeping the voltage constant, the current is gradually decreased until the limit value is reached. Similarly, it is discharged through a CC-CV approach, in this case, the cell is discharged with constant current up to the minimum voltage and then, while the voltage is kept constant, the current is decreased gradually up to the limit value. The threshold values are listed in Table 3-3. In the example shown in Figure 3-4, the cell is charged and discharged at 1 C, hence using a charging current of 60 A and a discharging current of -60 A.

Table 3-3 Voltage and current thresholds upon charging and discharging.

Phase	**Voltage limit [V]**	**Current limit [A]**
Charging	4.2	3.0
Discharging	2.5	-3.0

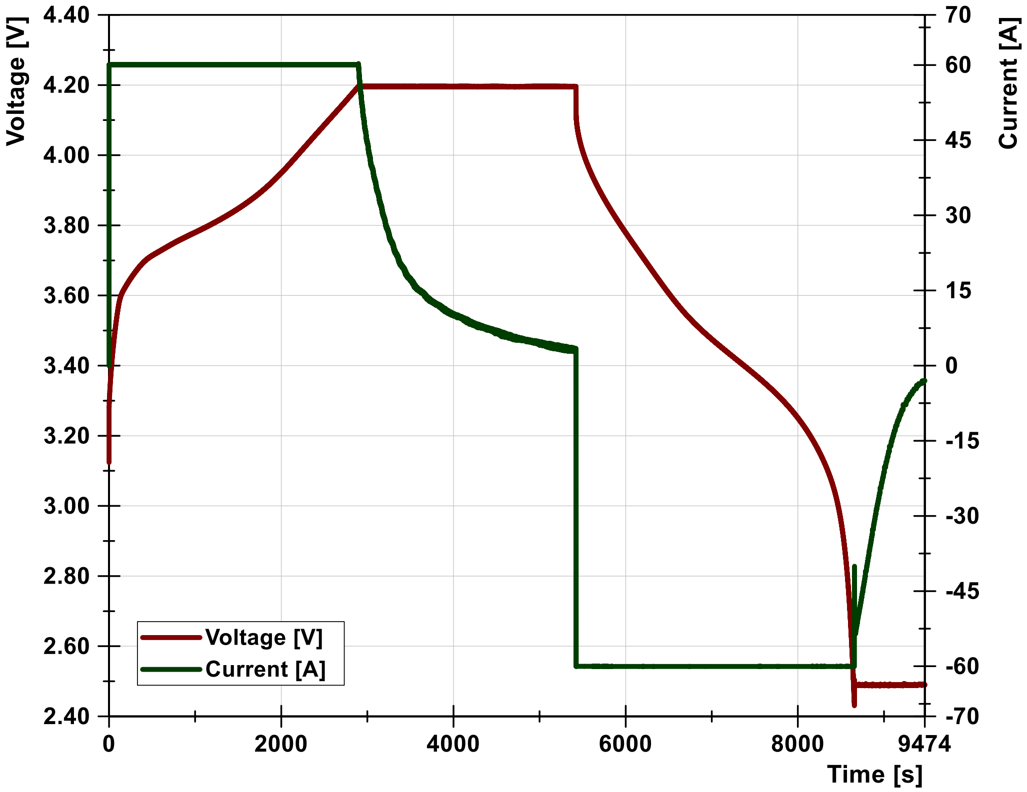

Figure 3-4 Full charging-discharging cycle of the cell at 1C.

3.4 Ageing

A total number of 7 cells were used, the first 3 cells are fresh and the last 4 are aged. The aged cells used in the experiments were aged by AVL List GmbH following two different ageing strategies. In particular, as shown in Table 3-4, albeit all the cells were aged through cycles ranging from 0 to 80% SOC with a C-rate of 0.5 during charging and 1.2 during discharging, cells 4 and 6 were cycled with a pretension of 300 N while cells 5 and 7 were cycled with a higher pretension equal to 4000 N. The cells with the highest pretension, although they were subjected to a lower number of cycles, are those that have suffered the greatest loss in terms of capacity. From now on, the ageing to which cell 4 and cell 6 have been subjected is referred to as ageing method 2, the ageing to which cells 5 and 7 have been subjected as ageing method 1.

Table 3-4 Ageing procedure, cells 5 and 7 follow the ageing method 1, cells 6 and 4 follow the ageing method 2.

Cell	Charge (C-Rate)	Discharge (C-Rate)	SOC range	N° of cycles	Capacity retention	Pretension [kN]
4	0.5	1.2	0-80	300	85.7	0.3
6	0.5	1.2	0-80	150	81.7	0.3
5	0.5	1.2	0-80	300	67.1	4
7	0.5	1.2	0-80	200	70.1	4

4 BREATHING & SWELLING IN NON-PRETENSIONED CELLS

4.1 Method

The surface thickness of non-pretensioned cells is measured for fresh and aged cells in order to investigate the factors influencing volumetric changes during charging and discharging. The thickness of the cells is measured using two capacitive sensors (see Appendix 9A.1.1) connected to the mechanical arm of the testbed (see Appendix 9A.1.2.1) and positioned along the z-axis on either side of the cell, as shown in Figure 4-1.

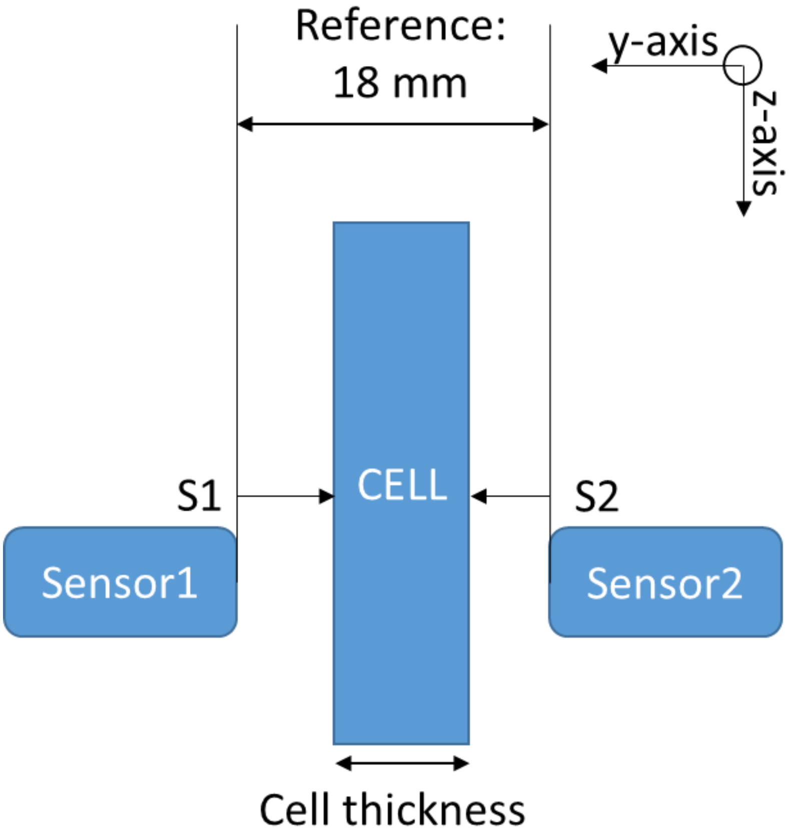

Figure 4-1 Principle sketch of the cell thickness measurement using two capacitive sensors.

The distance between the sensors is calibrated using a gauge block of 18 mm. Knowing the distance measured by the sensors, and the distance between the sensors it is possible to obtain the thickness of the cell.

$$Thickness = Ref - (S1 + S2)$$

With:

- Thickness = resulting thickness of the cell [mm]

- Ref = the reference distance measured with the gauge block [mm]
- S1 = distance measured by the sensor S1 [mm]
- S2 = distance measured by the sensor S2 [mm]

The cell is fixed by a structure that allows movement along the x-axis while the y-axis is blocked by means of pneumatic brakes. The cell is clamped at the pouch seams, so there is no pretension acting on the body, allowing a non-pretensioned breathing scenario to be simulated. This system allows the sensors to measure the entire surface of the cell, which extends along the x and z axes, as shown in Figure 4-2.

Figure 4-2 Degrees of freedom of the sensors with respect to the cell.

The sensors have a diameter of 20 mm, so measurements cannot be made less than one centimetre from the edge of the cell, and the reference surface is reduced from 260x90 mm to 240x70 mm. The measuring points are positioned 10 mm apart, i.e. 24 points along the x-axis and 7 along the z-axis, giving a total of 175 points along the entire surface. A graphical scheme is shown in Figure 4-3.

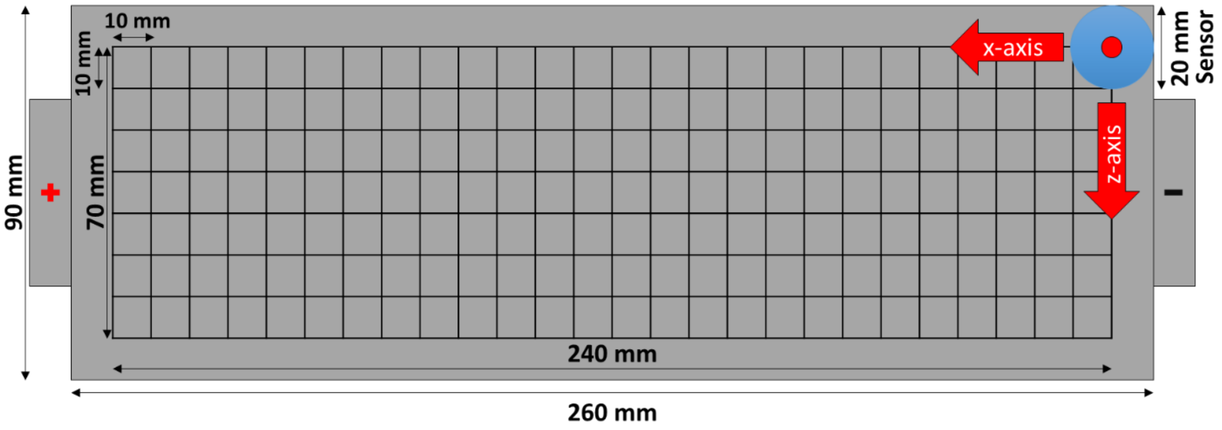

Figure 4-3 Schematic of the measurement points, every crossing corresponds to a measurement point. The red circle in the top right corner represents the origin of the x and z axes. The blue circle in the top right corner represents the area occupied by the sensor.

The thickness of the entire surface was measured at some specific SOCs, shown in Figure 4-4. Specifically, during charging at 0% SOC, 30% SOC, 60% SOC, 90% SOC and 100% SOC, and during discharging at 60% SOC, 30% SOC and 0% SOC. This approach is adopted to understand how cell thickness evolves as the state of charge increases rather than simply analysing the fully discharged cell and the fully charged cell. Furthermore, one more SOC is analysed during charging than during the discharge cycle, at 90% in order to check for the presence of overshoot.

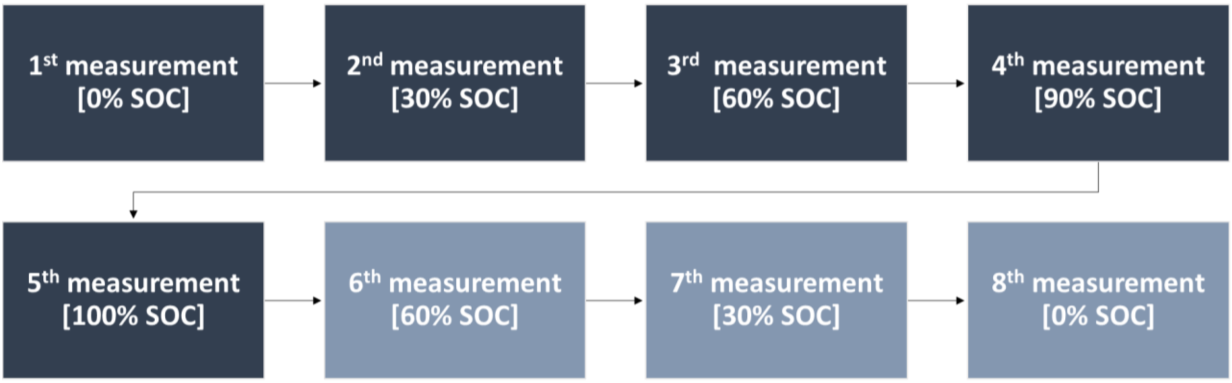

Figure 4-4 SOC at which the thickness is measured.

Additionally, each time a given SOC is reached, a relaxation period is waited before starting the measurement of the entire surface, the complete procedure is shown in Table 4-1. This procedure ensures that the accuracy of the measurement is not affected by thermal effects, more details are presented in Chapter 7.1.

Table 4-1 Steps of the full cycle with non-pretensioned cells.

Step	**Action**	**State of charge**
0	Thickness measurement of the whole surface	0%
1	Charge – thickness measurement in the centre	0-30%
2	Wait – thickness measurement in the centre	30%
3	Thickness measurement of the whole surface	30%
3	Charge – thickness measurement in the centre	30-60%
4	Wait – thickness measurement in the centre	60%
5	Thickness measurement of the whole surface	60%
7	Charge – thickness measurement in the centre	60-90%
8	Wait – thickness measurement in the centre	90%
9	Thickness measurement of the whole surface	90%
9	Charge – thickness measurement in the centre	90-100%
10	Wait – thickness measurement in the centre	100%
11	Thickness measurement of the whole surface	100%
12	Discharge – thickness measurement in the centre	100-60%
13	Wait – thickness measurement in the centre	60%
14	Thickness measurement of the whole surface	60%
15	Discharge – thickness measurement in the centre	60-30%
16	Wait – thickness measurement in the centre	30%
17	Thickness measurement of the whole surface	30%
18	Discharge – thickness measurement in the centre	30-0%
19	Wait – thickness measurement in the centre	0%
20	Thickness measurement of the whole surface	0%

Cell charging and discharging is carried out through the cyclic station shown in Appendix 9A.1.3. During charging and discharging periods the thickness measurement is performed at the centre of the cell at a frequency of 0.2 Hz. This measurement gives a clearer view of how the thickness change evolves. Current and time are used as references to achieve the SOCs under investigation. In particular, since the cell has a capacity of 60 Ah when the cell is charged with 1 C the current (in the CC phase) is 60 A, when it is charged at 0.5 C the current is 30 A. The following formula is used to derive the required charge or discharge time:

$$t = 3600 \cdot \frac{C \cdot CR}{I} \cdot p$$

With:

- t = time [s]
- C = capacity [Ah]
- CR = capacity retention $0 \leq CR \leq 1 = fresh\ cells$ (see Chapter 3.4)
- I = current [A]
- p = amount in percentage to be charged/discharged $0 \leq p \leq 1$

The relevant times for the tested cells are listed in Table 4-2.

Table 4-2 The times in seconds to charge or discharge cells at 1 C and 0.5 C by 30% or 40%. The difference in capacity is related to the fact that the first three cells are fresh and the last four are aged.

Cell	**Capacity [%]**	**C/D time 30% -1C**	**C/D time 40% -1C**	**C/D time 30% -0.5C**	**C/D time 40% -0.5C**
1	100.0	1080	1440	2160	2880
2	100.0	1080	1440	2160	2880
3	100.0	1080	1440	2160	2880
4	85.7	926	1234	1851	2468
5	67.1	725	966	1449	1932
6	81.7	882	1176	1765	2353
7	70.1	757	1009	1514	2019

The last step of charging (from 90% SOC to 100% SOC) or discharging (from 30% SOC to 0% SOC), instead of using the time as a reference, the current is taken, imposing that the current must be less than or equal to 3 A to consider the cell fully charged or discharged.

The testing procedure is shown schematically in Figure 4-5. First, there is the preparation phase where the axes of the testbed are calibrated and then the capacitive sensors are checked to ensure that they are at a proper distance from the cell throughout the entire surface. Then a script is executed which coordinates the movement of the testbed axes with the distance measurement of the two sensors and the measurement of the entire surface is performed. Once the surface measurement has been completed, another script is executed which brings the sensors to the centre of the cell and measures at a frequency of 0.2 Hz, while via the cycling station the desired charge/discharge cycle is performed. Once the charge/discharge cycle is complete, the thickness measurement at the centre of the cell is stopped and, after waiting for the relaxation period, the surface measurement script is re-run. This process is repeated until the end of the entire cycle.

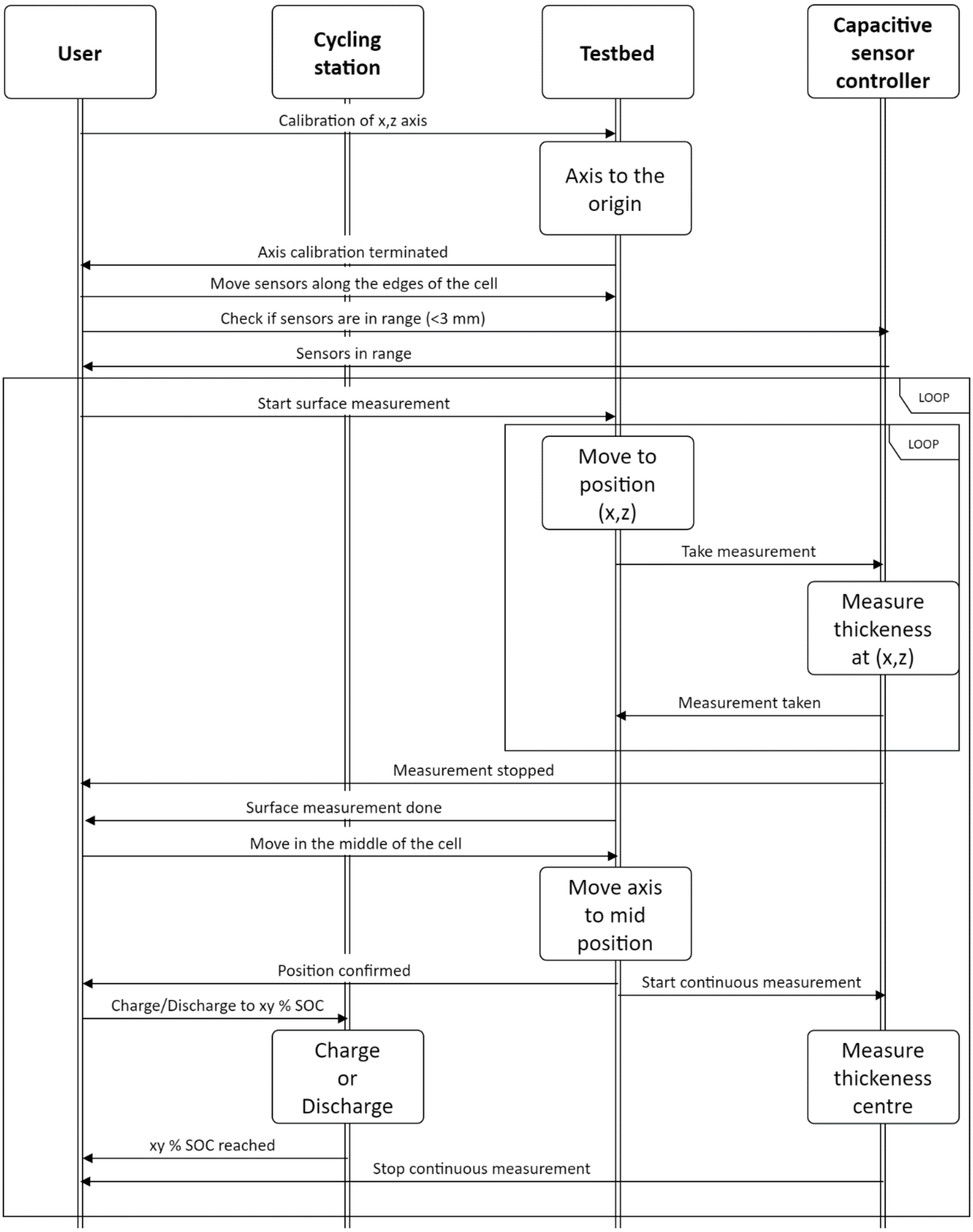

Figure 4-5 Sequence diagram of the thickness evaluation experimental procedure.

The first experimental part consists of measuring three fresh cells charged at 1 C, each of which is tested for three cycles, after which the same cells are measured while charged at 0.5 C for two cycles. The total number of complete cycles is 15, of which 9 are at 1 C and 6 at 0.5 C, as listed in Table 4-3.

Table 4-3 Summary of cycles for fresh cells.

Charging rate	1 C	0.5 C
N° of cells	3	3
N° of cycles per cell	3	2
Total n° of cycles	9	6

The second part involves measuring the thickness of four cells aged, employing two different procedures, details of the ageing methodology can be seen in Table 3-4. Measurements are taken at 1 C and 0.5 C for two cycles. The total number of complete cycles is 16, of which 8 are at 1 C and 8 at 0.5 C, as listed in Table 4-4.

Table 4-4 Summary of cycles for aged cells.

Charging rate	1 C	0.5 C
N° of cells	4	4
N° of cycles per cell	2	2
Total n° of cycles	8	8

4.2 Results

4.2.1 Single point measurement in the centre of fresh cells

The measurement at the centre of the cell is carried out during the charge and discharge phases. In Figure 4-6 there is an example of a cycle, in which the state of charge is related to the percentage increase of thickness taking as reference the cell at 0% SOC. A more in-depth analysis is represented in Figure 4-7 which there is the maximum, the minimum and the arithmetic mean of all the cycles performed with C-rate equal to 1 and, similarly for Figure 4-8 but for the cycles performed at 0.5 C. It can be observed that there is a strong correlation between the state of charge and the increase in cell thickness. It is also interesting to note the presence of overshoot for the cycles carried out at 1 C, on the contrary when the cell is charged at 0.5 C this phenomenon does not occur.

It can therefore be concluded that:

- The peak value for cycles charged with C-rate 1 is reached at 90%, due to the presence of overshoot, and is approximately 3.2% of the initial thickness.
- The peak value for cycles charged with C-rate 0.5 is reached at 100%, due to the absence of overshoot, and is approximately 3% of the initial thickness.

- Cells charged at 1 C and 0.5 C behave similarly in terms of increased thickness, except for the arising of overshoot. The increase in the thickness of the fully charged cell is about 3% for both C-rates.
- The distance of the maximum and minimum at 1 C is greater than at 0.5 C.

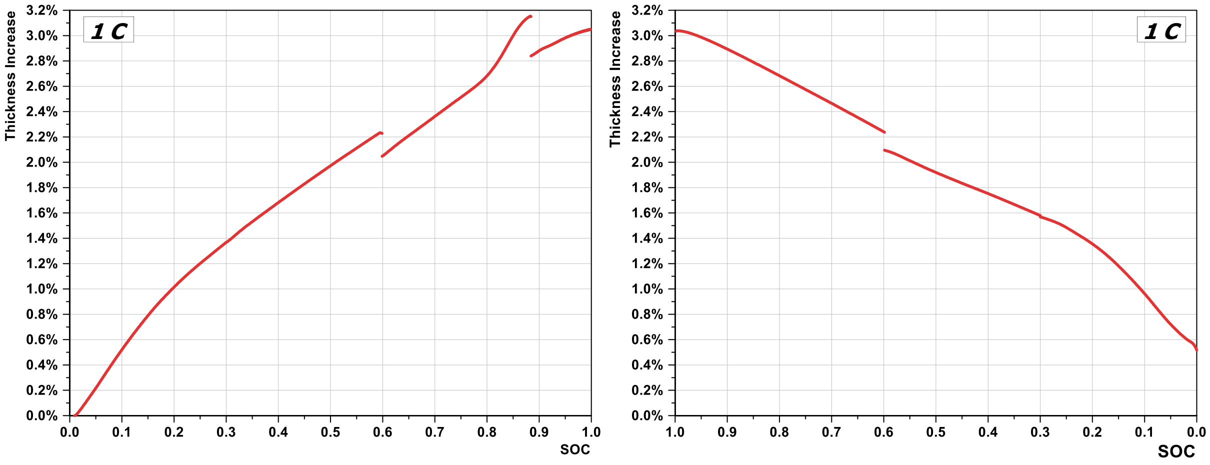

Figure 4-6 Example of thickness changes in the centre of cell 1 charged (left) and discharged (right) with 1 C.

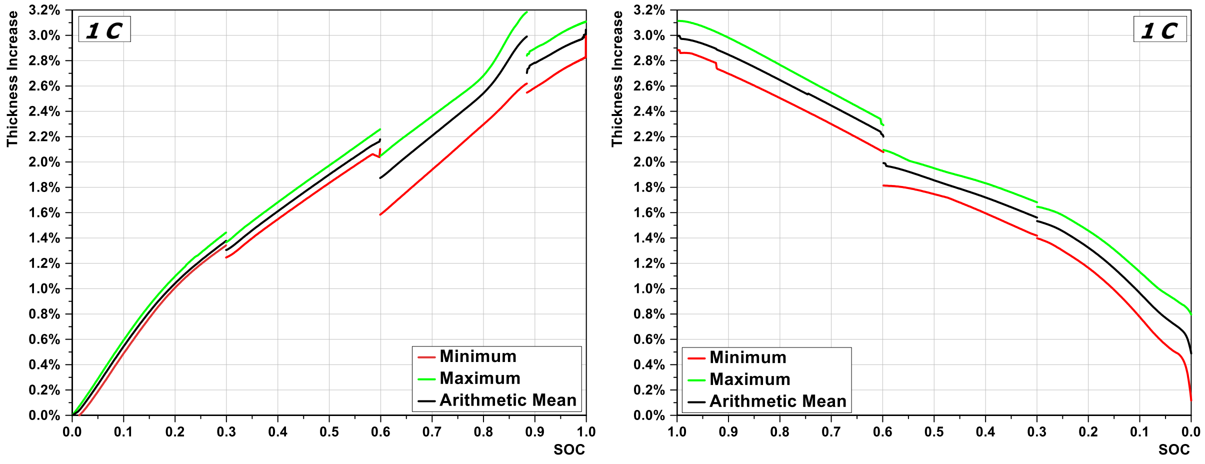

Figure 4-7 Analysis of thickness changes in the centre of all fresh cells charged (left) and discharged (right) with 1 C.

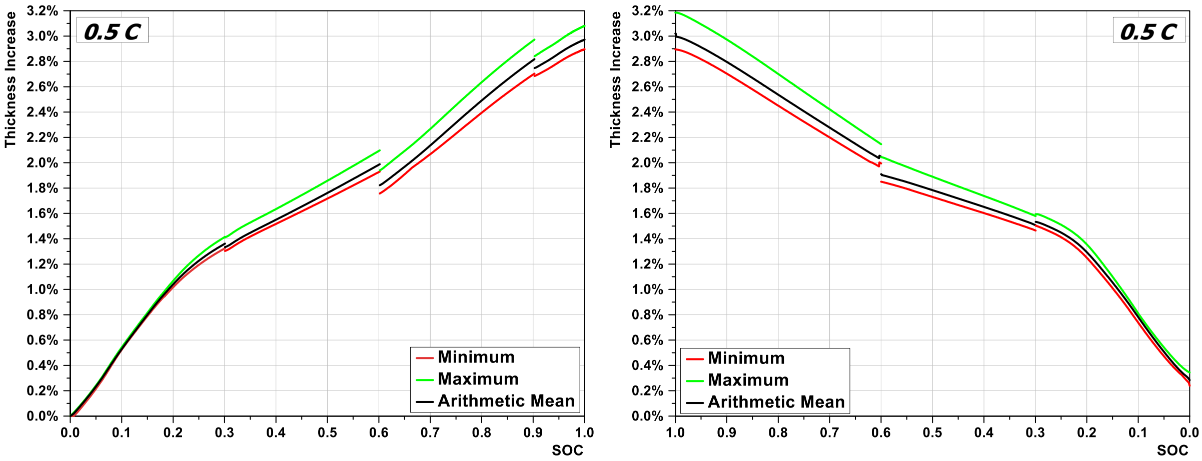

Figure 4-8 Analysis of thickness changes in the centre of all fresh cells charged (left) and discharged (right) with 0.5 C.

4.2.2 Surface measurement of fresh cells

The surface area is measured at the end of the relaxation period. Figure 4-9 shows the evolution of the thickness change at different SOCs up to 100%, Figure 4-10 and Figure 4-11 illustrate the statistical behaviour of all cycles under investigation at 1 C and 0.5 C. In particular, the point of maximum percentage increase (green), the point of minimum increase (red) and the arithmetic mean (blue) were considered for each SOC under study compared to the 0% SOC state.

From the results collected, it can be noted that:

- The highest percentage increase in thickness is found at 100% SOC.
- The increase in percentage thickness is mainly in the centre of the cell and decreases moving towards the edges, the peak values are at about 3.1%.
- The average increase in thickness from 0% to 100% SOC is approximately 2.9% for both cells charged at 1 C and cells charged at 0.5 C.
- The statistical behaviour of the cells charged at 1 C and 0.5 C follows a similar pattern, however with higher C-rates the variability of the outcome increases.
- The average of the difference between the point of maximum increase in per cent thickness and the minimum increase in per cent thickness is 0.50% for cells charged with 1C and 0.39% for cells charged with 0.5C.

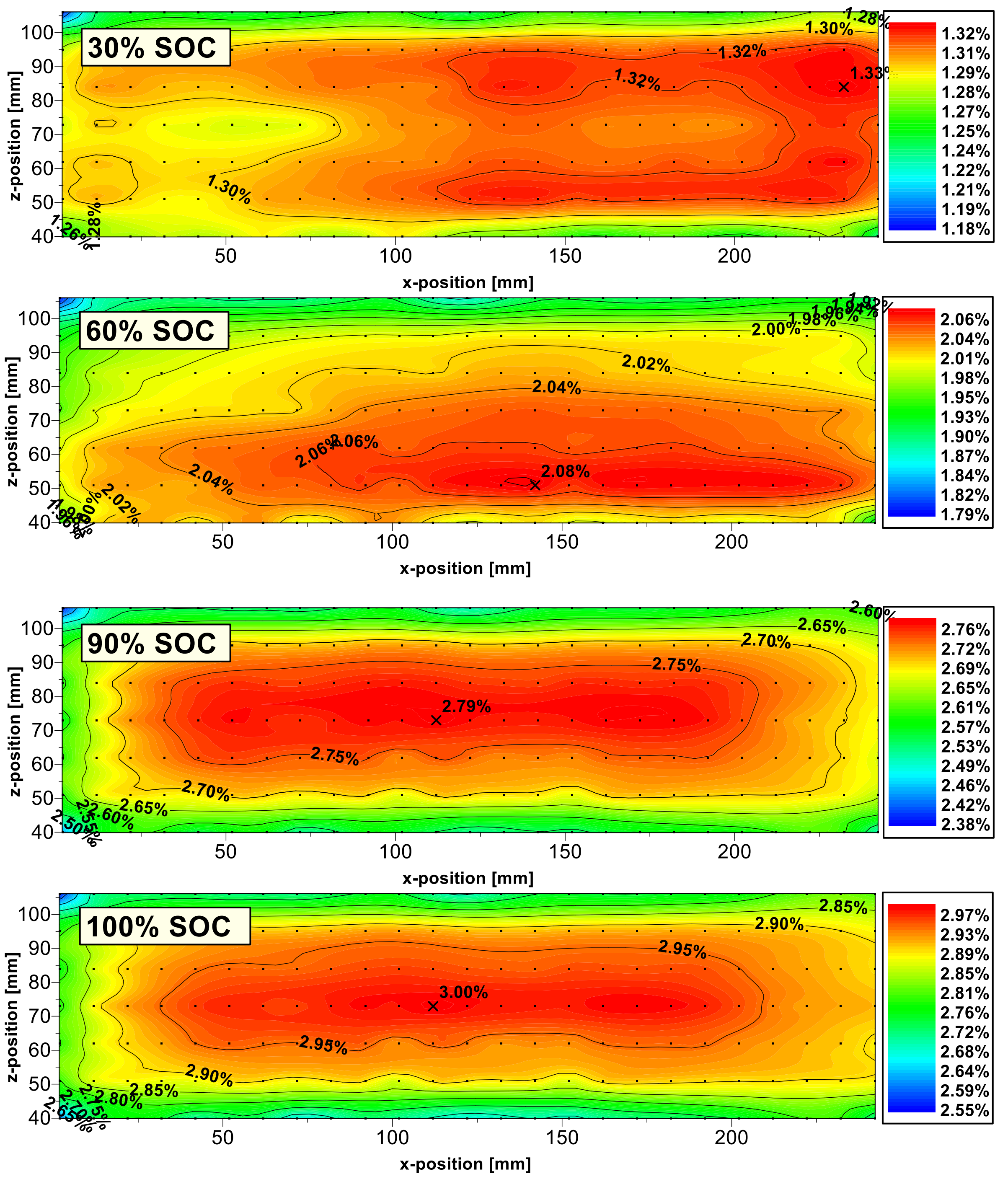

Figure 4-9 Evolution of thickness in a fresh cell increase for different SOCs considering the 0% SOC as reference.

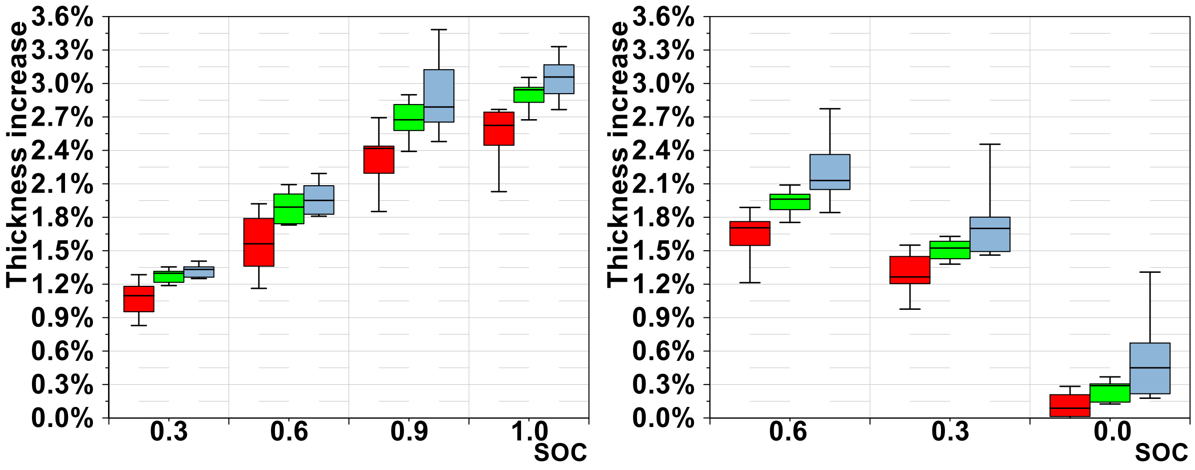

Figure 4-10 Analysis of thickness changes considering the maximum (blue), the minimum (red) and the average (green) of all points of the surface at different SOC of all fresh cells cycled with 1 C, during charging (left) and during discharging (right).

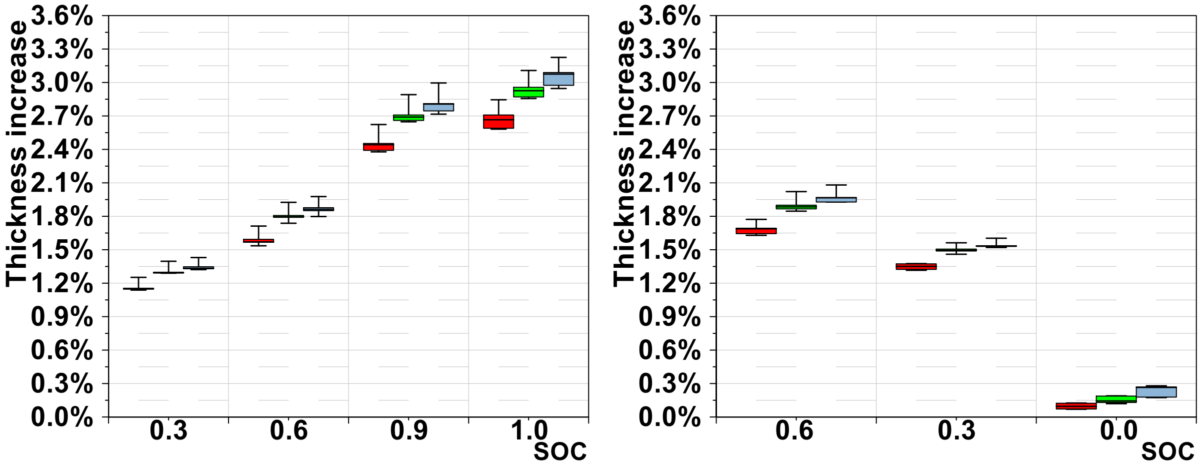

Figure 4-11 Analysis of thickness changes considering the maximum (blue), the minimum (red) and the average (green) of all points of the surface at different SOC of all fresh cells cycled with 0.5 C, during charging (left) and during discharging (right).

4.2.3 Single point measurement in the centre of aged cells

The measurement is taken, as in the case of fresh cells, at the centre with a frequency of 0.2Hz during charging and discharging. Figure 4-12 shows an example of the cell thickness change in a cycle. Ageing affects cell swelling. The percentage increase in thickness is less than for fresh cells, indeed the average increase in thickness from 0% to 100% SOC for fresh cells was 2.33% and for aged cells 2.39%. However, it should be noted that aged cells have greater irreversible swelling and thus greater initial absolute thickness. Another note can also be made about the non-occurrence of overshoot in the case of aged cells, even if charged with 1C.

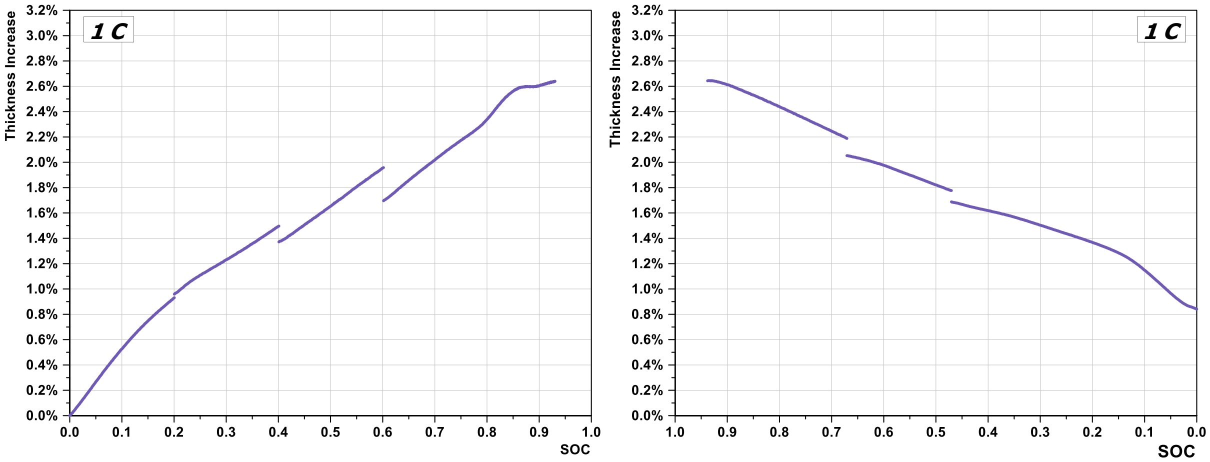

Figure 4-12 Thickness increase of cell number 5 (see Table 3-4) upon charging and discharging at 1C.

4.2.4 Surface measurement of aged cells

For the analysis of aged cells, the approach was similar to that for fresh cells. Figure 4-13 shows the evolution of the increase in thickness during charging. Figure 4-14 and Figure 4-15 show the statistical behaviour of cells charged with a C-rate of 1 and 0.5. The green boxplot refers to the maximum value, the red boxplot to the minimum and the blue boxplot to the average of all points measured along the surface for that SOC for that cycle. The highlights obtained from these measurements are:

- As with fresh cells, the maximum increase in percentage thickness is achieved at 100% SOC.
- The maximum percentage increase is at the edges of the cell, after that the maximum percentage increase is in the centre of the cell. This particular configuration results in the minimum points being arranged along a frame around the centre of the cell. The average peak value is around 2.7%.
- The average value of thickness increase for the various cycles is about 2.4%, for both 1 C and 0.5 C.
- The statistical behaviour of cells charged with 1 and with 0.5 C is on average very similar. The variability of the results, especially during discharge, is greater at higher C-rates.
- The difference between the point of maximum percentage increase and minimum percentage increase when the cell is fully charged compared to the empty cell is 0.69%, which is higher than for fresh cells.

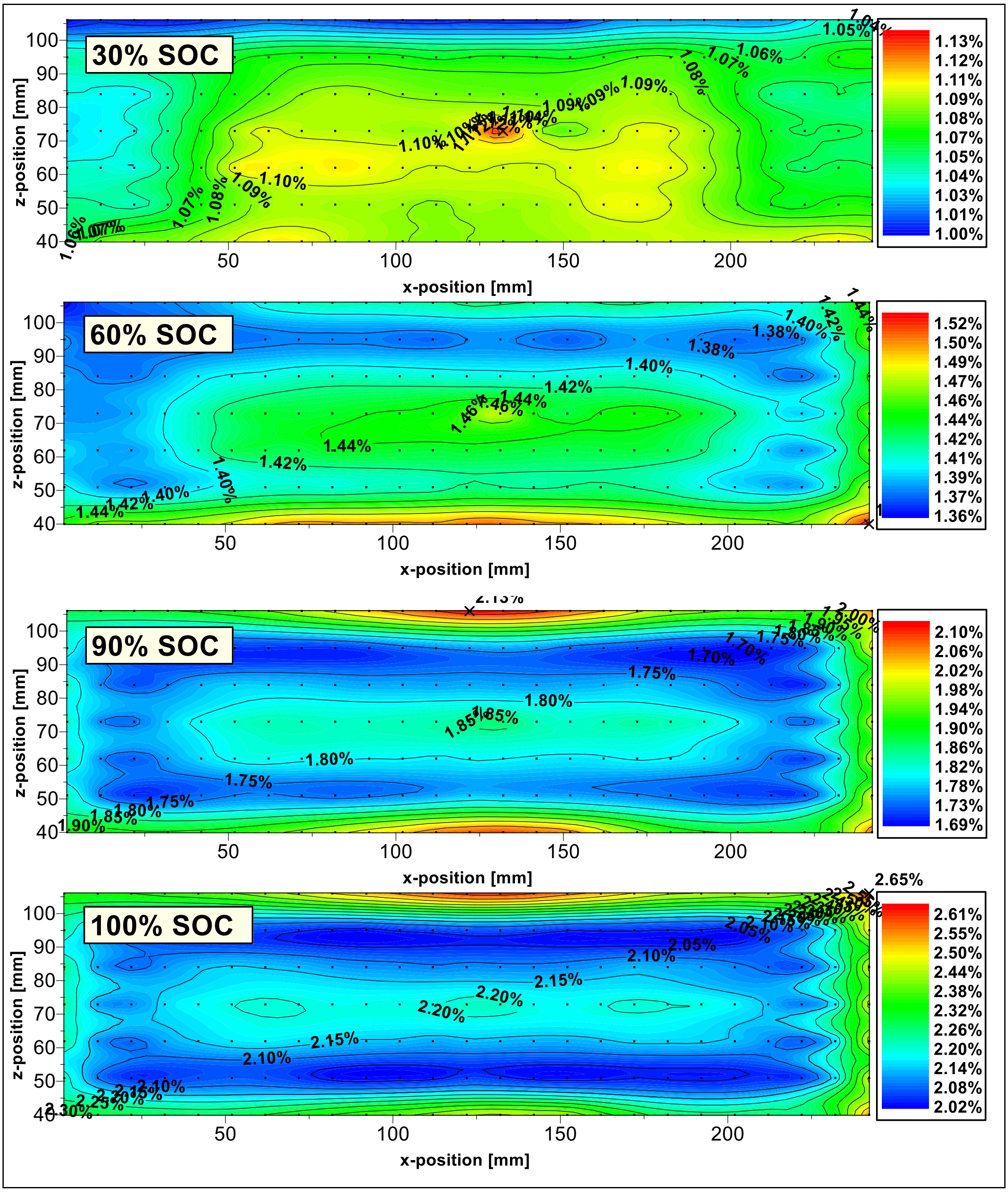

Figure 4-13 Evolution of thickness in an aged cell increase for different SOCs considering the 0% SOC as reference.

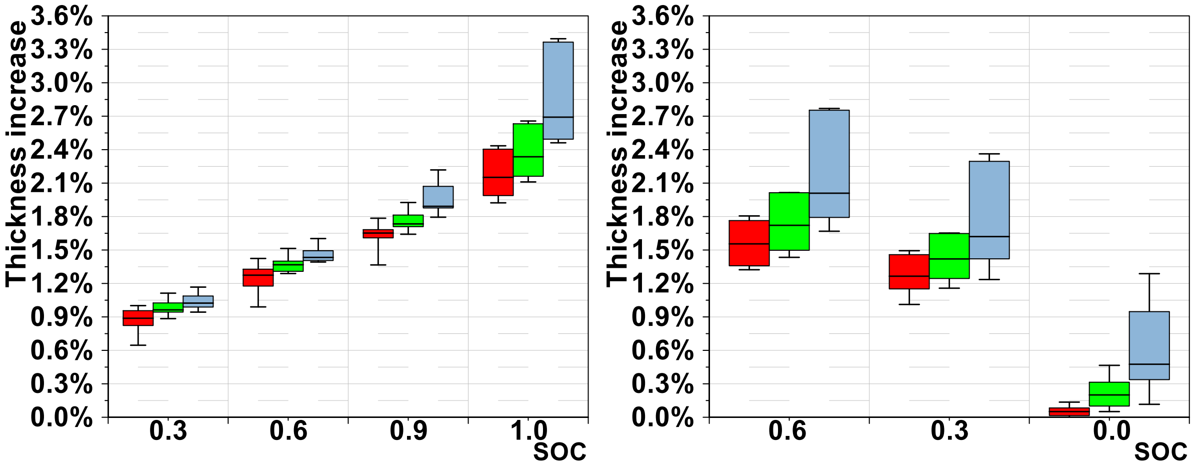

Figure 4-14 Analysis of thickness changes considering the maximum, the minimum and the average of all points of the surface at different SOC of all aged cells cycled with 1 C, during charging (left) and during discharging (right).

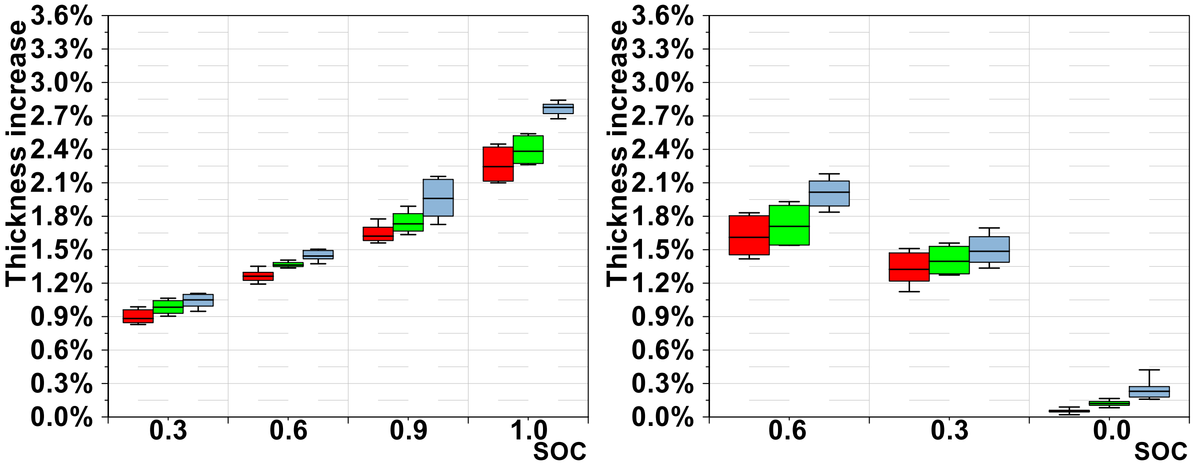

Figure 4-15 Analysis of thickness changes considering the maximum, the minimum and the average of all points of the surface at different SOC of all aged cells cycled 0.5 C, during charging (left) and during discharging (right).

4.2.4.1 Ageing method impact on the mechanical response

The results obtained with the ages cells are resumed in Table 4-5 when charged with 1 C and Table 4-6 when charged with 0.5 C.

Table 4-5 Comparison of the thickness properties for aged cells charged with 1 C.

Cell	**Absolute thickness at 0% SOC [mm]**			**Absolute thickness at 100% SOC [mm]**			**Thickness Increase from 0 to 100% SOC [%]**			
	Min.	Max.	Avr.	Min.	Max.	Avr.	Min	Max	Avr.	max-min Δ
4	14.26	14.83	14.56	14.59	15.15	14.88	2.05	2.46	2.18	0.41
	14.27	14.94	14.61	14.61	15.24	14.92	1.92	2.50	2.11	0.57
5	14.21	14.56	14.45	14.61	15.00	14.83	2.42	3.39	2.64	0.98
	14.25	14.64	14.48	14.64	15.06	14.86	2.43	3.36	2.62	0.93
6	14.29	14.72	14.61	14.64	15.08	14.93	2.03	2.65	2.21	0.62
	14.31	14.74	14.62	14.65	15.09	14.93	1.94	2.49	2.14	0.55
7	14.19	14.61	14.44	14.59	15.03	14.82	2.39	3.37	2.66	0.98
	14.26	14.71	14.50	14.61	15.07	14.85	2.25	2.73	2.46	0.48

Table 4-6 Comparison of the thickness properties for aged cells charged with 0.5 C.

Cell	**Absolute thickness at 0% SOC [mm]**			**Absolute thickness at 100% SOC [mm]**			**Thickness Increase from 0 to 100% SOC [%]**			
	Min.	Max.	Avr.	Min.	Max.	Avr.	Min	Max	Avr.	max-min Δ
4	14.25	14.90	14.58	14.61	15.23	14.91	2.11	2.67	2.26	0.56
	14.27	14.86	14.60	14.63	15.20	14.93	2.12	2.68	2.27	0.56
5	14.26	14.68	14.52	14.65	15.06	14.88	2.44	2.81	2.53	0.38
	14.28	14.68	14.52	14.66	15.06	14.89	2.45	2.84	2.54	0.39
6	14.31	14.75	14.63	14.68	15.11	14.96	2.12	2.79	2.30	0.66
	14.31	14.75	14.63	14.68	15.12	14.96	2.10	2.77	2.28	0.67
7	14.26	14.69	14.51	14.63	15.07	14.87	2.40	2.79	2.52	0.39
	14.26	14.71	14.52	14.63	15.07	14.88	2.37	2.76	2.47	0.40

Cells 4 and 6 aged with a lower pretension and for a higher number of cycles than cells 5 and 7 (see Table 3-4), showed less loss in terms of capacity but more irreversible swelling (see Figure 4-16). This behaviour is related to the fact that although cells 5 and 7 suffered more lithium plating, the high pressure acting on the cell reduced the development of irreversible swelling.

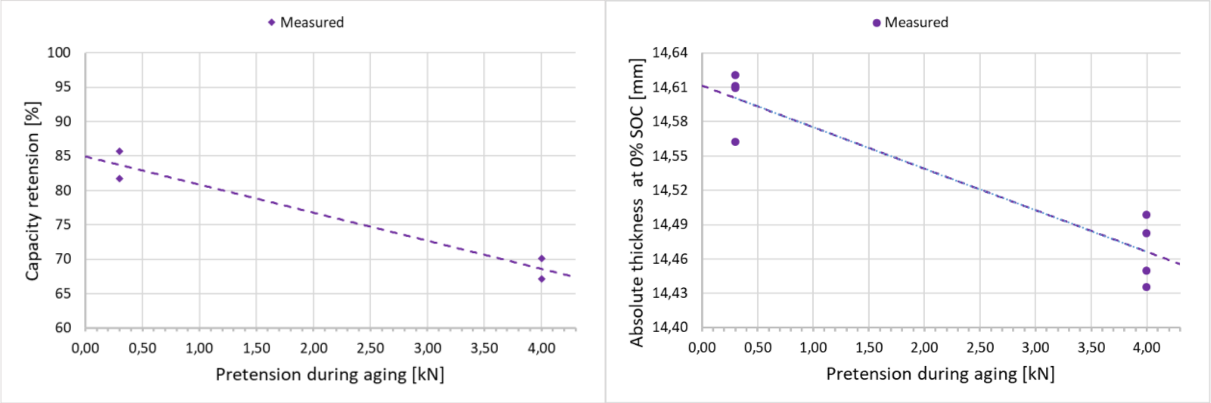

Figure 4-16 Ageing strategy impact on capacity retention (left) and on irreversible swelling (right). The purple dots are the measured points, the dashed curve is the trend line that follows a linear regression between the measured points.

At the end of the charge, cells 4 and 6 showed a greater absolute thickness than cells 5 and 7 (see Figure 4-17), although a lower percentage thickness increase (see Figure 4-18).

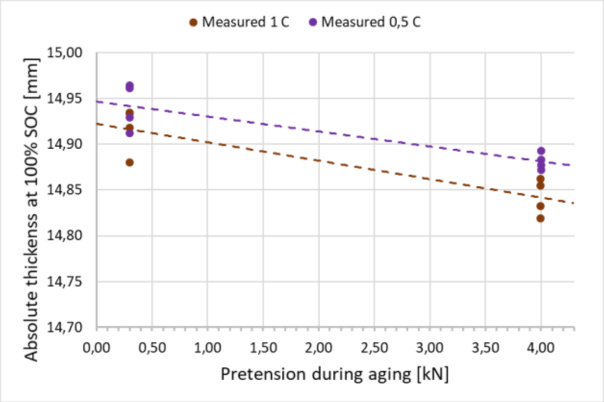

Figure 4-17 Ageing strategy impact on the absolute final thickness, the dots are the measured points. The dashed curve is the trend line that follows a linear regression between the measured points.

Finally, as shown in Figure 4-18, cells 5 and 7 compared to cells 4 and 6 showed mixed behaviour in terms of the difference between the maximum and minimum point of percentage growth from 0% SOC to fully charged.

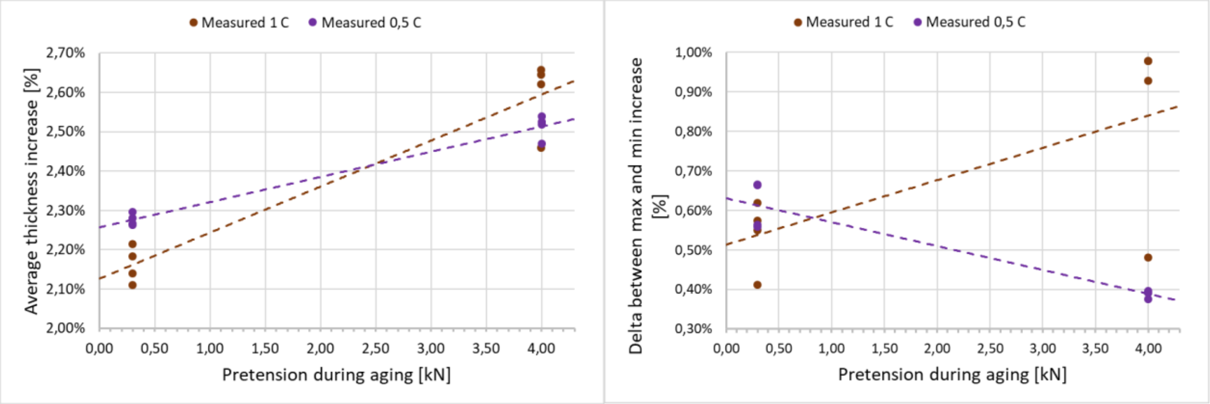

Figure 4-18 Ageing strategy impact on average thickness increase (left) and the difference between the maximum and the minimum percentage increase (right). The dots are the measured points, the dashed curve is the trend line that follows a linear regression between the measured points.

5 BREATHING & SWELLING IN PRETENSIONED CELLS

5.1 Method

The intensity and distribution of pressure are measured during a charge and discharge cycle of a cell subjected to a certain pretension. The constraint applied to the cell allows the stresses to evolve and not the change in cell thickness. The pressure analysis is performed by the data acquisition system (DAQ) presented in Appendix 9A.1.4. The cell is fixed to the same testbed used for non-pretensioned cells, however, in this case, it is fixed in a new configuration and is parallel to the plane of the testbed (see 9A.1.2.2) and is compressed by an aluminium plate. The configuration used to perform the measurements is shown in Figure 5-1 and consists of several layers. Starting from the bottom, in contact with the testbed:

- An aluminium block, which allows the cell to reach the clamping system.
- A layer of Pertinax, which provides electrical insulation between the cell and the metal block below it.
- Two compression pads (made of PORON® 4701-60 Polyurethane) are placed below and above the cell (see Figure 5-2), their surface area is smaller than that of the cell, which makes it possible to minimise the effect of bumps at the edges of the cell (see Chapter 3.2) and to obtain more precise measurements on the inner surface (see Chapter **Error! Reference source not found.**).
- The pressure mat through which the local pressure is distributed.
- An aluminium plate is attached to the z-axis of the testbed and allows the cell to be compressed with the pretension being tested.

The dimensions of the layers are summarised in Table 5-1.

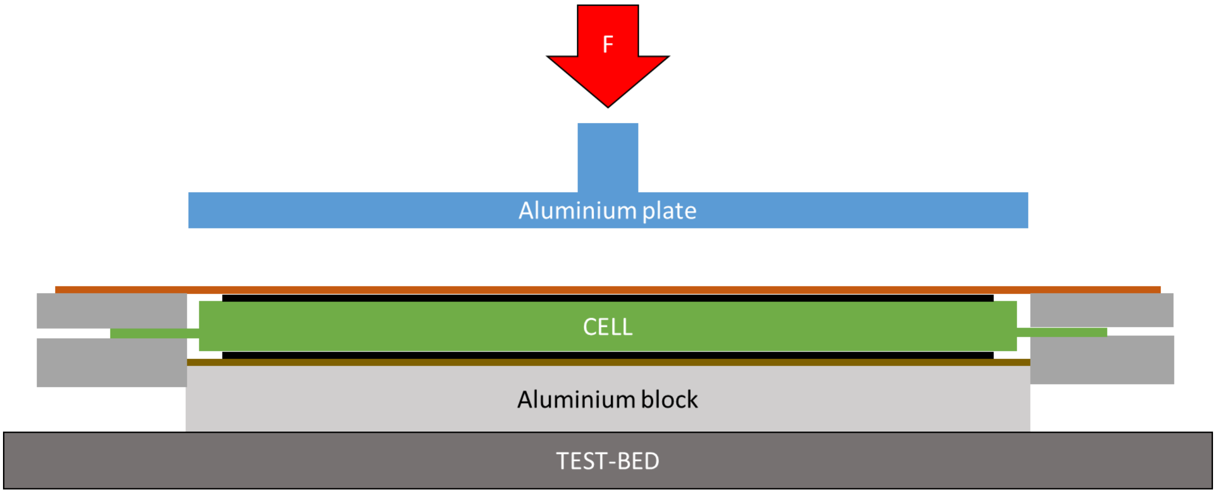

Figure 5-1 Schematic view of the testbed setup. For the layers without a label: the brown layer is Pertinax, the black layers are compressions pads and the orange layer is the pressure pad.

Figure 5-2 Compression pad positioned above the cell, the surface covered by the compression pad is smaller than that of the cell.

Table 5-1 Dimensions of configuration layers for the set of experiments with pretensioned cells.

Layer	Length [mm]	Width [mm]	Height [mm]
Aluminium block	300	125	30
Pertinax	300	125	3
Compression pads	250	80	2
Cell	260	90	15
Pressure mat	338	154	< 1
Aluminium plate	285	100	10

The charge-discharge cycle used begins after a waiting period of 30 minutes after the application of the pretension on the cell with 30% SOC. Cycle charging and discharging is performed at 0.5 C and the steps are shown in Table 5-2.

Table 5-2 Steps of the full cycle with pretensioned cells.

Step	Action	State of charge
0	Apply pretension and wait 30 minutes	30%
1	Discharge	30-0%
2	Wait 15 minutes	0%
3	Charge	0-30%
4	Wait 15 minutes	30%
5	Charge	30-60%
6	Wait 15 minutes	60%
7	Charge	60-90%
8	Wait 15 minutes	90%
9	Charge	90-100%
10	Wait 15 minutes	100%
11	Discharge	100-60%
12	Wait 15 minutes	60%
13	Discharge	60-30%
14	Wait 15 minutes	30%

The entire cycle is controlled by the same cycling station used for non-pretensioned cells, see Appendix 9A.1.3. The current and voltage profiles are shown graphically in Figure 5-3. The test procedure is similar to that seen for the measurement of the thickness of non-pretensioned cells seen in Chapter 4. This makes it easier to compare the results obtained.

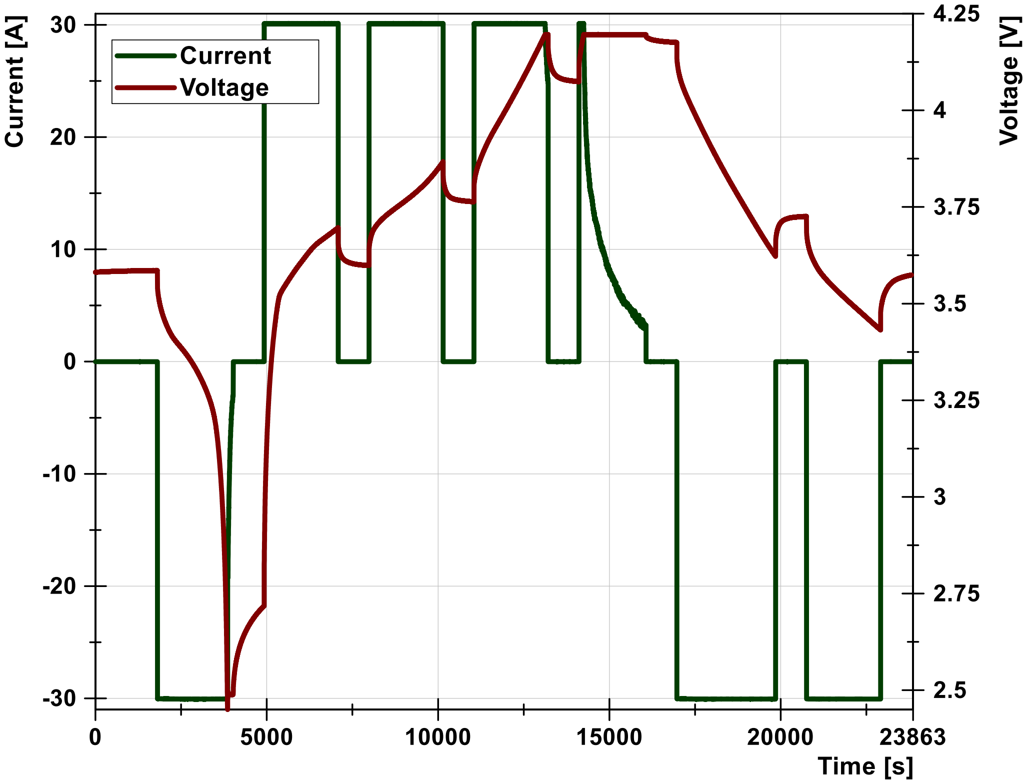

Figure 5-3 Current and voltage curves for a full test cycle with pretensioned cells.

The testing procedure is shown schematically in Figure 5-4. At the beginning of each cycle, the load cell is calibrated and the sensitivity of the pressure sensor system is adjusted. Once the preparation phase is complete, the pressure measurement programme and the complete charge/discharge cycle are started. Before starting the actual cycle, the cycling station communicates with the testbed to apply the proper pretension. Once the testbed communicates to the cycling station that the pretension has been applied, the cycle in Table 5-2 begins. At the end of the cycle, the pressure measurement system is manually interrupted by the user. At the end of the procedure, it is possible to continue with a new cycle or restart the testing procedure with a new cell.

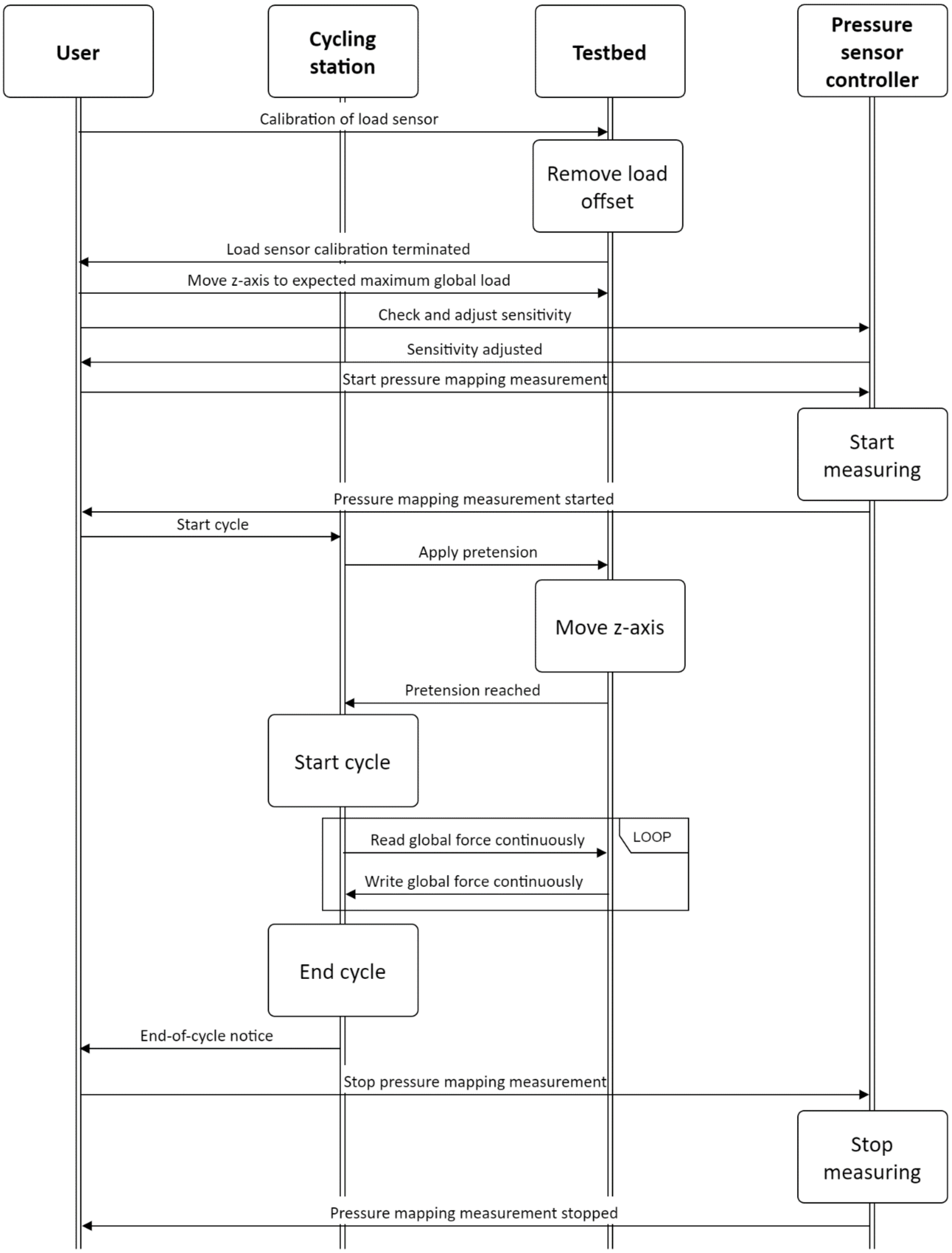

Figure 5-4 Sequence diagram of the pressure distribution evaluation experimental procedure.

The tests were carried out for two different pretension levels, namely 300 N and 4000 N, for two fresh and two aged cells. The cells tested are the same as those used in the experiments without pretension in the previous chapter and correspond to 2 and 3 for the fresh cells and 6 and 7 for the aged cells (see Table 4-2), cells 5 and 6 were selected since they were aged using two different ageing methods. Each scenario is tested twice in order to make the results more robust. The test matrix is shown in Table 5-3. The total number of cycles is therefore 16, 8 for fresh cells and 8 for aged cells.

Table 5-3 Test matrix for pretensioned cells. Cell number - Investigated cell. Aged - Ageing method. N° of cycles – Repetitions.

Cell number	Aged	Pretension	C-rate	N° of cycles
2	No – fresh	300 N	0.5 C	2
		4000 N	0.5 C	2
3	No – fresh	300 N	0.5 C	2
		4000 N	0.5 C	2
5	Yes (with 4 kN pretention)	300 N	0.5 C	2
		4000 N	0.5 C	2
6	Yes (with 300 N pretention)	300 N	0.5 C	2
		4000 N	0.5 C	2

5.2 Results

5.2.1 Global force profile for fresh cells

The global force during the cycle tends to increase during charging, and decrease during discharging. The maximum peak force is reached when the cell is fully charged, while the minimum value is reached when the cell is fully discharged. During the relaxation periods, while the SOC remains constant, the force tends to decrease over time. Figure 5-5 shows the trend of the SOC and the average global force of all cycles performed with the fresh cells over time. The average global force is placed between two other lines describing the maximum (green) and minimum (red) values for all cycles with fresh cells.

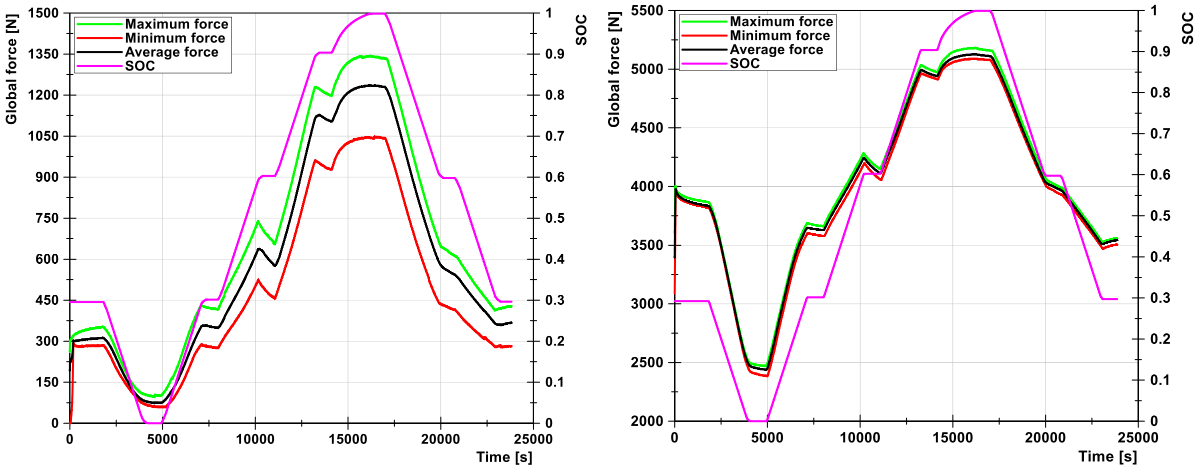

Figure 5-5 Development of SOC, the maximum global force, the minimum global force and the average global force over time considering all fresh cells pretensioned with 300 N (left) and at 4000 N (right).

The force evolution for all fresh cells tested is shown in Table 5-4. From the data collected, it can be seen that after applying pretension, there is always a settling of the overall force of about 5%. On the other hand, comparing the percentage increase from 0% to 100% SOC of cells pretensioned with 300 N with respect to those pretensioned with 4000 N, it can be seen that lower pretensions result in a higher percentage increase.

Table 5-4 Global force of fresh cells at different SOC.

Cell	Pretension [N]	Force at 30% SOC [N]	Force at 30% SOC relaxed [N]	Force at 0% SOC [N]	Force at 100% SOC [N]	Force increase
2	300	300.89	351.85	101.39	1320.97	1203%
		297.92	285.80	71.26	1042.06	1362%
	4000	3997.19	3865.78	2471.79	5106.10	107%
		4000.47	3833.99	2442.14	5078.60	108%
3	300	296.12	285.58	58.33	1219.28	1990%
		299.96	324.70	68.18	1333.08	1855%
	4000	3999.68	3816.59	2456.62	5155.33	110%
		4001.95	3821.53	2383.77	5097.71	114%

5.2.2 Global force profile for aged cells

The global force trend in the case of aged cells is similar to that for fresh cells. The global force tends to increase during charging and decrease during discharging and during the relaxation period while keeping SOC constant the force decreases. The global force trend, its maximum and minimum corridors and the state of charge over time are shown in Figure 5-6.

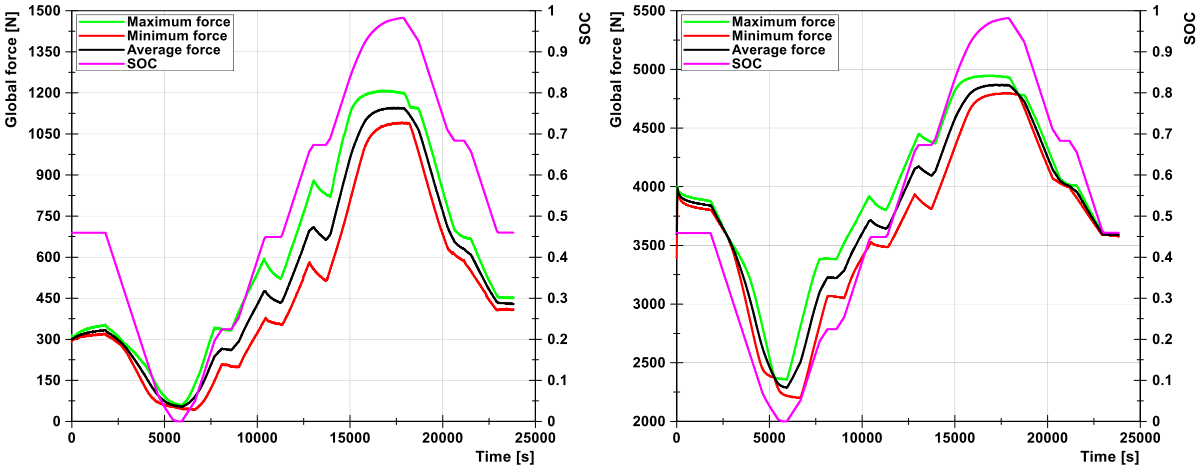

Figure 5-6 Development of SOC, the maximum global force, the minimum global force and the average global force over time considering all aged cells pretensioned with 300 N (left) and at 4000 N (right).

The force evolution for all aged cells tested is shown in Table 5-5. Similarly to fresh cells, aged cells after pretension has been applied there is a settling of the global force. Furthermore, the percentage increase in the global force of a cell charged from 0% to 100% is higher for lower pretensions than for higher pretensions.

Table 5-5 Global force of aged cells at different SOC.

Cell	Pretension [N]	Force at 30% [N]	Force at 30% relaxed [N]	Force at 0% [N]	Force at 100% [N]	Force increase
5	300	300.12	319.49	53.40	1082.73	1928%
		299.51	336.32	42.73	1144.94	2579%
	4000	3998.54	3791.98	2735.12	5322.13	95%
		3994.10	3801.71	2200.16	4779.92	117%
6	300	299.95	326.30	52.23	1134.36	2072%
		300.45	351.49	58.92	1198.84	1935%
	4000	3999.16	3896.11	2676.79	5230.41	95%
		3996.55	3878.50	2356.95	4932.89	109%

5.2.3 Pressure distribution for fresh cells

Figure 5-7 shows the pressure increase in MPa of a fresh cell pretensioned with 300 N and 4000 N. The distribution of the pressure increase suggests in both cases that the highest pressures are in the middle of the cell. An important difference emerges between the different types of pretension applied, in the case of lower pretension there is a less homogeneous distribution of pressure rise than in the cell under higher pretension. This inhomogeneity can cause higher pressure peaks despite the lower applied force.

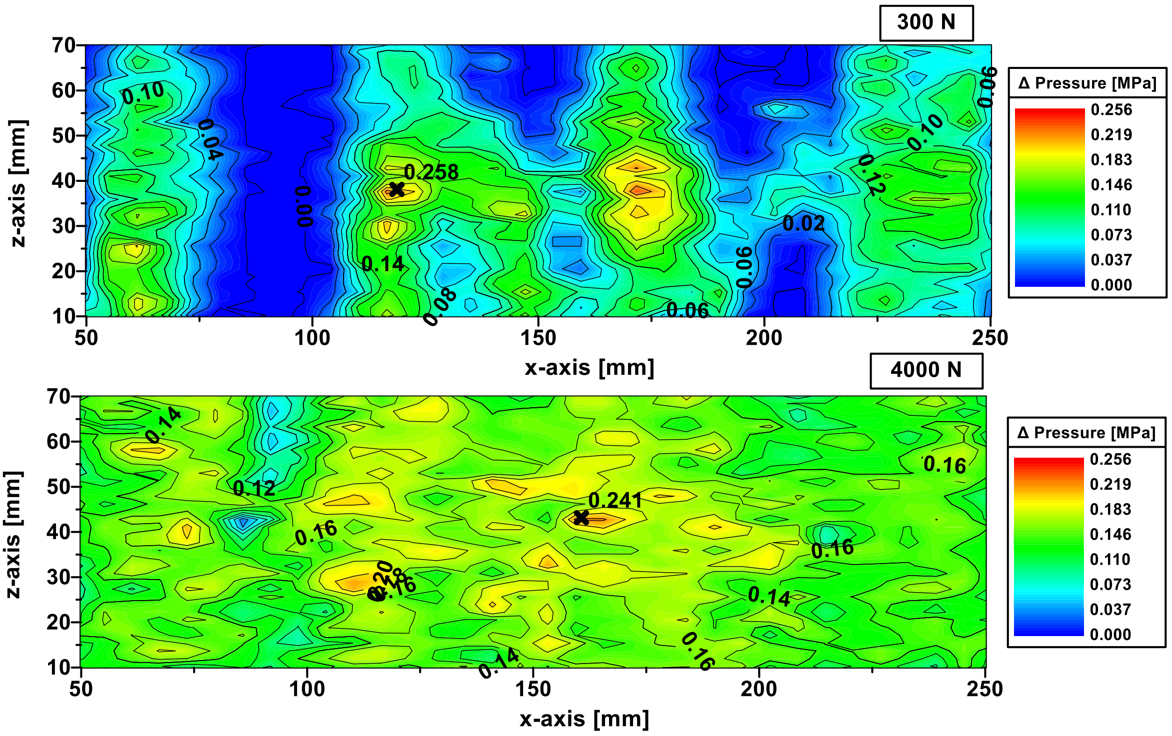

Figure 5-7 Comparison of the difference of pressure increase of a fresh cell pretensioned at 300 N (top) and 4000 N (bottom) when charged from 0% to 100%.

Table 5-6 analyses the average pressure and peak pressures measured in the fresh cells. Cells with higher pretension have the highest peak pressures, however, it is also shown that with lower pretension the pressure difference between the measured average and the peaks is higher. This suggests that in the case of higher pretension the pressures involved are higher, but the pressure distribution is more heterogeneous.

Table 5-6 Average and peak pressure of fresh cells at different SOC.

Cell	Pretension [N]	Average pressure at 100% [MPa]	Peak pressure at 0% [MPa]	Peak pressure at 100% [MPa]	Peak pressure increase
2	300	0.050	0.173	0.354	105%
		0.039	0.202	0.385	91%
	4000	0.192	0.456	0.603	32%
		0.191	0.421	0.567	35%
3	300	0.046	0.089	0.326	266%
		0.050	0.096	0.327	242%
	4000	0.194	0.412	0.573	39%
		0.192	0.399	0.564	41%

5.2.4 Pressure distribution for aged cells

Figure 5-8 shows the pressure increase in MPa of an aged cell pretensioned with 300 N and 4000 N. The distribution of the pressure increase suggests that with the lower pretension the distribution is more heterogeneous and increases as it moves away from the centre, whereas with the higher pretension the distribution of pressure increase is more homogeneous.

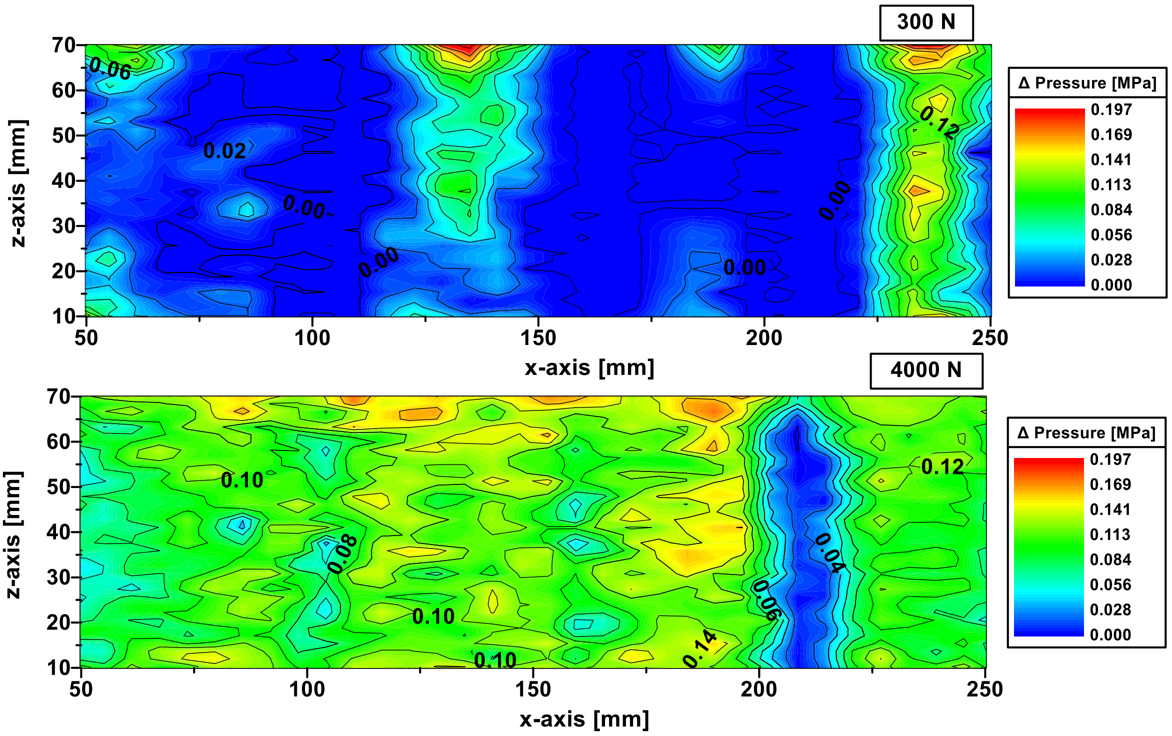

Figure 5-8 Comparison of the difference of pressure increase of an aged cell pretensioned at 300 N (top) and 4000 N (bottom) when charged from 0% to 100%.

The pressure behaviour analysed in Table 3, concerning aged cells, as in the case of fresh cells shows that peaks occur mainly at higher pretensions, but the difference between the maximum and the average pressure is more pronounced for lower pretensions, suggesting that pressure homogeneity is more prevalent for higher pretensions.

Table 5-7 Average and peak pressure of aged cells at different SOC.

Cell	**Pretension [N]**	**Average pressure at 100% [MPa]**	**Peak pressure at 0% [MPa]**	**Peak pressure at 100% [MPa]**	**Peak pressure increase**
5	300	0.041	0.121	0.314	161%
		0.043	0.103	0.322	212%
	4000	0.201	0.449	0.615	37%
		0.180	0.368	0.553	50%
6	300	0.043	0.097	0.409	320%
		0.045	0.099	0.407	310%
	4000	0.197	0.511	0.697	36%
		0.186	0.461	0.668	45%

6 EMPIRICAL MODEL

6.1 Method

The data collected is used to construct an empirical model that can later be used to develop a simulation model. The formulation of the empirical model began with a comparison of the global force versus the state of charge. As can be seen in Figure 6-1, there is a close relationship between the measured force and the state of charge; as the state of charge increases, the force increases proportionally. At the end of each charge and discharge phase, the force tends to decrease over time during the relaxation period.

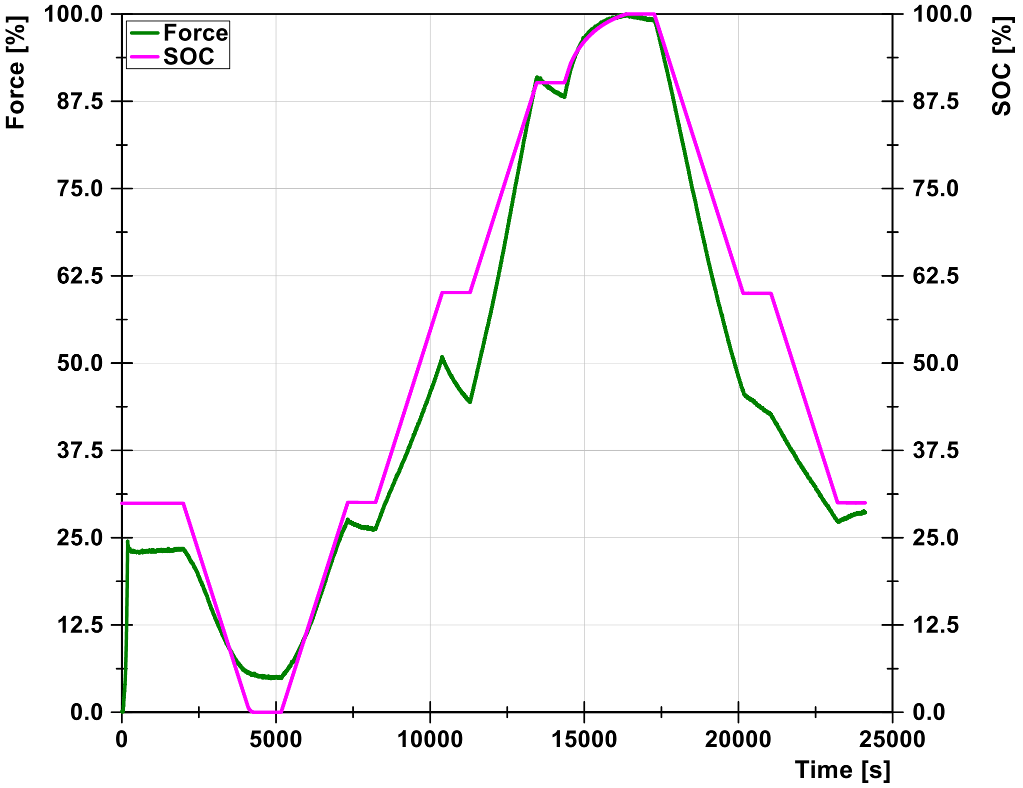

Figure 6-1 Evolution of the state of charge and global force over-time during a complete cycle.

The ratio of the force above the SOC is calculated and its development over time is studied. The ratio was calculated for all cells considered and compared for both 300 N and 4000 N pretension. The comparison is illustrated in Figure 6-2 and shows the presence of similar behaviour for all cells subjected to the same pretension.

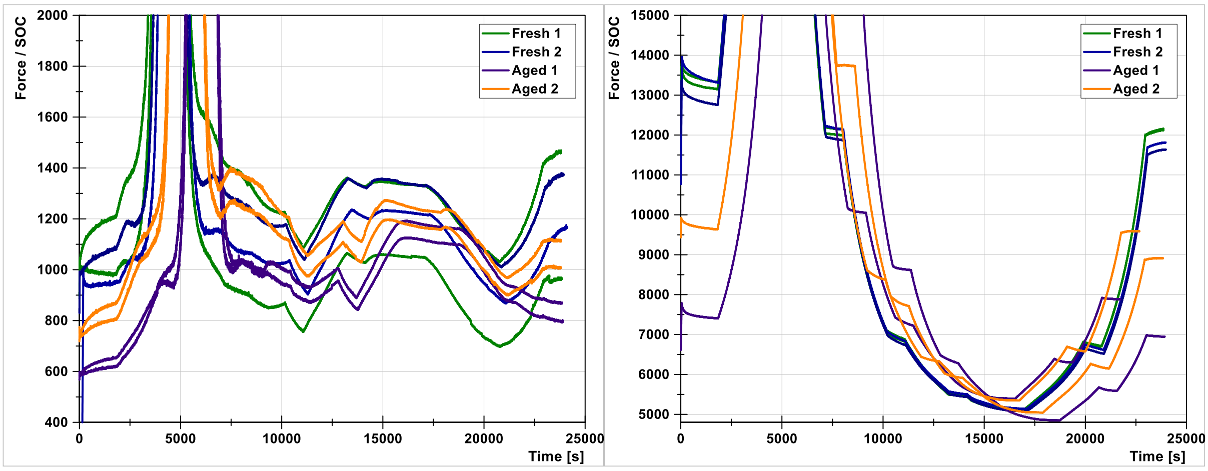

Figure 6-2 Ratio global force to SOC over time for fresh and aged cells pretensioned with 300N (left) and with 4000 N (right).

Given the analogy of the behaviour as a function of pretension, the curve is discretized into the various phases of charge, discharge and relaxation. The charging and discharging phases are studied as a function of voltage, while relaxation is studied as a function of time.

The trend in the charge and discharge phases tends to be linear, while during the relaxation phase it is exponential. The discretized phases are therefore approximated by linear regression (for charging and discharging) or exponential regression (for relaxation). The segments into which the curve is divided are shown in Figure 6-3 for the charging phase (namely 0-30% SOC, 30-60% SOC, 60-90% SOC, 90-100% SOC), Figure 6-4 for the discharging phase (namely 30-0% SOC, 100-60% SOC and 60-30% SOC) and Figure 6-5 and Figure 6-6 for the relaxing phase (namely at 30% SOC, 60% SOC, 90% SOC and 100% SOC while charging; 0% SOC, 60% SOC and 30% SOC while discharging). The figures also show the limitation of this modelling: when the SOC tends to zero, the ratio under analysis tends to infinity, thus invalidating the possibility of obtaining linear behaviour for charge states close to zero. For this reason, the regression functions were only calculated for the cycle from 30% to 100% SOC and from 100% to 30% SOC. In addition, the 90-100% SOC charging phase was divided into the constant current phase (90-100% SOC) and the constant voltage phase (90-100% SOC CV).

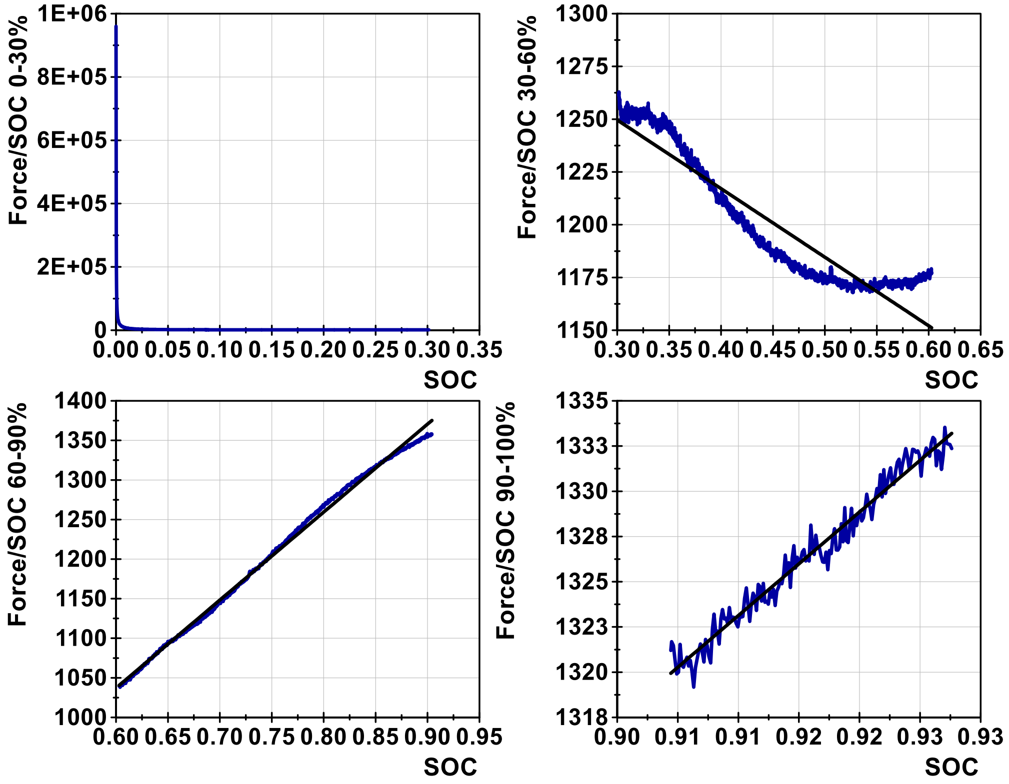

Figure 6-3 Discretized curves during the charging phases, the blue lines refer to the actual trend, the black lines to the regression function.

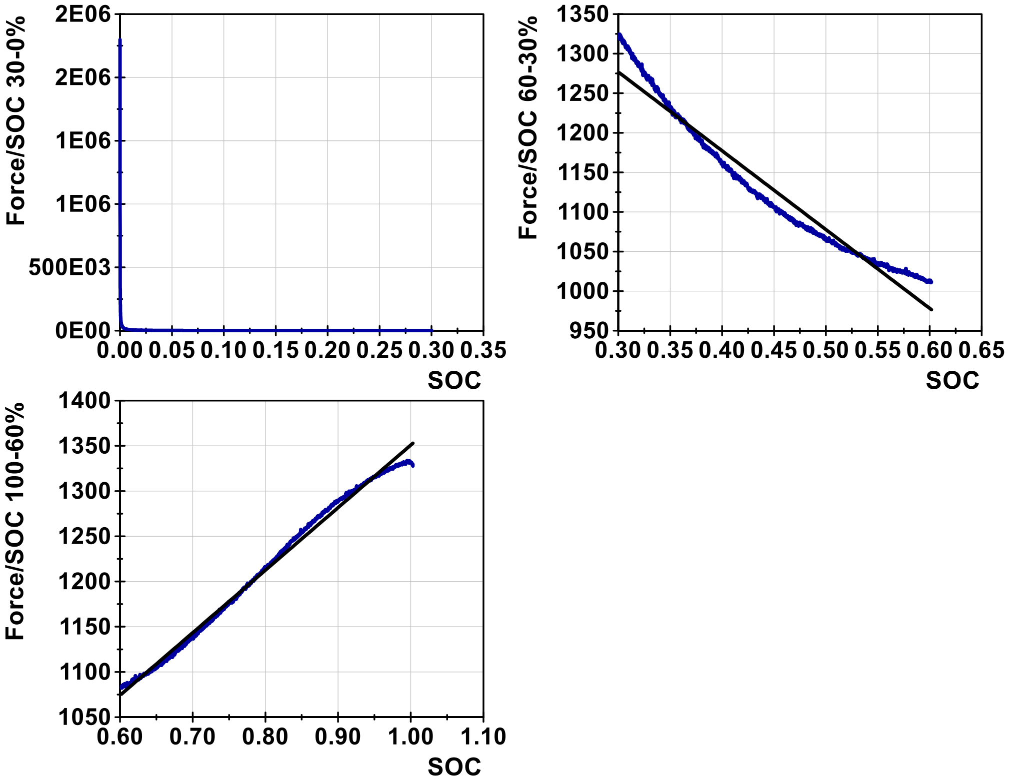

Figure 6-4 Discretized curves during the discharging phases, the blue lines refer to the actual trend, the black lines to the regression function.

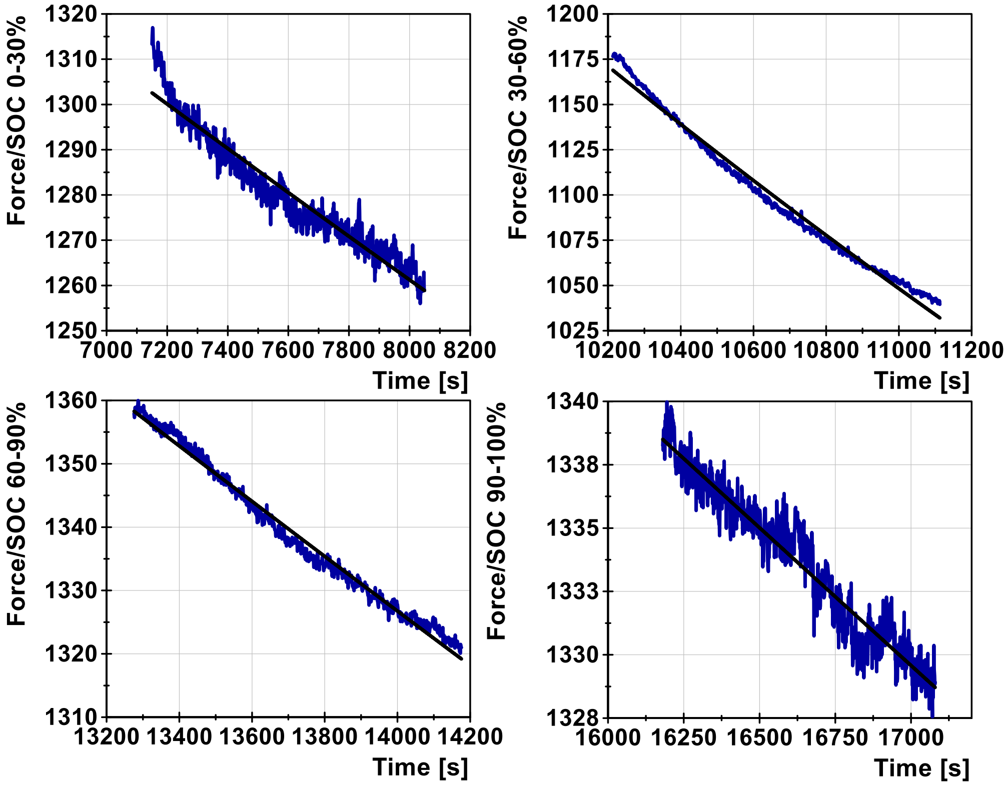

Figure 6-5 Discretized curves during the relaxation after the charging phases, the blue lines refer to the actual trend, the black lines to the regression function.

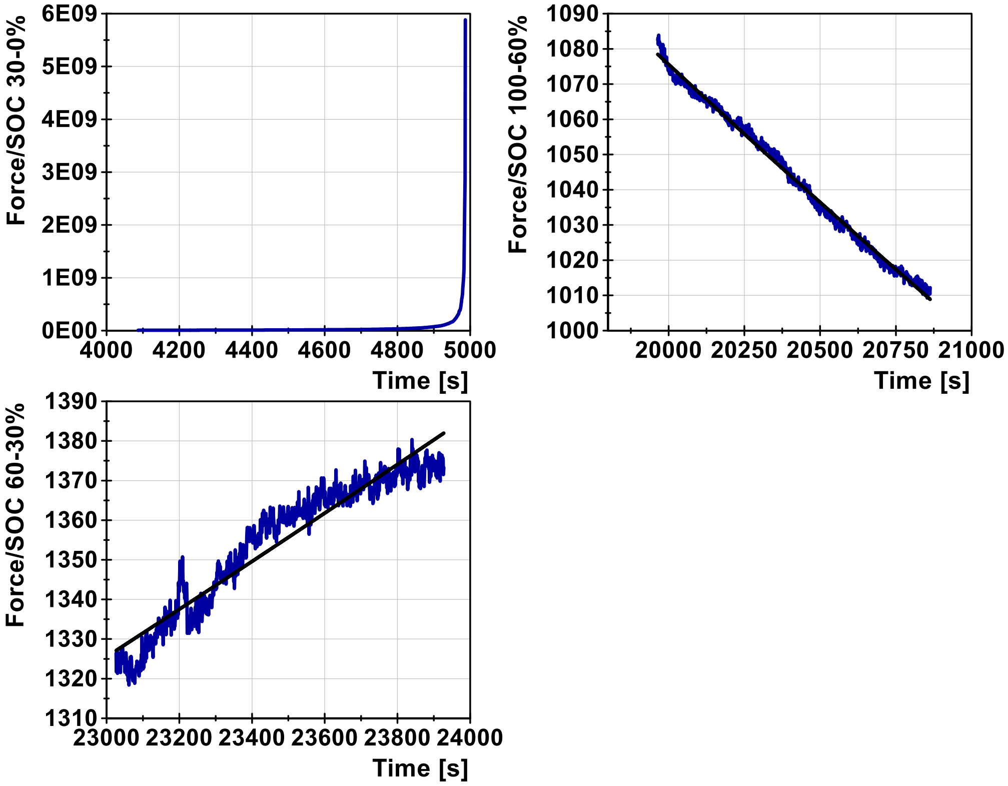

Figure 6-6 Discretized curves during the relaxation after the discharging phases, the blue lines refer to the actual trend, the black lines to the regression function.

The regression functions are then calculated and summarised in Appendix 9A.2. The coefficients a and b depend on the type of regression adopted, in particular, two possible cases have been considered:

$$Linear: y = a \cdot x + b$$

$$Exponential: y = a \cdot e^{b \cdot x}$$

Specifically in this case the formulas for the charge/discharge and relaxation phases are respectively:

$$\frac{F}{SOC} = a(P, C) \cdot SOC + b(P, C)$$

$$\frac{F}{SOC} = a(P, C) \cdot e^{b(P,C) \cdot t}$$

With:

- F = global force [N]
- SOC = state of charge
- P = pretension [N]
- C = number of cycles
- t = time [s]

To validate the equations obtained, the coefficients a and b of cells with the same boundary conditions are compared. Once the similarity of the coefficients is confirmed for cells with the same ageing level, the same SOC range and the same applied pretension, the arithmetic mean of the precision-weighted coefficients ("precision" refers to the determination coefficient R^2) of the regression function is calculated with the following formulas:

$$\frac{\sum_{1=1}^{n} w_i \cdot a_i}{\sum_i^n w_i}$$

$$\frac{\sum_{1=1}^{n} w_i \cdot b_i}{\sum_i^n w_i}$$

The trend of the two coefficients was then compared, keeping the boundary conditions constant except for the pretension. An example of the linear interpolation of the weighted average of the cluster of points of coefficient a (left) and b (right) for the charging phase from 30% to 60% SOC is shown in Figure 6-7. From the image, it is also visible that the points belonging to the cluster and their weighted average do not differ much.

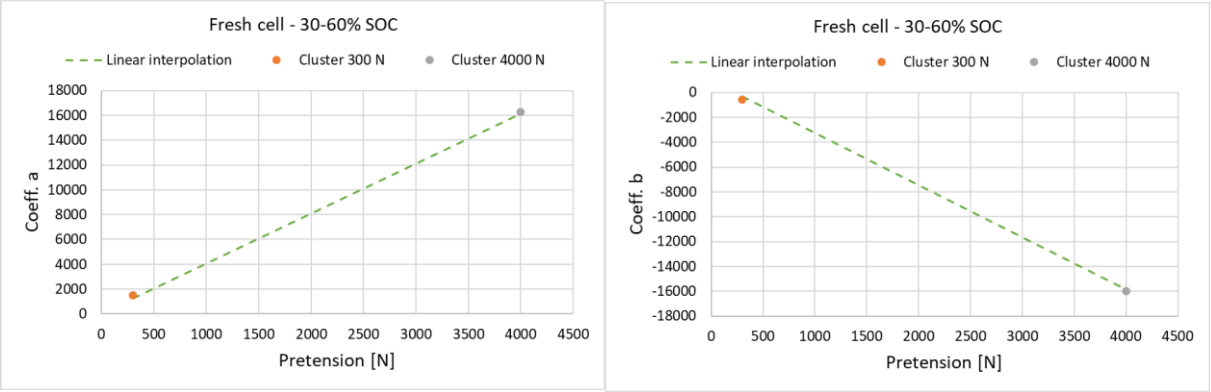

Figure 6-7 Value of coefficient a (left) and coefficient b (right) as a function of pretension. The weighted average of the clusters of points with the same conditions is connected by a straight line (dashed green line).

To obtain the slope and intercept values of the line linking the weighted average of the coefficients a and b at 300 N and 4000 N, the formula of the straight line passing through two points is used in which the term x refers to the pretension value, the term y to the value of the coefficient a:

$$\frac{x - x_0}{x_1 - x_0} = \frac{y - y_0}{y_1 - y_0}$$

Therefore:

$$y = \frac{y_1 - y_0}{x_1 - x_0} \cdot x + y_0 - x_0 \cdot \frac{y_1 - y_0}{x_1 - x_0} = \alpha \cdot x + \beta$$

From which we can obtain the equations to derive the slope and intercept of the line:

$$\alpha = \frac{y_1 - y_0}{x_1 - x_0}$$

$$\beta = y_0 - x_0 \cdot \frac{y_1 - y_0}{x_1 - x_0}$$

And replacing x and y:

$$\alpha = \frac{a(4000) - a(300)}{4000 - 300}$$

$$\beta = a(300) - 300 \cdot \frac{a(4000) - a(300)}{4000 - 300}$$

This process is repeated in such a way as to obtain alpha and beta for both fresh and aged cells taking into account the type of ageing. The coefficients alpha and beta obtained for the charging segment from 30% to 60% SOC are summarised in Table 6-1 for coefficient a and in Table 6-2 for coefficient b, the ageing procedure is shown in Table 3-4.

Table 6-1 Alpha and beta values as a function of ageing status for the parameter a when charging from 30% to 60% SOC.

	α	β
Fresh	0.2484	-12.9179
Ageing method 1	0.1723	119.6582
Ageing method 2	0.2046	5.5450

Table 6-2 Alpha and beta values as a function of ageing status for parameter b when charging from 30% to 60% SOC.

	α	β
Fresh	-0.2379	223.3939
Ageing method 1	-0.1104	271.6194
Ageing method 2	-0.1585	206.6494

Using the coefficients alpha and beta, the evolution of the coefficients a and b as a function of the pretension can be plotted through the formula:

$$P = \alpha \cdot a + \beta$$

Therefore:

$$a = \frac{P - \beta}{\alpha}$$

Similarly, for the other coefficient:

$$b = \frac{P - \beta}{\alpha}$$

With:

- a = slope
- b = intercept

Using the equations obtained, it is possible to derive the trend of parameters a and b as a function of pretension. The trends of the parameter a and b when charging from 30% to 60% SOC of the aged cell 5 with respect to the fresh cells 2 and 3 are shown in Figure 6-8, similarly, those of the aged cell 6 with respect to the fresh cells 2 and 3 are shown in Figure 6-9.

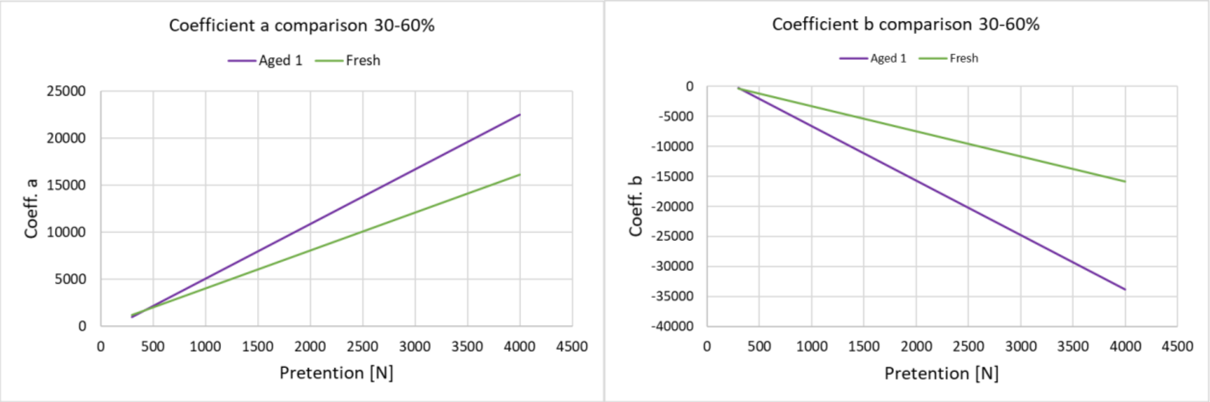

Figure 6-8 Parameters a (left) and b (right) when charging from 30% to 60% SOC as a function of applied pretension and ageing. The fresh cells considered are number 2 and 3, the aged cell is number 5.

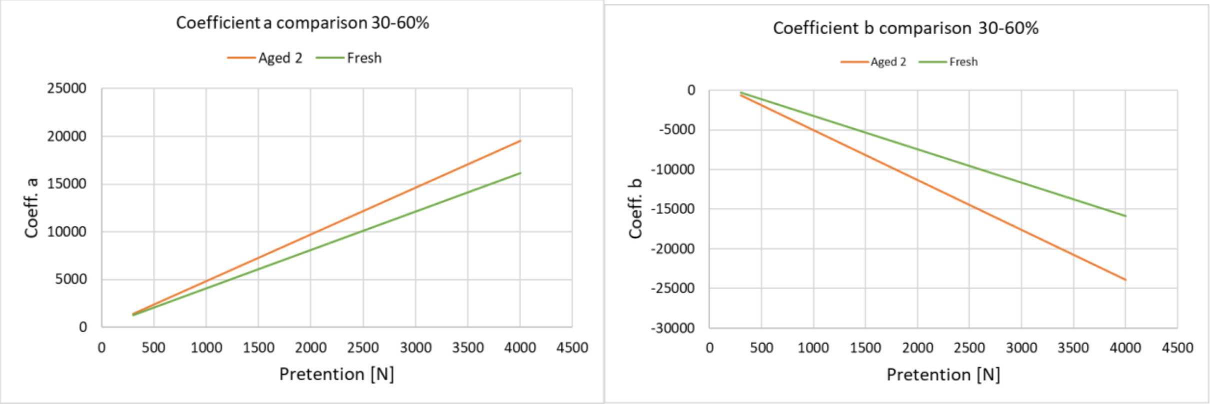

Figure 6-9 Parameters a (left) and b (right) when charging from 30% to 60% SOC as a function of applied pretension and ageing. The fresh cells considered are number 2 and 3, the aged cell is number 6.

For both ageing modes, there is a steeper slope and a lower intercept as the applied pretension increases than for fresh cells. It is also interesting to point out that the ageing process of cell number 5 has resulted in a greater loss of capacity than cell number 6, and the behaviour of cell number 5 is in between the fresh cells and the aged cell number 6.

The ageing process in the early stages follows a linear trend, as shown in Figure 6-10.

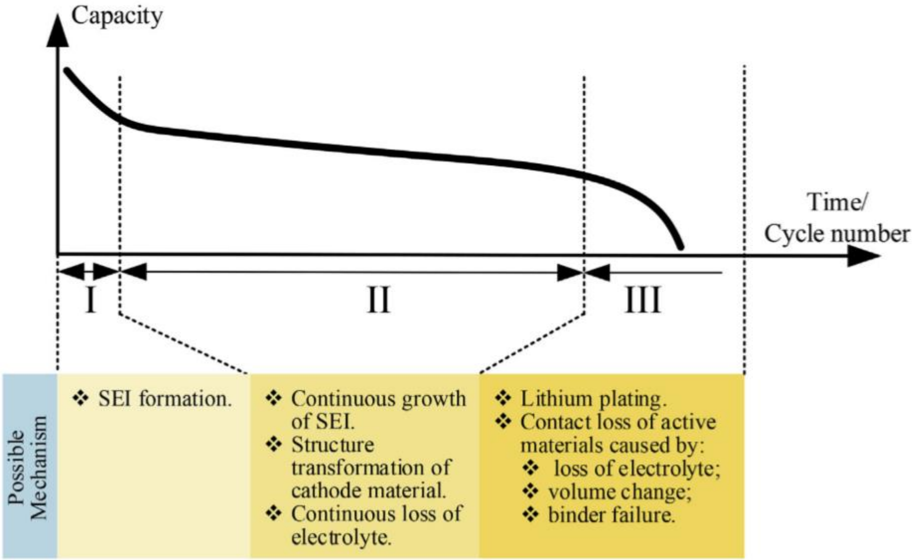

Figure 6-10 Capacity fade over the number of cycles of a cell (Han et al. 2019).

Therefore, the ageing process is considered linear and it is possible to obtain an approximate plane using the least square approximation function of the behaviour of parameters a and b as a function of both the pretension and the number of cycles to which the cell has been subjected according to the type of ageing. An example of the coefficient a as a function of pretension and number of cycles for the charging segment from 30% to 60% considering the ageing method 1 is shown in Figure 6-11.

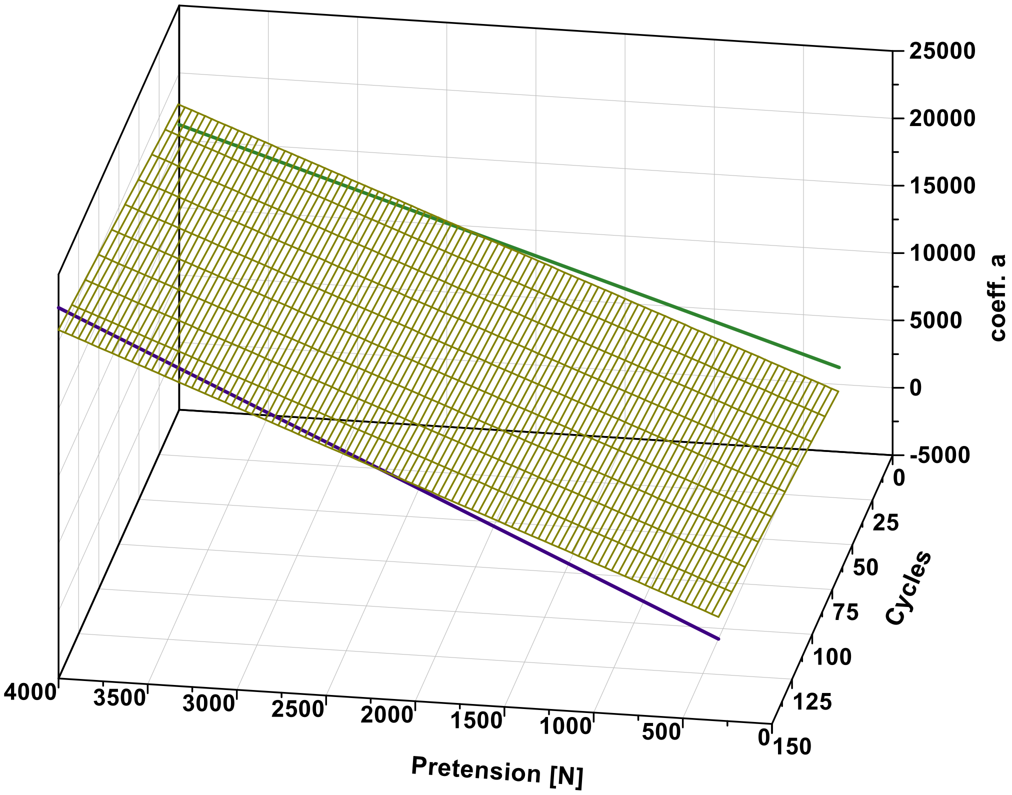

Figure 6-11 In the 3D plot, the purple and green lines represent the trend of the coefficient a with respect to pretension for the fresh cell and the aged cell (with ageing method 1) charged from 30% to 60% SOC, respectively. The olive green surface is the approximation plane of the two lines.

The equation of the plane allows the value of parameters a and b to be obtained as a function of pretension and number of cycles:

$$a = p_1 \cdot P + p_2 \cdot C + p_0$$
$$b = p_1 \cdot P + p_2 \cdot C + p_0$$

Using the values a and b, finally, the target equation can be derived:

$$\frac{F}{SOC} = a(P,C) \cdot SOC + b(P,C)$$

6.2 Results

The plane equations are obtained via a MATLAB script using the "lsqnonlin" command. The coefficients a and b are calculated by the following formula:

$$a = p_1 \cdot P + p_2 \cdot C + p_0$$
$$b = p_1 \cdot P + p_2 \cdot C + p_0$$

6.2.1 Charging

The values of p0, p1 and p2 are listed in the tables below, in particular, Table 6-3 refers to the calculation of coefficient a with ageing method 1, Table 6-4 to the calculation of coefficient b with ageing method 2, Table 6-5 to the calculation of coefficient a with ageing method 1 and Table 6-6 to the calculation of coefficient b with ageing method 2. In the tables below the term "precision" refers to the determination coefficient R^2.

Table 6-3 Coefficients b upon charging as a function of parameters p0, p1, and p2 for different SOCs, using ageing method 1. Precision shows how accurate the approximation is.

SOC [%]	p0	p1	p2	Precision
30-60	-1860.4956	4.9147	20.5231	0.9691
60-90	-1624.0507	2.9658	16.6279	0.9673
90-100	-265.7279	2.2541	0.8751	0.9945
90-100 CV	424.4087	2.1097	2.0479	0.9998

Table 6-4 Coefficients a upon charging as a function of parameters p0, p1, and p2 for different SOCs, using ageing method 1. Precision shows how accurate the approximation is.

SOC [%]	p0	p1	p2	Precision
30-60	6160.7252	-6.6328	-59.4733	0.8941
60-90	3432.1834	-2.3105	-26.6037	0.8888
90-100	1262.4245	-1.2249	-1.3291	0.9773
90-100 CV	433.2851	-1.0417	-2.2839	0.9991

Table 6-5 Coefficients b upon charging as a function of parameters p0, p1, and p2 for different SOCs, using ageing method 2. Precision shows how accurate the approximation is.

SOC [%]	p0	p1	p2	Precision
30-60	-873.9001	4.4559	5.9090	0.9909
60-90	-932.5482	2.6442	4.4384	0.9921
90-100	-97.4546	2.1758	-0.5170	0.9983
90-100 CV	405.3881	2.1186	2.0085	0.9997

Table 6-6 Coefficients a upon charging as a function of parameters p0, p1, and p2 for different SOCs, using ageing method 2. Precision shows how accurate the approximation is.

SOC [%]	p0	p1	p2	Precision
30-60	3202.4682	-5.2569	-13.8729	0.9631
60-90	2212.6894	-1.7433	-5.9190	0.9669
90-100	1059.9570	-1.1307	0.8268	0.9934
90-100 CV	458.1215	-1.0533	-1.9876	0.9984

From the results obtained, it is possible to note the decrease of the parameters characterising the coefficient a and b as the SOC increases (except during the constant voltage (CV) phase when the trend reverses), which translates into a reduction of the slope for higher states of charge. Furthermore, the contribution given by the pretension does not change much depending on the type of ageing, while the number of cycles has a greater influence, particularly for low SOC.

The coefficients a and b are used to calculate the following equation:

$$\frac{F}{SOC} = a(P, C) \cdot SOC + b(P, C)$$

With:

- F = global force [N]
- SOC = state of charge

- P = pretension [N]
- C = number of cycles

6.2.2 Discharging

As for the charging phase also for the discharging phase, the parameters p0, p1 and p2 are summarised in the tables below. In particular, Table 6-7 considers the case of coefficient a with ageing method 1, Table 6-8 coefficient b with ageing method 1, Table 6-9 coefficient a with ageing method 2 and finally Table 6-10 coefficient b with ageing method 1.

Table 6-7 Coefficients b upon discharging as a function of parameters p0, p1, and p2 for different SOCs, using ageing method 1. Precision shows how accurate the approximating plane is.

SOC [%]	p0	p1	p2	Precision
100-60	-26.3811	2.2023	-2.0697	0.9991
60-30	1455.0580	3.3714	-18.6775	0.9748

Table 6-8 Coefficients a upon discharging as a function of parameters p0, p1, and p2 for different SOCs, using ageing method 1. Precision shows how accurate the approximating plane is.

SOC [%]	p0	p1	p2	Precision
100-60	935.5248	-1.1655	1.9013	0.9950
60-30	-1978.9303	-3.1095	34.3612	0.9123

Table 6-9 Coefficients b upon discharging as a function of parameters p0, p1, and p2 for different SOCs, using ageing method 2. Precision shows how accurate the approximating plane is.

SOC [%]	p0	p1	p2	Precision
100-60	-114.5273	2.2433	0.0346	0.9999
60-30	906.6257	3.6265	-4.4089	0.9933

Table 6-10 Coefficients a upon discharging as a function of parameters p0, p1, and p2 for different SOCs, using ageing method 2. Precision shows how accurate the approximating plane is.

SOC [%]	p0	p1	p2	Precision
100-60	1042.9959	-1.2155	0.0485	0.9993
60-30	-1030.2379	-3.5507	9.2378	0.9721

The tables show, as in the case of charging, that as the SOC decreases, the parameters a and b decrease. The type of ageing has a marked influence on the number of cycles parameter and a negligible influence on the effect of the applied pretension.

The coefficients a and b are used to calculate the following equation:

$$\frac{F}{SOC} = a(P,C) \cdot SOC + b(P,C)$$

With:

- F = global force è [N]
- SOC = state of charge
- P = pretension [N]
- C = number of cycles

6.2.3 Relaxation

The parameters p0, p1 and p2 are summarised in Table 6-11 and Table 6-12 for obtaining, respectively a and b by ageing method 1 and in Table 6-13 and Table 6-14 for obtaining a and b by ageing method 2.

Table 6-11 Coefficients a during relaxation as a function of parameters p0, p1, and p2 for different SOCs, using ageing method 1. Precision shows how accurate the approximating plane is.

SOC [%]	**p0**	**p1**	**p2**	**Precision**
30 C	-629.8597	3.6116	15.3920	0.9720
60 C	3181.2413	1.9371	-8.4893	0.9569
90 C	1538.7354	1.2647	23.9903	0.9994
100 C	1084.4105	1.0977	-0.4236	0.9995
60 D	3711.5194	1.4999	-9.2730	0.9947
30 D	181.9182	2.0752	1.7303	0.9920

Table 6-12 Coefficients b during relaxation as a function of parameters p0, p1, and p2 for different SOCs, using ageing method 1. Precision shows how accurate the approximating plane is.

SOC [%]	**p0**	**p1**	**p2**	**Precision**
30 C	-4.80E-05	1.12E-08	-3.76E-08	0.9777
60 C	-1.33E-04	2.06E-08	3.66E-07	0.9082
90 C	-5.97E-05	1.67E-08	-4.02E-07	0.8277
100 C	-7.64E-06	1.06E-09	-2.56E-09	0.9949
60 D	-7.16E-05	1.24E-08	6.18E-08	0.9872
30 D	3.42E-05	-2.26E-09	-2.88E-07	0.7546

Table 6-13 Coefficients a during relaxation as a function of parameters p0, p1, and p2 for different SOCs, using ageing method 2. Precision shows how accurate the approximating plane is.

SOC [%]	p0	p1	p2	Precision
30 C	187.7810	3.2313	3.2004	0.9945
60 C	3908.2890	1.5990	2.9269	0.9976
90 C	1575.9529	1.2474	4.6182	0.9997
100 C	1093.4297	1.0935	-0.1034	0.9997
60 D	4204.8676	1.2704	3.6915	0.9357
30 D	66.3102	2.1290	0.1985	0.9961

Table 6-14 Coefficients b during relaxation as a function of parameters p0, p1, and p2 for different SOCs, using ageing method 2. Precision shows how accurate the approximating plane is.

SOC [%]	p0	p1	p2	Precision
30 C	-4.27E-05	8.71E-09	2.74E-08	0.9926
60 C	-1.52E-04	2.95E-08	1.61E-09	0.9991
90 C	-4.80E-05	1.13E-08	-8.97E-08	0.8685
100 C	-7.61E-06	1.05E-09	9.80E-10	0.9963
60 D	-8.00E-05	1.63E-08	-3.57E-08	0.9784
30 D	3.84E-05	-4.19E-09	-8.83E-08	0.7452

7 DISCUSSION

The tests with non-pretensioned and pretensioned cells carried out yield interesting comparisons of the mechanical behaviour of lithium-ion batteries under different conditions. Firstly, a comparison of cycles performed with non-pretensioned cells at different C-rates determined that faster charge cycles cause less deterministic cell behaviour and thus higher outcome variability. This behaviour is explained by the phenomenon that, for high C-rates, the movement of ions through the electrolyte is faster than their diffusion inside the anode. This mechanism causes an accumulation of ions in the outer part of the cathode leading to the occurrence of overshoot and a consequent more chaotic and less deterministic distribution of lithium-ions inside the anode (Sommer et al. 2015).

Another comparison is between the difference in the behaviour of aged versus fresh cells in the case of non-pretensioned cells. The results obtained, shown in Table 7-1, indicated a difference between fresh and aged cells in the case of experiments carried out with non-pretensioned cells, in general, the percentage thickness growth in fresh cells was higher and the homogeneity of the percentage increase more pronounced. The higher percentage increase in thickness caused by breathing in fresh cells is due to the fact that the amount of lithium ions in aged cells is lower than in fresh cells. A difference in behaviour as a function of the ageing method, as analysed in Chapter 4.2.4.1, also emerged.

Table 7-1 Average thickness increase from 0 to 100% for fresh and aged cells.

Cell type	**C-rate**	**Average thickness increase from 0 to 100%**			
		Minimum	Maximum	Average	Max. – Min.
Fresh	0.5	2.69%	3.07%	2.96%	0.39%
	1	2.55%	3.05%	2.89%	0.51%
Ageing method 1	0.5	2.41%	2.80%	2.51%	0.39%
	1	2.37%	3.21%	2.59%	0.84%
Ageing method 2	0.5	2.11%	2.73%	2.28%	0.61%
	1	1.99%	2.53%	2.16%	0.54%

In the case of pretensioned cells, as shown in Table 7-2, it is possible to compare the behaviour of cells subjected to low pretension (300 N) and high pretension (4000 N).

Table 7-2 Average pressure behaviour for different types of cells at different SOC. In the last column, the percentage value of the peak compared to the average is calculated.

Cell type	Pretension	Pressure [MPa]			Perc. Difference
		Avg. 100% SOC	Peak 100% SOC	Avg. increase 0-100% SOC	Peak/Max – 1
Fresh	300 N	0.0463	0.3480	0.0435	663%
	4000 N	0.1925	0.5767	0.1006	200%
Ageing method 1	300 N	0.0420	0.3183	0.0402	659%
	4000 N	0.1903	0.5840	0.0973	207%
Ageing method 2	300 N	0.0440	0.4079	0.0419	829%
	4000 N	0.1915	0.6824	0.0966	256%

Cells subjected to higher pretension showed higher pressures and greater absolute pressure growth during charging, but the percentage difference between the maximum and average value was smaller, suggesting a more homogeneous pressure distribution. The higher absolute pressure growth is due to the non-linearity of the elastic mechanical behaviour of the pouch cell. As shown by the stress-strain curve in Figure 7-1, as the stack pressure increases, the stress required to perform the same deformation also increases (Cannarella and Arnold 2014).

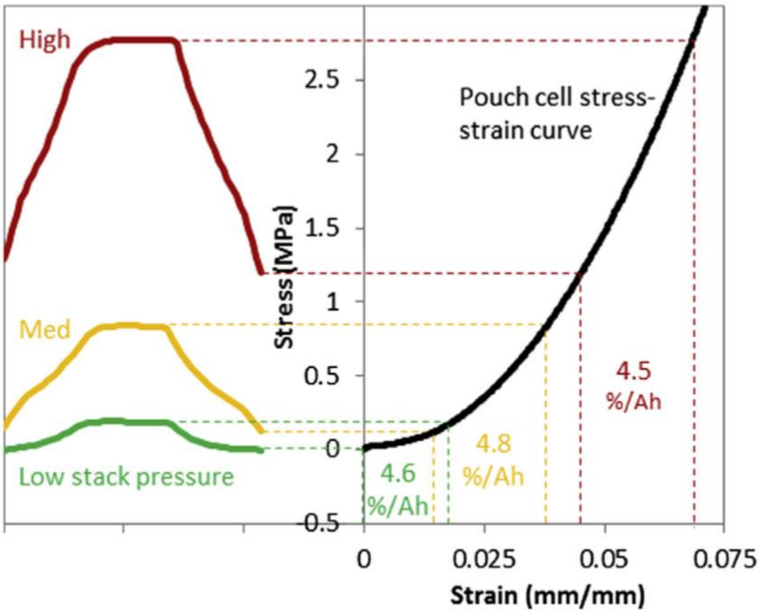

Figure 7-1 Comparison of stress curves over an entire charge and discharge cycle under different applied pretensions with the pouch cell stress-strain curve (Cannarella and Arnold 2014).

The empirical model provides simple mathematical tools to study the force trend as a function of some of the key parameters such as SOC, number of cycles and pretension applied at 30% SOC. However, this type of analysis is not suitable for SOCs that tend towards zero and is only a first approximation for the development of a simulation model, and its accuracy can be improved by studying the behaviour of the cell with different types of ageing and different pretensions.

All experiments were carried out at room temperature (20±2 °C). In real-life applications, the temperature can differ and play a key role in cell expansion. In order to obtain more exhaustive results, it would be advisable to extend the research by also considering the effect of the temperature.

7.1 Thickness relaxation

For the evaluation of the thickness in non-pretensioned cells, a period of relaxation is necessary at the end of each charging and discharging phase. In fact, the thickness tends to decrease in the minutes following the end of the charging/discharging phase. Experimental experience has set the waiting time after each phase at 900 seconds when the C-rate is 1 and 600 seconds when the C-rate is 0.5. The difference in thickness is depicted in the graph in Figure 7-2, in which the thickness at the centre of the cell is measured during an entire cycle. The blue lines represent the charge (or discharge) phase, the red lines the relaxation period, the unmeasured period between relaxation and the next charge/discharge is due to the time (approx. 7 minutes) taken to perform the surface measurement. So, if the measurement of the entire surface is taken immediately after charging (or discharging) the cell, there may be imbalances between the first measured point and the last measured point. The cause of this phenomenon is due to the presence of thermal effects and the diffusion of ions within the cathode to more stable positions at the end of the charge or discharge phase, both effects are amplified by higher C rates. (Rieger et al. 2016; Sommer et al. 2015). The impact of the thickness relaxation period is particularly marked for 60% SOC and 90% SOC, almost 10% of the total swelling, less important for 30% SOC, less than 3%, and essentially irrelevant for 100% SOC.

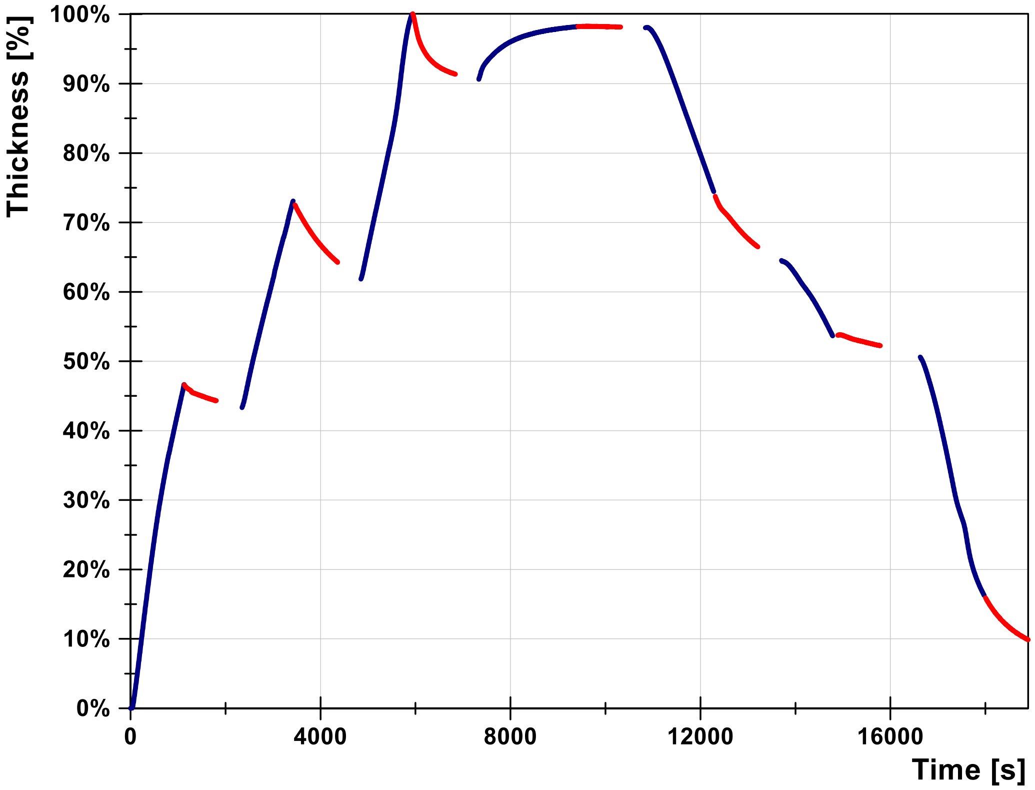

Figure 7-2 Percentage thickness in the centre of the cell during an entire cycle with 1 C, the blue lines are the charging/discharging phases, the red lines the relaxation periods.

7.2 Cell geometry

The pressure distribution was initially measured with a different layout, shown in Figure 7-3, than that shown in Figure 5-1.

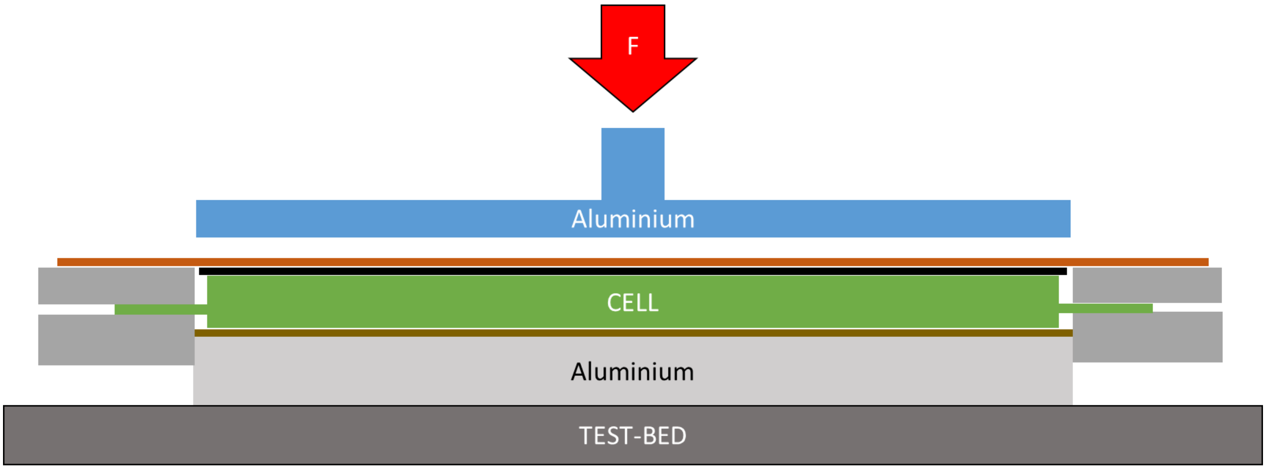

Figure 7-3 Schematic view of the first testbed setup. For the layers without a label: the brown layer is Pertinax, the black layer is the compression pad and the orange layer is the pressure pad.

The pressure distribution with the first setup is shown in Figure 7-4 and Figure 7-5 applying 300 N and 4000 N of pretension, respectively. The figures highlight that most of the force is transferred along the edges of the cell, which limits the analysis of the pressure distribution in the centre. For this reason, the setup illustrated in Chapter 5.1 is used, in which two compression pads smaller than the cell are applied on both sides of the cell; this strategy allows the effect of the presence of the bumps (see Chapter 3.2) to be neglected.

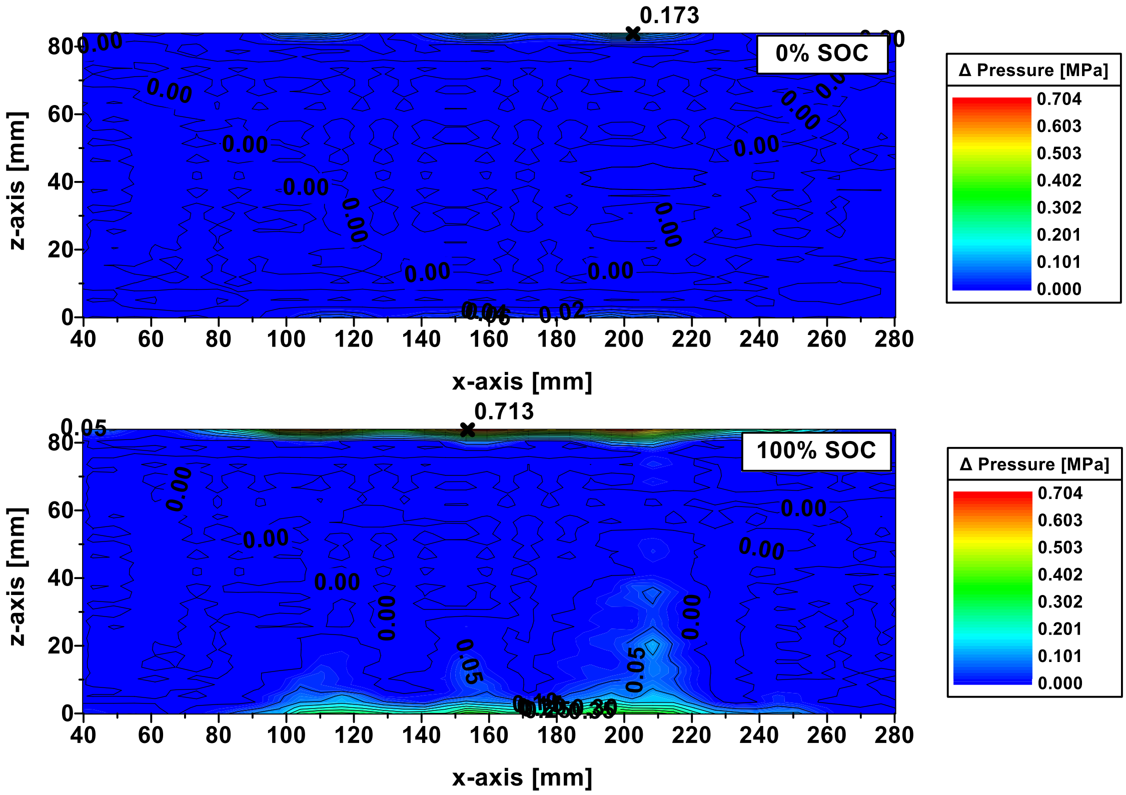

Figure 7-4 Pressure distribution at 0% SOC (top) and at 100% SOC (bottom) applying a pretension of 300 N at 30% SOC.

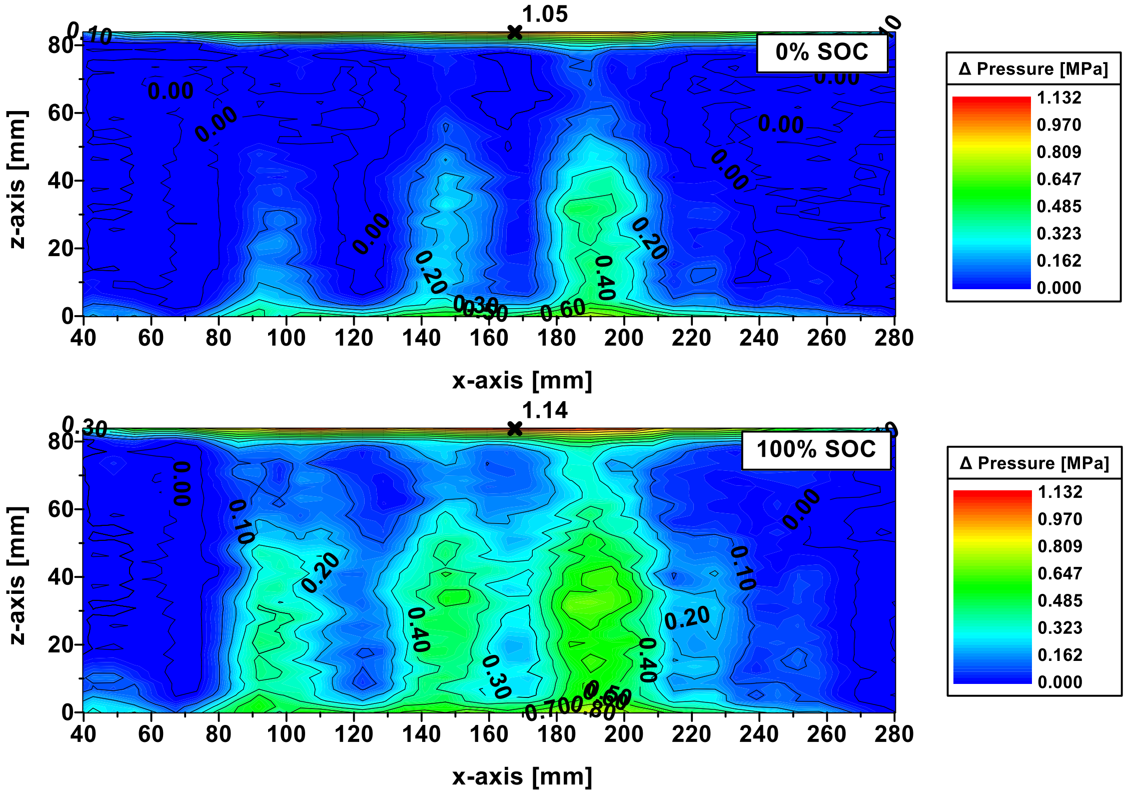

Figure 7-5 Pressure distribution at 0% SOC (top) and at 100% SOC (bottom) applying a pretension of 4000 N at 30% SOC.

With the final setup, the analysed area is reduced to a 60x200 mm surface, as shown in Figure 7-6.

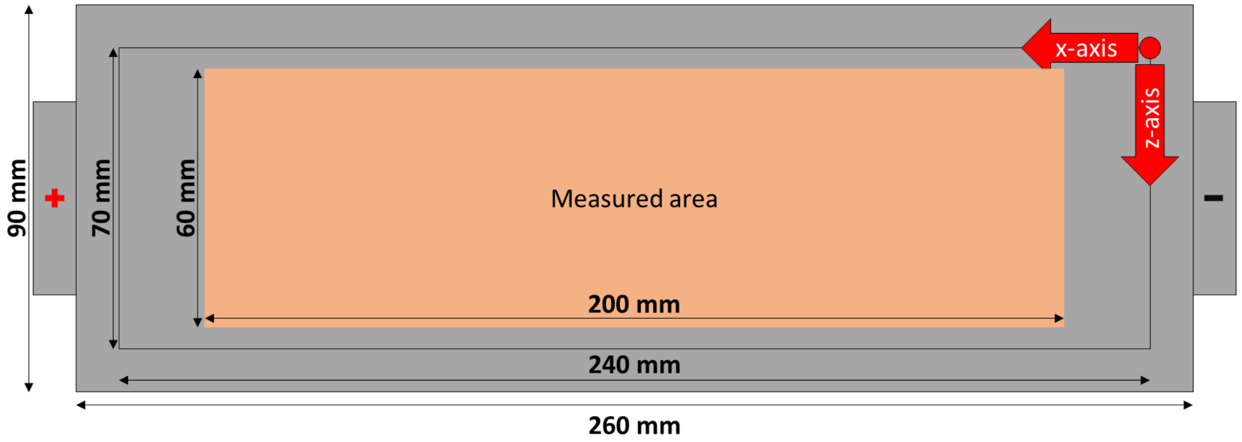

Figure 7-6 Area considered for the pressure distribution.

7.3 Force relaxation

In the case of experiments with pretensioned cells, a waiting time of 30 minutes is required after the application of the pretension because, as shown in the graph in Figure 7-7, in the following 10 minutes there is a change in the global force applied to the system for that z value. Considering the case of pretensioning with 4000 N the force settles to a stable value after about 30 minutes, while in the case of 300 N of pretension the force's settlement takes less time, about 5 minutes. The change in global force is approximately 5%. The force relaxation is related to the viscoelastic behaviour of the cell under the compression force (Zhu et al. 2018).

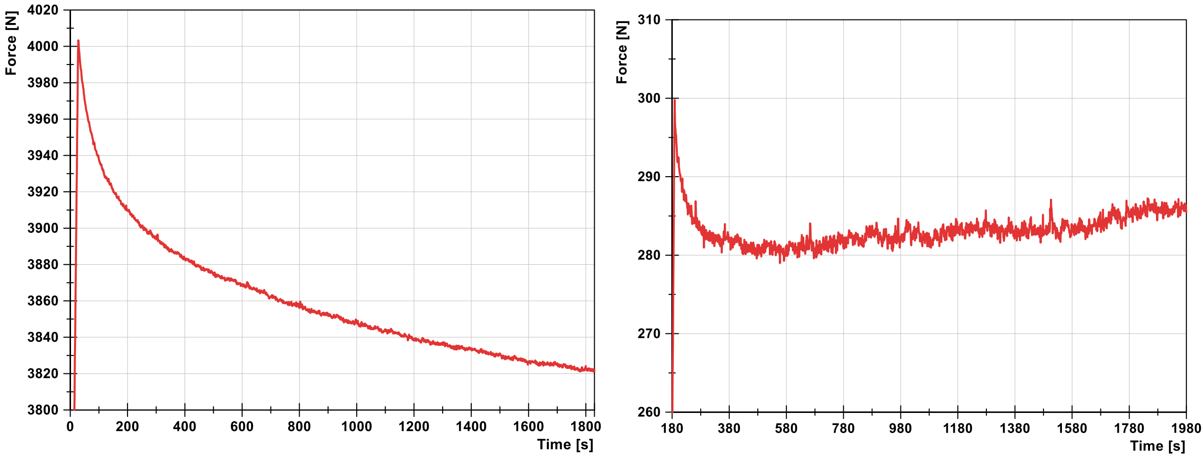

Figure 7-7 Force change during the waiting time after applying 4000 N (right) and 300 N (left) pretension.

8 CONCLUSIONS

The effect of swelling and breathing was studied in the case of both non-pretensioned and pretensioned cells. The results obtained made it possible to answer the initial research questions.

The used measurement systems to quantify the mechanical effects of breathing have been found to be effective. Capacitive sensors for measuring the increase in thickness in non-pretensioned cells enabled precise values (accuracy of ±0.012 µm compared to an average thickness increase of 365 µm) to be obtained quickly. Whereas, for the measurement of pressure in pretensioned cells, the use of the pressure mat gave decent results, however, to improve the accuracy of the results it would be advisable to use a load cell with greater precision.

The analysis of both pretensioned and non-pretensioned cells showed that the main factor influencing breathing is the SOC. For high SOC the tendency to expand volumetrically is higher, from 0 to 100% the average thickness increase was 2.92% with fresh cells and 2.39% with aged cells while the global force increased from 0% to 100% SOC by an average of 1121 N under 300 N of pretension and 2622 N at 4000 N pretension. Another parameter to be considered is the location on the cell: experiments have shown that breathing does not occur homogeneously over the whole cell, but that there are areas which are more affected by volumetric expansion in the case of non-pretensioned cells or by higher pressures in the case of pretensioned cells, specifically in the case of non-pretensioned fresh cells the increase in volume was mainly in the centre of the cell and the average difference between the maximum and minimum percentage increase was 0.45%, whereas for aged cells the increase in thickness occurred predominantly along the edges and in the centre of the cell with an average difference between the maximum and minimum percentage of 0.59%. Similarly, the pressure in the case of the pretensioned cells had the highest peaks in the centre of the cell (considering the fact that the edges of the cell were not analysed) and the recorded peaks averaged 0.356 MPa for the cell 300 N pretensioned cells and 0.605 MPa for the 4000 N pretensioned cells, and generally higher pretensions resulted in more homogeneous pressure distributions, the average percentage difference between the peak and the average pressure value of a fully charged cell pretensioned with 300 N is 717% and when pretensioned with 4000 N is 212%. The distribution, as shown by the data above, of the breathing magnitude is influenced by another parameter of interest, which is the ageing of the cell. The ageing of the cell not only affected the pressure distribution but also caused a distributed decrease in cell breathing due to the lower number of ions compared to fresh cells. In addition, experiments with non-pretensioned cells also showed the influence of the C-rate during the charging phase; with high C-rates, overshooting occurs as soon as the cell enters the charging phase at constant voltage. Overshooting is a temporary increase in thickness, which peaks at around 90% SOC and then tends to fade when a full charge is reached. Overshoot, on the other hand, is not present during cell discharge. The applied pretension also affects the evolution of the global applied force due to breathing, for lower pretension forces the percentage increase in global force is higher than for higher pretension forces (1866% and 107%), however, when considering the absolute increase on average, the cells loaded with 4000 N had an increase in the global force of 2622N while the cells loaded with 300 N experienced an increase in the global force of 1121N.

The empirical model developed, by discretising the force curve above the SOC, makes it possible to approximate the global force trend during charging and discharging with respect to the state of charge, the pretension applied at 30% charge and the number of cycles following a precise cell ageing method. Similarly, relaxation is also studied through the empirical model by considering time, pretension and number of cycles as variables.

In order to optimise the life of the batteries, it would be advisable to size the module housing the cells according to the pressure distribution of the cell stack and its evolution over time, thereby applying a compressive force that is not too high and homogeneous throughout the cycle of use of the battery.

The results obtained determined the main factors influencing the volumetric displacement of the cell. By means of the empirical model, it was possible to obtain equations that can be used for the development of a simulation model. The modelling of the cell will allow the prediction of the stresses acting as a function of the main parameters and thus the realisation of a module capable of limiting undesirable stresses and optimising the behaviour of the battery.

9 REFERENCES

AUDI AG (2015): Audi e-tron quattro concept. Bild-Nr: A1511323. Available online at https://www.audi-mediacenter.com/de/fotos/detail/audi-e-tron-quattro-concept-27589, checked on 3/26/2021.

B&R (2019): Data sheet X20AI1744-10.

Bach, Tobias C.; Schuster, Simon F.; Fleder, Elena; Müller, Jana; Brand, Martin J.; Lorrmann, Henning et al. (2016): Nonlinear aging of cylindrical lithium-ion cells linked to heterogeneous compression. In *Journal of Energy Storage* 5, pp. 212–223. DOI: 10.1016/j.est.2016.01.003.

Bilgin, Berker; Magne, Pierre; Malysz, Pawel; Yang, Yinye; Pantelic, Vera; Preindl, Matthias et al. (2015): Making the Case for Electrified Transportation. In *IEEE Trans. Transp. Electrific.* 1 (1), pp. 4–17. DOI: 10.1109/TTE.2015.2437338.

Cannarella, John; Arnold, Craig B. (2014): Stress evolution and capacity fade in constrained lithium-ion pouch cells. In *Journal of Power Sources* 245, pp. 745–751. DOI: 10.1016/j.jpowsour.2013.06.165.

Cano, Zachary P.; Banham, Dustin; Ye, Siyu; Hintennach, Andreas; Lu, Jun; Fowler, Michael; Chen, Zhongwei (2018): Batteries and fuel cells for emerging electric vehicle markets. In *Nat Energy* 3 (4), pp. 279–289. DOI: 10.1038/s41560-018-0108-1.

Dambrowski, Jonny (2013): Methoden der Ladezustandsbestimmung und ihre Eignung für LiFePO4-Li4Ti5O12-Zellen Teil 1. In *Elektronik* 7/2013.

El Kharbachi, A.; Zavorotynska, O.; Latroche, M.; Cuevas, F.; Yartys, V.; Fichtner, M. (2020): Exploits, advances and challenges benefiting beyond Li-ion battery technologies. In *Journal of Alloys and Compounds* 817, p. 153261. DOI: 10.1016/j.jallcom.2019.153261.

Elektro-Automatic (2019a): EL 9000 B Electronic DC Load. Operating Manual.

Elektro-Automatic (2019b): PSI 9000 WR 3U. Operating Guide.

Few, Sheridan; Schmidt, Oliver; Offer, Gregory J.; Brandon, Nigel; Nelson, Jenny; Gambhir, Ajay (2018): Prospective improvements in cost and cycle life of off-grid lithium-ion battery packs: An analysis informed by expert elicitations. In *Energy Policy* 114 (21), pp. 578–590. DOI: 10.1016/j.enpol.2017.12.033.

Greenwood, David (2018): Automotive Batteries 101. Lecture notes. University of Warwick.

Han, Xuebing; Lu, Languang; Zheng, Yuejiu; Feng, Xuning; Li, Zhe; Li, Jianqiu; Ouyang, Minggao (2019): A review on the key issues of the lithium ion battery degradation among the whole life cycle. In *eTransportation* 1 (1–2), p. 100005. DOI: 10.1016/j.etran.2019.100005.

Heymans, Catherine; Walker, Sean B.; Young, Steven B.; Fowler, Michael (2014): Economic analysis of second use electric vehicle batteries for residential energy storage and load-levelling. In *Energy Policy* 71 (10), pp. 22–30. DOI: 10.1016/j.enpol.2014.04.016.

IEA (2020): Global EV Outlook 2020. In *IEA, Paris*. Available online at https://www.iea.org/reports/global-ev-outlook-2020, checked on 3/26/2021.

Kochhan, Robert; Fuchs, Stephan; Reuter, Benjamin; Burda, Peter; Matz, Stephan; Lienkamp, Markus (2014): An Overview of Costs for Vehicle Components, Fuels and Greenhouse Gas Emissions.

Korthauer, Reiner; Wuest, Michael (2018): Lithium-ion batteries. Basics and applications / Reiner Korthauer, editor ; translator Michael Wuest, alphabet & more. Berlin, Germany: Springer.

Lee, Jae Hyun; Lee, Hyang Mok; Ahn, Soonho (2003): Battery dimensional changes occurring during charge/discharge cycles—thin rectangular lithium ion and polymer cells. In *Journal of Power Sources* 119-121, pp. 833–837. DOI: 10.1016/S0378-7753(03)00281-7.

Lighting Global (2019): Lithium-ion Batteries Part I: General Overview and 2019 Update. Technical Notes Issue 30.

Mars, N.; Krouz, F.; Louar, F.; Sbita, L. (2017): Comparison study of different dynamic battery model. 23-25 March, 2017, Hammamet, Tunisia. Piscataway, NJ: IEEE. Available online at http://ieeexplore.ieee.org/servlet/opac?punumber=8058138.

Megatron (2020): Datasheet KMB38.

Micro-Epsilon (2020): capaNCDT - Capacitive displacement sensors and systems.

Müller, Verena; Scurtu, Rares-George; Memm, Michaela; Danzer, Michael A.; Wohlfahrt-Mehrens, Margret (2019): Study of the influence of mechanical pressure on the performance and aging of Lithium-ion battery cells. In *Journal of Power Sources* 440, p. 227148. DOI: 10.1016/j.jpowsour.2019.227148.

Neubauer, Jeremy; Pesaran, Ahmad (2011): The ability of battery second use strategies to impact plug-in electric vehicle prices and serve utility energy storage applications. In *Journal of Power Sources* 196 (23), pp. 10351–10358. DOI: 10.1016/j.jpowsour.2011.06.053.

Oh, Ki-Yong; Siegel, Jason B.; Secondo, Lynn; Kim, Sun Ung; Samad, Nassim A.; Qin, Jiawei et al. (2014): Rate dependence of swelling in lithium-ion cells. In *Journal of Power Sources* 267, pp. 197–202. DOI: 10.1016/j.jpowsour.2014.05.039.

Rieger, Bernhard; Erhard, Simon V.; Rumpf, Katharina; Jossen, Andreas (2016): A New Method to Model the Thickness Change of a Commercial Pouch Cell during Discharge. In *J. Electrochem. Soc.* 163 (8), A1566-A1575. DOI: 10.1149/2.0441608jes.

Sarlioglu, Bulent; Morris, Casey T.; Di Han; Li, Silong (2017): Driving Toward Accessibility: A Review of Technological Improvements for Electric Machines, Power Electronics, and Batteries for Electric and Hybrid Vehicles. In *IEEE Ind. Appl. Mag.* 23 (1), pp. 14–25. DOI: 10.1109/MIAS.2016.2600739.

Sauerteig, Daniel; Ivanov, Svetlozar; Reinshagen, Holger; Bund, Andreas (2017): Reversible and irreversible dilation of lithium-ion battery electrodes investigated by in-situ dilatometry. In *Journal of Power Sources* 342, pp. 939–946. DOI: 10.1016/j.jpowsour.2016.12.121.

SLAC National Laboratory, Stanford University (2015): Study Finds a Way to Prevent Fires in Next-Generation Lithium Batteries. Available online at https://www6.slac.stanford.edu/news/2015-06-17-study-finds-way-prevent-fires-next-generation-lithium-batteries.aspx, checked on 3/26/2021.

Sommer, Lars Wilko; Kiesel, Peter; Ganguli, Anurag; Lochbaum, Alexander; Saha, Bhaskar; Schwartz, Julian et al. (2015): Fast and slow ion diffusion processes in lithium ion pouch cells during cycling observed with fiber optic strain sensors. In *Journal of Power Sources* 296 (3), pp. 46–52. DOI: 10.1016/j.jpowsour.2015.07.025.

Spingler, Franz B.; Wittmann, Wilhelm; Sturm, Johannes; Rieger, Bernhard; Jossen, Andreas (2018): Optimum fast charging of lithium-ion pouch cells based on local volume expansion criteria. In *Journal of Power Sources* 393, pp. 152–160. DOI: 10.1016/j.jpowsour.2018.04.095.

Sun, Peiyi; Bisschop, Roeland; Niu, Huichang; Huang, Xinyan (2020): A Review of Battery Fires in Electric Vehicles. In *Fire Technol* 56 (4), pp. 1361–1410. DOI: 10.1007/s10694-019-00944-3.

Tekscan (2015): Pressure mapping sensor 5511 - datasheet.

Tekscan (2020): i-Scan selection guide.

Wang, Xianming; Sone, Yoshitsugu; Kuwajima, Saburo (2004): In Situ Investigation of the Volume Change in Li-ion Cell with Charging and Discharging. In *J. Electrochem. Soc.* 151 (2), A273. DOI: 10.1149/1.1635827.

Wentker, Marc; Greenwood, Matthew; Leker, Jens (2019): A Bottom-Up Approach to Lithium-Ion Battery Cost Modeling with a Focus on Cathode Active Materials. In *Energies* 12 (3), p. 504. DOI: 10.3390/en12030504.

Wu, Yuping (2015): Lithium-ion batteries. Fundamentals and applications. 1st. Boca Raton: CRC Press (Electrochemical energy storage and conversion).

Xiong, Rui; Shen, Weixiang (2018): Advanced Battery Management Technologies for Electric Vehicles. 1st: John Wiley & Sons (Automotive Series).

Xu, Bolun; Oudalov, Alexandre; Ulbig, Andreas; Andersson, Goran; Kirschen, Daniel S. (2018): Modeling of Lithium-Ion Battery Degradation for Cell Life Assessment. In *IEEE Trans. Smart Grid* 9 (2), pp. 1131–1140. DOI: 10.1109/TSG.2016.2578950.

Zhang, Jianan; Zhang, Lei; Sun, Fengchun; Wang, Zhenpo (2018): An Overview on Thermal Safety Issues of Lithium-ion Batteries for Electric Vehicle Application. In *IEEE Access* 6, pp. 23848–23863. DOI: 10.1109/ACCESS.2018.2824838.

Zhao, Wei; Luo, Gang; Wang, Chao-Yang (2015): Modeling Internal Shorting Process in Large-Format Li-Ion Cells. In *J. Electrochem. Soc.* 162 (7), A1352-A1364. DOI: 10.1149/2.1031507jes.

Zhu, Juner; Wierzbicki, Tomasz; Li, Wei (2018): A review of safety-focused mechanical modeling of commercial lithium-ion batteries. In *Journal of Power Sources* 378 (Part 2), pp. 153–168. DOI: 10.1016/j.jpowsour.2017.12.034.

A APPENDIX

A.1 Instrumentation

A.1.1 Capacitive sensors

High-precision capacitive sensors with a diameter of 20 mm, shown in Figure Appendix A.1-1, were used for distance measurement of non-pretensioned cells. These sensors provide measurements with an accuracy of ±0.012 µm through a stable signal with high immunity to interference and thermal fluctuations. Besides, the measurement is non-contact, which speeds up the measurement process and simplifies automation, as it prevents the occurrence of vibrations and localized deformations.

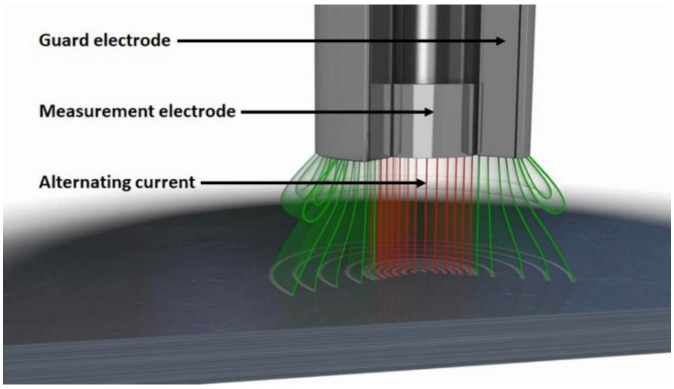

Figure Appendix A.1-1 Microepsilon capacitive sensor.

Table Appendix A.1-1 Specifications of capacitive sensor Micro-Epsilon CSE3.

Manufacturer	Micro-Epsilon
Sensor model	CSE3
Description	Cylindrical sensor with socket, compact design
Measuring range	3 mm
Temperature range	From -50°C to +200 °C
Dimensions	Ø 20 x 24 mm
Min. target size	Ø 20 mm
Material	1.4404 (non-magn.)
Connection	Socket (type B)

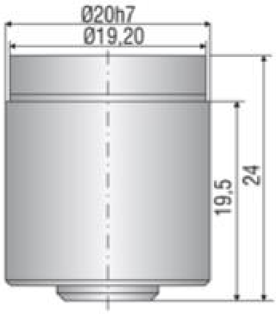

Figure Appendix A.1-2 Capacitive sensor CSE3 (Micro-Epsilon 2020).

Table Appendix A.1-2 Specification of controller Micro-Epsilon DT6222/DL6222 /ECL2.

Manufacturer	Micro-Epsilon
Controller model	DT6222/DL6222 /ECL2
Description	High-precision multi-channel controller for dynamic measurement tasks / extended cable lengths
System resolution with sensor CSE3:	0.012 µm
Frequency response:	20 kHz
Output:	Voltage output, Current output, Ethernet interface

Figure Appendix A.1-3 Controller DT6222/DL6222 /ECL2 (Micro-Epsilon 2020).

A.1.2 Testbed

A.1.2.1 Non-pretensioned configuration

The testbed, shown in Figure Appendix A.1-4, is used to clamp the battery and allows movement along the three axes. The battery is attached to a special structure, shown in Figure Appendix A.1-5, capable of moving along the x and y axes, the capacitive sensors are attached to a mechanical arm capable of moving along the z-axis. The reference system is illustrated in Figure Appendix A.1-6.

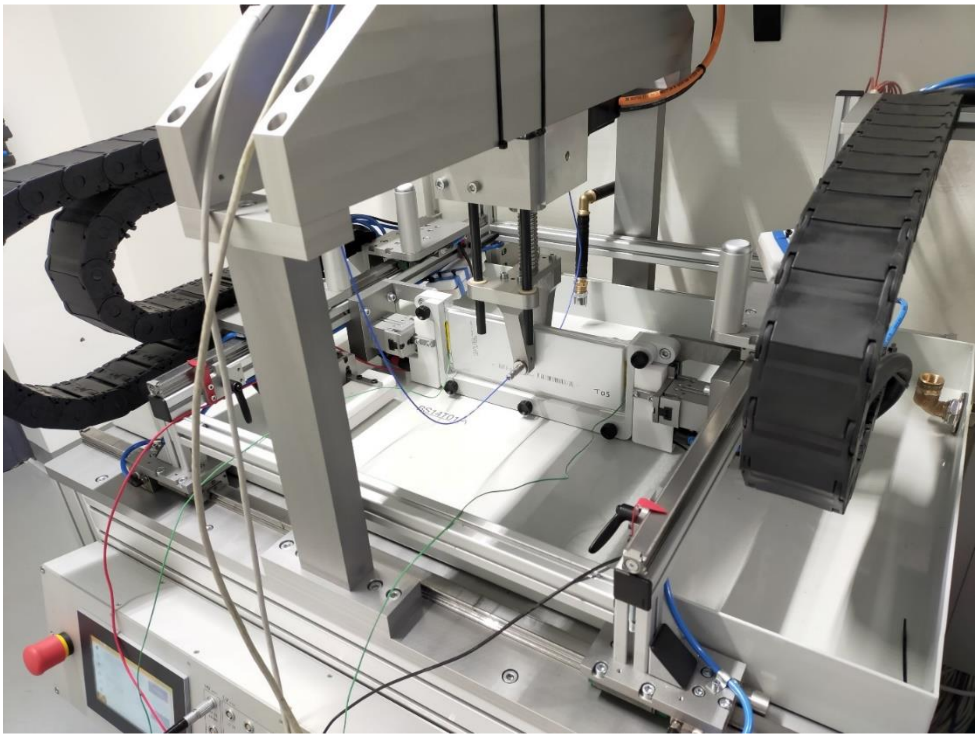

Figure Appendix A.1-4 Testbed during the experiments with the sensors mounted at the end of the electronic arm measuring the centre of the cell.

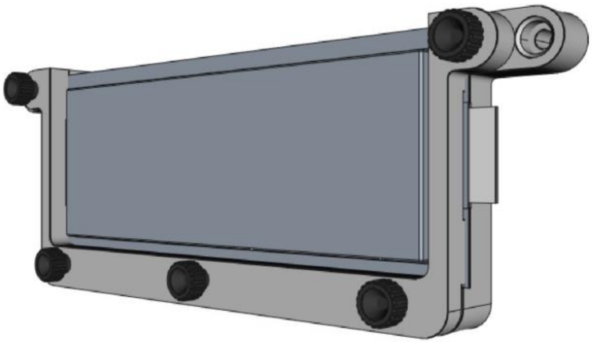

Figure Appendix A.1-5 CAD of the cell fixing structure.

Figure Appendix A.1-6 Degrees of freedom of the sensors with respect to the cell.

A.1.2.2 Pretensioned configuration

For the pretensioned series of experiments the orientation of the clamping system has changed, the new configuration of the testbed is shown in Figure Appendix A.1-7. In this configuration the cell is parallel to the testbed and is pressed through an aluminium plate, the applied force is controlled through the load cell system of Appendix 9A.1.5.

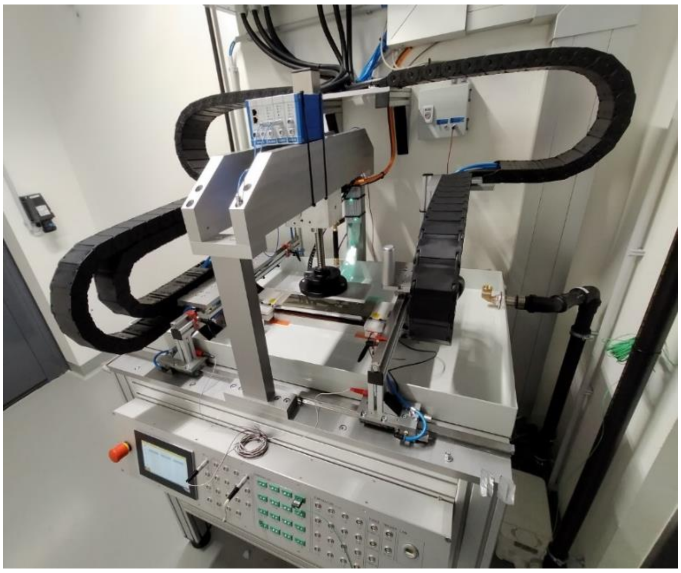

Figure Appendix A.1-7 Testbed with parallel clamping.

A.1.3 Cyclic station

The cycling station, pictured in Figure Appendix A.1-8, includes a DC power supply, a DC electronic load and a controller.

Figure Appendix A.1-8 Cycling station with power supply, electronic load and controller.

The employed power supply (PS) is EA-PSI 9080-340 by Elektro-Automatik used to deliver a maximum current of 60A, while the employed electronic load (EL) is EA-EL 9080-340 B by Elektro-Automatik, used to absorb a maximum current of 60 A. More specifications are given in Appendix 9A.1.3.1 and 9A.1.3.2. The PS and the EL are controlled by an internal python programmed software, in which the test protocol can be defined, able to measure and log detailed information of the battery behaviour during charging and discharging.

A.1.3.1 Power supply

Table Appendix A.1-3 Specifications of power supply Elektro-Automatik EA-PSI 9080-340.

Manufacturer	Elektro-Automatik
Model	EA-PSI 9080-340
Product type	DC Laboratory power supply
Housing	19'' rack
Max voltage	80 V
Output voltage accuracy	< 0.1%
Max current	340 A
Output current accuracy	< 0.02%
Max power	10 kW
Output power accuracy	< 1%
Slew rate 10%-90%	< 30 ms
Operation temperature	0-50°C

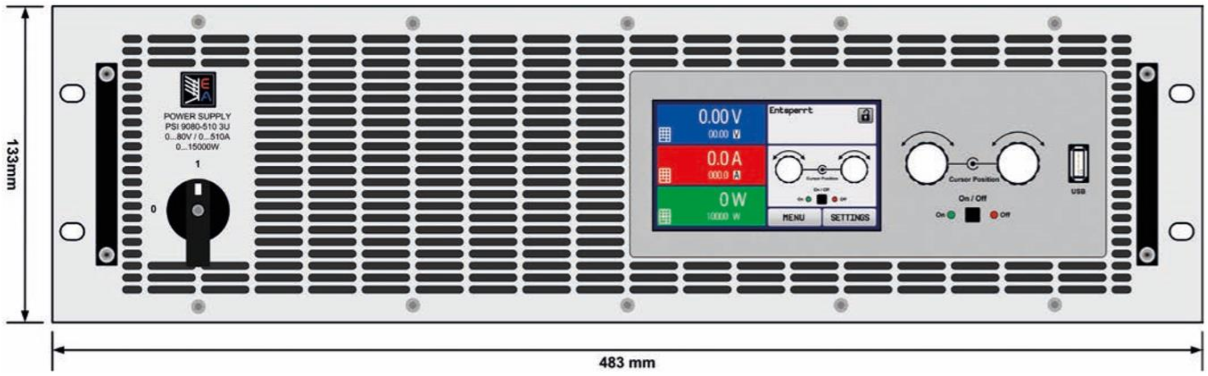

Figure Appendix A.1-9 Power supply front view (Elektro-Automatic 2019b).

A.1.3.2 Electronic load

Table Appendix A.1-4 Specifications of electronic load Elektro-Automatik EA-EL 9080-340 B.

Manufacturer	Elektro-Automatik
Model	EA-EL 9080-340 B
Product type	DC electronic load
Housing	19’’ rack
Max voltage	80 V
Input voltage accuracy	< 0.1%
Max current	340 A
Input current accuracy	< 0.2%
Max power	4800 W
Input power accuracy	< 0.5%
Resistance	0.03-7.5 Ω
Resistance accuracy	≤ 1% + 0.3% of nominal current
Operation temperature	0-50°C

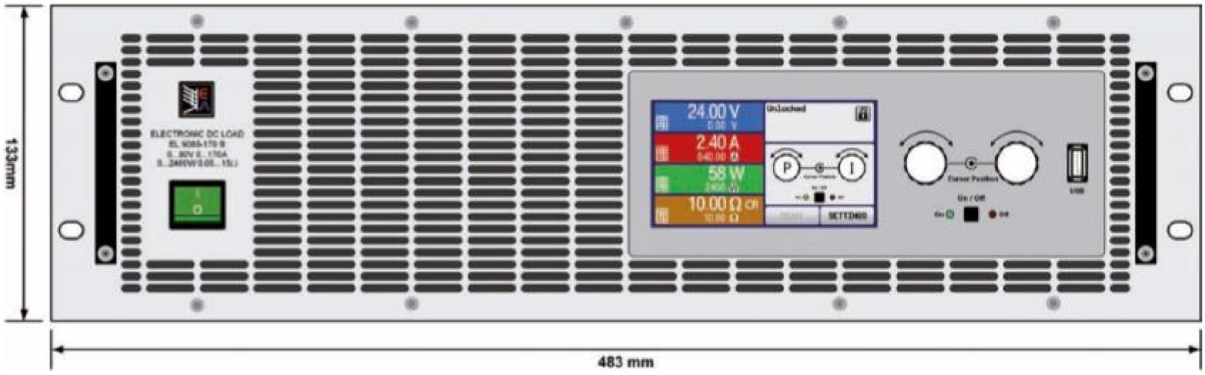

Figure Appendix A.1-10 Electronic load front view (Elektro-Automatic 2019a).

A.1.4 Pressure distribution data acquisition system

The system configuration utilised to acquire pressure distribution data, as shown in Figure Appendix A.1-11, is composed of 4 basic components:

- the pressure mapping sensor
- the VersaTek handle
- the VersaTek hub
- the computer on which to run the acquisition software

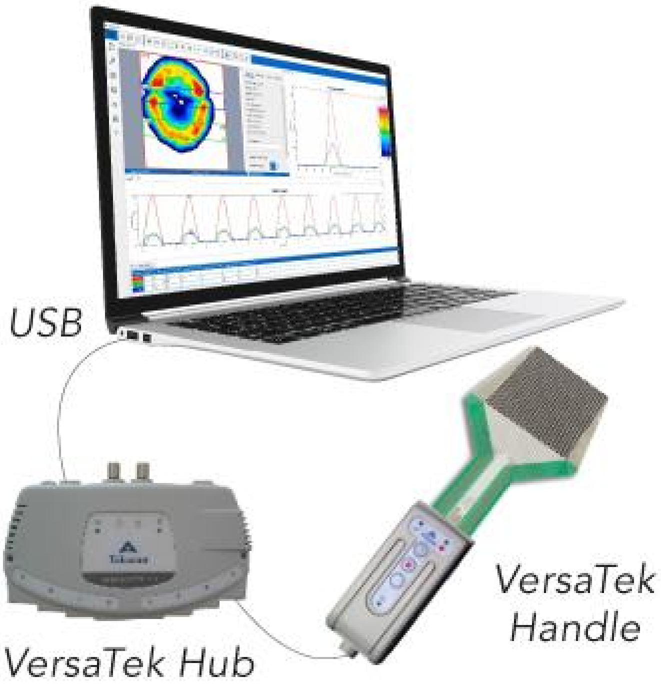

Figure Appendix A.1-11 Pressure distribution data acquisition configuration (Tekscan 2020).

The grid-based sensor, shown in Figure Appendix A.1-12, consists of two thin, flexible polyester sheets placed on top of each other (sensor thickness is less than 0.1 mm). Each sheet has printed strips of conductive material, in one sheet the stripes are horizontal, while in the other the stripes are vertical, this arrangement allows to obtain a grid. A semi-conductive ink is printed on top of the conductors. Each intersection in the array will be a measurement point. Whenever a force is applied to the sensing elements, the internal resistance of the semiconductor materials changes inversely proportional to the acting pressure, allowing to distinguish the pressure distribution on the surface.

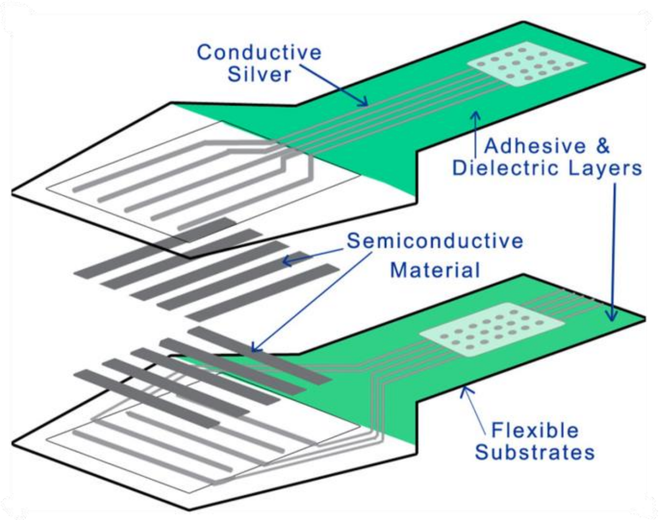

Figure Appendix A.1-12 Matrix-based pressure mapping sensor (Tekscan 2020).

Specifications on the sensor used can be found in Appendix 9A.1.4.1.

The sensor is connected to a handle that communicates via a LAN cable with the hub. The hub is responsible for driving, managing and collecting incoming data from the handle and forwarding the information to the computer through a USB 2.0 cable. More details about the handle and hub system are provided in Appendix 9A.1.4.2. Then, the data received by the computer is handled by the software "I-scan". The software is able to show the pressure distribution in real-time and also to record, save and export it in ASCII text file (.csv) so that the collected data can be processed by external data analysis programs.

A.1.4.1 Pressure mapping sensor

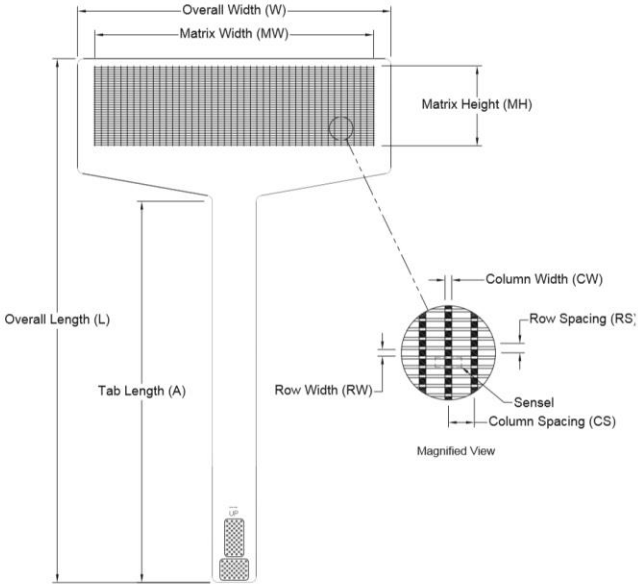

Figure Appendix A.1-13 Pressure mapping sensor 5511 dimensions (Tekscan 2015).

Table Appendix A.1-5 Pressure mapping sensor specifications.

Manufacturer	Tekscan
Model	Pressure mapping sensor 5511
Overall length (L)	565.2 mm
Overall width (W)	337.8 mm
Tab length (A)	411.2 mm
Matrix width (MV)	307.3 mm
Matrix height (MH)	86.4 mm
Thickness	0.305 mm
Column width (CW)	1.8 mm
Column pitch (CS)	7.0 mm
Number of columns	44
Row width (CW)	1.8 mm
Row pitch (CS)	2.5 mm
Number of rows	34
Total number of sensing points (sensels)	1496
Sensel spatial density	5.6 sensel per cm^2
Pitch	2540 mm
Temperature range (low)	-40 °C
Temperature range (high)	60 °C

A.1.4.2 Data acquisition electronics

The data acquisition electronics referred to as VersaTek, is composed of the VersaTek handle and the VersaTek Hub.

Table Appendix A.1-6 VersaTek configuration specifications.

Handle housing material	Polycarbonate/ABS blend (grey)
Hub housing material	Polyurethane [PUR] (Grey)
Handle weight	305 g
Hub weight	370 g
Power source	Input 100-240V 5A 50-60 Hz, Output: 12V, 5A
Standard cable length	Handle to Hub: 4.57 m Hub to Host: 3 m
Maximum cable length	Handle to Hub: 30 m Hub to Host: 5 m
Maximum scanning speed	Up to 20 MHz (speeds vary by sensors)
Handles supported by the hub	8
Pulse-per-frame synchronization	Yes
Digital pressure resolution	8 bit
Communication to PC	USB 2.0, 480 Mbps
Temperature range (low)	-10 °C
Temperature range (high)	55 °C
Humidity range (low)	0%
Humidity range (high)	90% (non condensing)

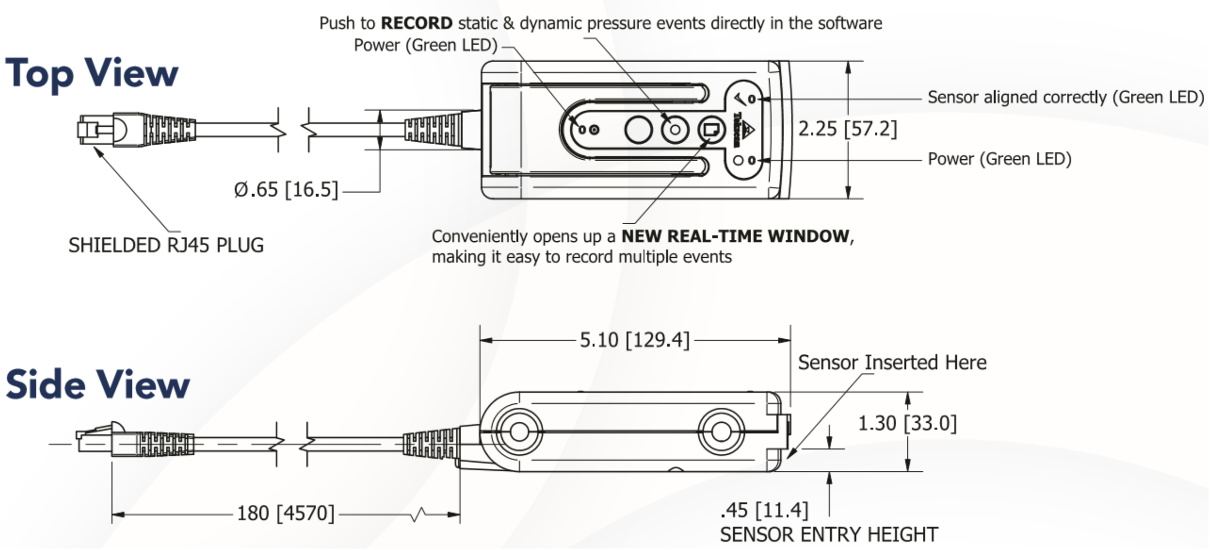

Figure Appendix A.1-14 VersaTek Handle dimensions in mm (Tekscan 2020).

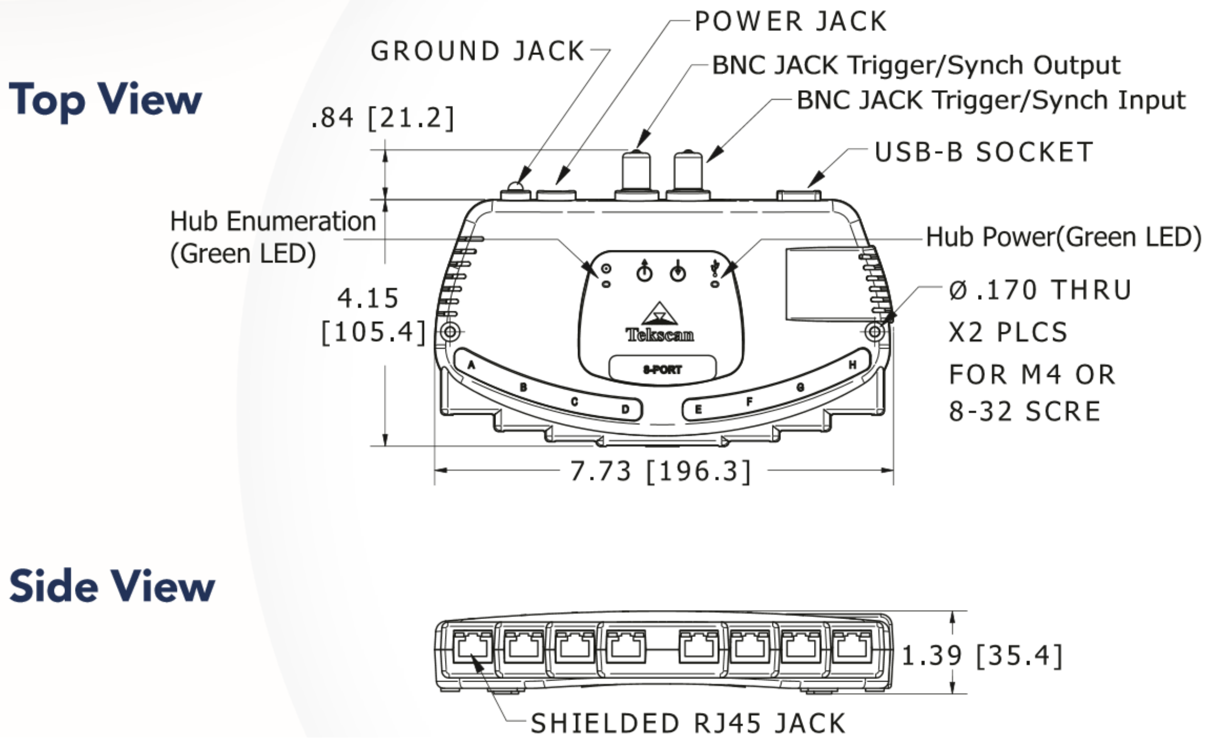

Figure Appendix A.1-15 VersaTek hub dimensions in mm (Tekscan 2020).

A.1.5 Load cell and load cell module

A.1.5.1 Load cell

The load cell is positioned on top of the aluminium plate, as shown in Figure Appendix A.1-16, and makes it possible to quantify the global force applied to the cell both at the beginning of the cycle during the application of pretension and during the entire cycle.

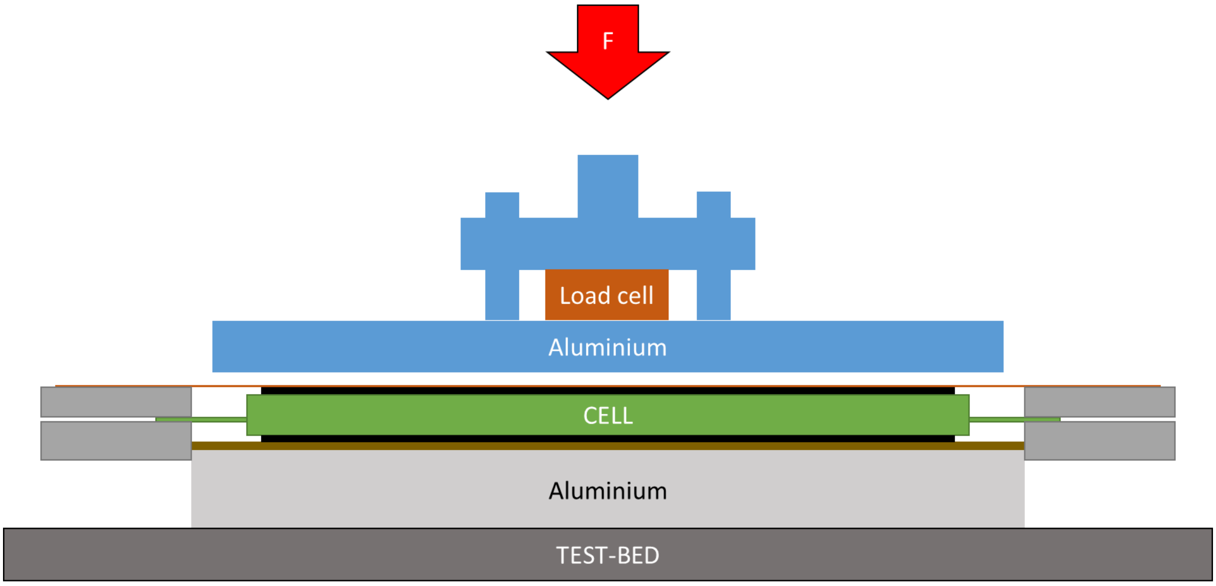

Figure Appendix A.1-16 Layout of the test setup with the load cell.

Due to the configuration, the weight of the aluminium plate which applies a certain force on the cell is not taken into account by the load cell. Nevertheless, the approximate weight of the aluminium plate is:

$$m = \rho \cdot V = 2.7 \cdot (1 \cdot 10 \cdot 28.5) = 769.5\ g$$

$$1000\ g = 1\ kg \rightarrow 769.5\ g = 0.7695\ kg$$

$$F_g = m \cdot g = 0.7695 \cdot 9.81 = 7.55\ N$$

With:

- m = mass
- ρ = density
- V = volume
- F_g = weight force
- g = gravity

The weight force exerted by the aluminium plate is approximately 7.5 N and therefore within the load cell's tolerance limits:

$$\varepsilon = 0.5\% \cdot (rated\ output) = 0.005 \cdot 20000 = \pm 100\ N$$

Table Appendix A.1-7 Load cell specifications.

Manufacturer	Megatron
Model	Series KMB38
Type	Button load cell
Rated force	20 kN
Relative linearity error	≤ 0.5% of rated force
Input and output resistance	700±10 Ω
Maximum operating force	≤ 150% of rated force
Rated range of excitation voltage	10 VDC / AC
Operating range of excitation voltage	≤ 20 VDC / AC
Rated temperature range (low)	-50 °C
Rated temperature range (high)	90 °C
Operating temperature range (low)	0 °C
Operating temperature range (high)	70 °C
Protection	IP64
Temperature effect on characteristic value	≤ 0.36% of rated output / 10 K
Temperature effect on zero signal	≤ 0.18% of rated output / 10 K
Creep under load	≤ 0.5% of rated output
Cable dimension	4 x AWG26. cable shielded
Cable length from body	ca. 3 m
Body material	Stainless steel (17-4 PH)
Mass	ca. 90 g

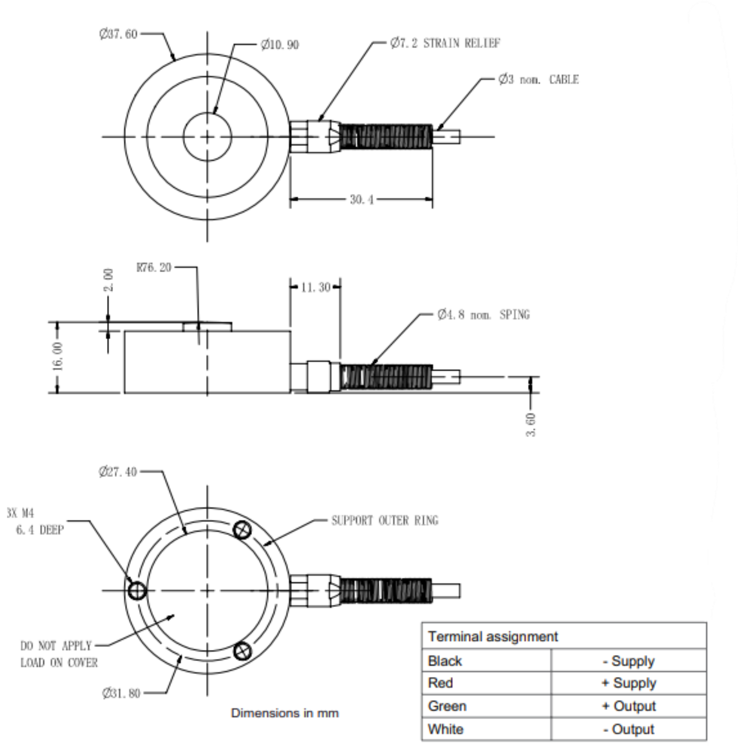

Terminal assignment	
Black	- Supply
Red	+ Supply
Green	+ Output
White	- Output

Figure Appendix A.1-17 Load cell bottom, side and top view and dimensions (Megatron 2020).

A.1.5.2 Load cell module

The voltage output for 0 kN and 20 kN has been measured and is shown in Table Appendix A.1-8, the voltage window is the following:

$$0\ mV \leq V \leq 1.881mV$$

While the force window is:

$$0\ kN \leq F \leq 20\ kN$$

Considering that the steps for the 32-bit load cell module are of 2.5 nV, the force steps are:

$$F_{step} = F_{tot} \cdot \frac{V_{step}}{V_{tot}} = 20 \times 10^3 \cdot \frac{2.5 \times 10^{-9}}{1.881 \times 10^{-3}} = 0.027\ N$$

Therefore, the uncertainty given by the load cell module is negligible compared to the tolerance of the load cell and the tolerance range of the system can be approximated to ±100N.

Table Appendix A.1-8 Load cell module specifications.

Manufacturer	B&R
Model	X20AI1744-10
Type	1 full-bridge strain gauge input
Voltage level	0kN force: 0.00000 mV 20kN force: 18.0964 mV
Digital converter resolution	24-bit
Quantization of LSB with 2 mV/V	2.50 nV
Protection	IP20

Figure Appendix A.1-18 3D view of the load cell module (B&R 2019).

A.2 Regression functions summary

In the tables the coefficients a and b refer to the following regression functions:

$$Linear: y = a \cdot x + b$$

$$Exponential: y = a \cdot e^{b \cdot x}$$

Table Appendix A.2-1 Linear regression during charging phases of fresh cells.

Cell	Pretension [N]	Cycle	SOC [%]	Precision	b	a
2	300	1	30-60	0.937	1525.482	-548.003
		1	60-90	0.998	497.229	971.470
		1	90-100	0.911	979.595	382.929
		1	90-100 CV	0.041	1379.057	-38.440
		2	30-60	0.720	961.213	-197.121
		2	60-90	0.999	118.153	1056.421
		2	90-100	0.949	477.575	608.556
		2	90-100 CV	0.178	963.515	94.366
	4000	1	30-60	0.969	16286.183	-16001.604
		1	60-90	0.989	9371.464	-4312.358
		1	90-100	0.997	8617.140	-3470.326
		1	90-100 CV	0.996	8937.322	-3801.623
		2	30-60	0.968	16059.702	-15736.121
		2	60-90	0.988	9273.125	-4253.719
		2	90-100	0.999	8649.864	-3545.247
		2	90-100 CV	0.997	8805.381	-3702.684
3	300	1	30-60	0.719	1105.098	-149.112
		1	60-90	0.998	216.694	1142.237
		1	90-100	0.977	632.971	624.761
		1	90-100 CV	0.144	1147.624	82.156
		2	30-60	0.876	1347.082	-325.012
		2	60-90	0.997	370.132	1111.532
		2	90-100	0.969	802.672	571.934
		2	90-100 CV	0.031	1405.032	-57.258
	4000	1	30-60	0.969	16339.715	-16148.984
		1	60-90	0.987	9175.935	-4062.108
		1	90-100	0.998	8329.577	-3128.811

Cell	Pretension [N]	Cycle	SOC [%]	Precision	b	a
		1	90-100 CV	0.993	8755.481	-3570.314
		2	30-60	0.969	15925.384	-15623.741
		2	60-90	0.988	8997.686	-3937.191
		2	90-100	0.999	8166.184	-3022.212
		2	90-100 CV	0.995	8750.088	-3633.334

Table Appendix A.2-2 Linear regression during charging phases of aged cells.

Cell	Pretension [N]	Cycle	SOC [%]	Precision	b	a
5	300	1	30-60	0.914	1048.536	-289.395
		1	60-90	0.974	682.487	445.086
		1	90-100	0.999	225.805	1007.446
		1	90-100 CV	0.323	1241.949	-130.876
		2	30-60	0.179	1037.632	-92.471
		2	60-90	0.990	767.115	389.516
		2	90-100	0.998	237.872	1074.897
		2	90-100 CV	0.500	1359.408	-187.576
	4000	1	30-60	0.977	24535.695	-37117.633
		1	60-90	0.988	14953.528	-12668.012
		1	90-100	0.990	9988.234	-4739.965
		1	90-100 CV	0.998	9864.901	-4507.751
		2	30-60	0.978	20511.762	-30455.557
		2	60-90	0.987	12582.567	-10269.844
		2	90-100	0.990	8395.742	-3624.596
		2	90-100 CV	0.997	8577.527	-3757.035
6	300	1	30-60	0.985	1360.067	-514.655
		1	60-90	0.995	711.902	532.767
		1	90-100	0.989	179.197	1159.422
		1	90-100 CV	0.757	1497.341	-332.300
		2	30-60	0.989	1517.336	-663.064
		2	60-90	0.998	792.969	533.779
		2	90-100	0.968	292.106	1120.427
		2	90-100 CV	0.813	1649.198	-417.248
	4000	1	30-60	0.971	20531.064	-25382.429

Cell	Pretension [N]	Cycle	SOC [%]	Precision	b	a
		1	60-90	0.989	11980.471	-7645.359
		1	90-100	1.000	9007.019	-3634.012
		1	90-100 CV	0.998	9917.605	-4649.650
		2	30-60	0.970	18505.642	-22484.956
		2	60-90	0.989	10850.586	-6665.841
		2	90-100	1.000	8224.556	-3138.549
		2	90-100 CV	0.997	9181.589	-4208.324

Table Appendix A.2-3 Linear regression during discharging phases of fresh cells.

Cell	Pretension [N]	Cycle	SOC [%]	Precision	b	a
2	300	1	100-60	0.994	689.938	665.337
		1	60-30	0.958	1715.367	-1227.319
		2	100-60	0.997	241.118	833.299
		2	60-30	0.925	1152.226	-829.038
	4000	1	100-60	0.981	8999.449	-3976.695
		1	60-30	0.969	16215.025	-16792.949
		2	100-60	0.983	9013.650	-4013.723
		2	60-30	0.968	16171.601	-16752.311
3	300	1	100-60	0.996	466.945	767.852
		1	60-30	0.951	1304.768	-771.329
		2	100-60	0.994	659.245	691.585
		2	60-30	0.955	1575.614	-995.794
	4000	1	100-60	0.982	8872.780	-3810.752
		1	60-30	0.970	15859.871	-16088.257
		2	100-60	0.982	8725.935	-3720.060
		2	60-30	0.970	15623.981	-15852.129

Table Appendix A.2-4 Linear regression during discharging phases of aged cells.

Cell	Pretension [N]	Cycle	SOC [%]	Precision	b	a
5	300	1	0.988	405.682	723.789	0.988
		1	0.946	641.983	313.482	0.946
		2	0.985	482.539	710.851	0.985

Cell	Pretension [N]	Cycle	SOC [%]	Precision	b	a
		2	0.950	741.231	262.475	0.950
	4000	1	0.997	8925.082	-3590.680	0.997
		1	0.990	11865.298	-7867.074	0.990
		2	0.997	7778.980	-2984.580	0.997
		2	0.990	10358.804	-6748.914	0.990
6	300	1	0.973	555.604	655.016	0.973
		1	0.971	1139.500	-374.036	0.971
		2	0.966	671.231	608.075	0.966
		2	0.965	1314.691	-551.077	0.965
	4000	1	0.992	9160.717	-3936.395	0.992
		1	0.985	14056.586	-11805.396	0.985
		2	0.993	8488.671	-3550.196	0.993
		2	0.985	13013.383	-10841.840	0.985

Table Appendix A.2-5 Exponential regression during relaxation after charging and discharging phases of fresh cells with 300 N and 4000 N pretension.

Cell	Pretension [N]	Cycle	SOC [%]	Precision	a	b
2	300	1	30 C	0.928	1824.383	-3.52E-05
		1	60 C	0.921	1300.820	-4.47E-05
		1	90 C	0.814	12588.449	-4.50E-06
		1	100 C	0.968	12430.966	-4.48E-06
		1	60 D	0.906	1576.898	-4.84E-05
		1	30 D	0.931	1708.162	-3.79E-05
		2	30 C	0.977	13004.265	-8.65E-06
		2	60 C	0.980	12627.956	-7.74E-06
		2	90 C	0.991	4471.357	-1.28E-04
		2	100 C	0.986	4080.087	-1.53E-04
		2	60 D	0.991	10160.694	-3.53E-05
		2	30 D	0.991	9827.059	-3.30E-05
	4000	1	30 C	0.991	4779.117	-1.48E-04
		1	60 C	0.988	4806.884	-1.38E-04
		1	90 C	0.991	10344.997	-3.75E-05
		1	100 C	0.989	10297.160	-3.84E-05

Cell	Pretension [N]	Cycle	SOC [%]	Precision	a	b
		1	60 D	0.987	2028.734	-3.02E-05
		1	30 D	0.980	1851.396	-4.19E-05
		2	30 C	0.989	6530.880	-1.24E-05
		2	60 C	0.985	6264.350	-9.88E-06
		2	90 C	0.987	1986.773	-3.53E-05
		2	100 C	0.988	2089.053	-3.24E-05
		2	60 D	0.989	6696.409	-1.39E-05
		2	30 D	0.983	6613.442	-1.39E-05
3	300	1	30 C	0.867	1453.799	-5.25E-06
		1	60 C	0.015	1063.697	-7.63E-07
		1	90 C	0.962	5411.265	-3.10E-06
		1	100 C	0.953	5316.194	-2.39E-06
		1	60 D	0.933	1396.555	-8.08E-06
		1	30 D	0.931	1527.443	-8.16E-06
		2	30 C	0.936	5585.193	-4.88E-06
		2	60 C	0.977	5417.952	-3.75E-06
		2	90 C	0.990	3699.042	-6.16E-05
		2	100 C	0.984	2911.718	-6.88E-05
		2	60 D	0.995	9468.837	-1.66E-05
		2	30 D	0.987	9640.488	-1.76E-05
	4000	1	30 C	0.994	4450.765	-7.76E-05
		1	60 C	0.994	4740.003	-7.42E-05
		1	90 C	0.997	10259.045	-2.10E-05
		1	100 C	0.996	10305.944	-2.19E-05
		1	60 D	0.955	590.366	3.83E-05
		1	30 D	0.041	859.311	4.80E-06
		2	30 C	0.966	8763.181	1.38E-05
		2	60 C	0.977	8954.432	1.27E-05
		2	90 C	0.958	298.161	5.68E-05
		2	100 C	0.915	471.367	4.50E-05
		2	60 D	0.962	8882.691	1.20E-05
		2	30 D	0.950	8710.419	1.21E-05

Table Appendix A.2-6 Exponential regression during relaxation after charging and discharging phases of aged cells with 300 N and 4000 N pretension.

Cell	Pretension [N]	Cycle	SOC [%]	Precision	a	b
5	300	1	30 C	0.877	1869.046	-7.26E-05
		1	60 C	0.869	1353.896	-3.42E-05
		1	90 C	0.896	18597.865	-5.18E-06
		1	100 C	0.916	15982.503	-6.32E-06
		1	60 D	0.917	1605.843	-3.14E-05
		1	30 D	0.919	1736.166	-2.94E-05
		2	30 C	0.312	15245.076	-1.00E-06
		2	60 C	0.347	13865.460	-1.11E-06
		2	90 C	0.900	1683.629	-5.82E-05
		2	100 C	0.882	1750.265	-5.62E-05
		2	60 D	0.911	11069.709	-1.07E-05
		2	30 D	0.913	9789.857	-1.13E-05
	4000	1	30 C	0.971	5106.588	-1.48E-04
		1	60 C	0.972	5131.907	-1.41E-04
		1	90 C	0.972	11369.557	-3.05E-05
		1	100 C	0.966	11288.356	-3.41E-05
		1	60 D	0.988	5320.286	-1.35E-04
		1	30 D	0.983	5571.512	-1.35E-04
		2	30 C	0.991	10328.079	-3.12E-05
		2	60 C	0.992	10206.237	-3.55E-05
		2	90 C	0.990	3366.712	-8.54E-05
		2	100 C	0.970	3224.927	-7.70E-05
		2	60 D	0.973	8131.551	-1.97E-05
		2	30 D	0.974	7848.584	-2.04E-05
6	300	1	30 C	0.904	1279.304	-8.20E-06
		1	60 C	0.894	1334.370	-7.48E-06
		1	90 C	0.970	5681.036	-3.16E-06
		1	100 C	0.984	5232.591	-4.08E-06
		1	60 D	0.878	1309.366	-6.87E-06
		1	30 D	0.925	1397.802	-7.36E-06

Cell	Pretension [N]	Cycle	SOC [%]	Precision	a	b
		2	30 C	0.972	5639.856	-3.18E-06
		2	60 C	0.967	5303.726	-2.80E-06
		2	90 C	0.911	2943.902	-5.69E-05
		2	100 C	0.913	3013.763	-5.49E-05
		2	60 D	0.889	8386.835	-1.49E-05
		2	30 D	0.888	7836.631	-1.58E-05
	4000	1	30 C	0.986	5547.316	-8.62E-05
		1	60 C	0.984	7106.771	-9.46E-05
		1	90 C	0.984	9842.084	-2.02E-05
		1	100 C	0.985	9680.430	-2.15E-05
		1	60 D	0.921	1469.102	-2.57E-05
		1	30 D	0.831	1343.949	-1.84E-05
		2	30 C	0.969	8843.655	-5.32E-06
		2	60 C	0.954	7942.487	-5.62E-06
		2	90 C	0.035	962.034	2.03E-06
		2	100 C	0.023	1085.350	1.15E-06
		2	60 D	0.703	8782.563	3.93E-06
		2	30 D	0.795	8053.293	4.29E-06

A.3 Guidelines

A.3.1 List of abbreviations

Abbreviation	Explanation
Approx.	Approximately
Avg.	Average
B&S	Breathing and swelling
BEV	Battery electric vehicle
BMS	Battery management system
CC	Constant current
CV	Constant voltage
DAQ	Data acquisition system
DOD	Depth of discharge
DST	Dynamic stress test
EV	Electric vehicle
EL	Electronic load
EVB	Electrical vehicle battery
ICE	Internal combustion engine
GHG	Greenhouse gasses
GIC	Graphite intercalation compound
LCO	Lithium cobalt oxide
LMO	Lithium manganese oxide
Max.	Maximum
Min.	Minimum
NCA	Nickel cobalt aluminium
NMC	Nickel manganese cobalt
PHEV	Plug-in hybrid electric vehicles
PS	Power Supply
Ref	Reference
S1	Capacitive sensor 1
S2	Capacitive sensor 2
SEI	Solid electrolyte interface
SOC	State of Charge

A.3.2 List of units of measurements

µm	Micrometre	Length	$1 \times 10^{-6}\ m$
A	Ampere	Electric current	A
°C	Celsius	Temperature	$°C$
cm³	Cubic centimetre	Volume	$m^3 \times 10^{-6}$
Hz	Hertz	Frequency	s^{-1}
g	Grams	Mass	$kg \times 10^{-3}$
kg	Kilograms	Mass	kg
kN	Kilonewton	Force	$(kg \cdot m \cdot s^{-2}) \times 10^3$
kPa	Kilopascal	Pressure	$(kg \cdot m^{-1} \cdot s^{-2}) \times 10^3$
Mbps	Megabit per second	Data-transfer rate	$(bit \cdot s^{-1}) \times 10^6$
mm	Millimetre	Length	$1 \times 10^{-3}\ m$
m	Metre	Length	m
m³	Cubic metre	Volume	m^3
MHz	Megahertz	Frequency	$(s^{-1}) \times 10^6$
MPa	Megapascal	Pressure	$(kg \cdot m^{-1} \cdot s^{-2}) \times 10^6$
N	Newton	Force	$kg \cdot m \cdot s^{-2}$
Pa	Pascal	Pressure	$kg \cdot m^{-1} \cdot s^{-2}$
s	Seconds	Time	s
V	Volt	Voltage	$kg \cdot m^2 \cdot s^{-3} \cdot A^{-1}$

A.3.3 Line legend

Conventional line colours unless otherwise specified.

Reference	**Colour**
Cell 1	Red
Cell 2	Green
Cell 3	Blue
Cell 4	Brown
Cell 5	Purple
Cell 6	Orange
Cell 7	Light green
Maximum	Bright green
Minimum	Red
Arithmetic mean	Black
State of charge	Fuchsia
Current	Dark green
Voltage	Dark red